Coupling of Quantum Emitters in Nanodiamonds to Plasmonic Structures

Kumar, Shailesh

Publication date:
2012

Document Version
Publisher's PDF, also known as Version of record

Coupling of Quantum Emitters in Nanodiamonds to Plasmonic Structures

Shailesh Kumar

A thesis submitted for the degree
Doctor of Philosophy in Physics
Technical University of Denmark

Supervisor
Professor Ulrik L. Andersen
Department of Physics
Technical University of Denmark

July 2012

Dedicated to

Gandhbaba Vishuddhanand

&

My Parents

Acknowledgements

First of all, I would like to express my gratitude towards my supervisor Ulrik L. Andersen for all the support, and for allowing me to work in my own way. I am thankful to Alexander Huck also for his support, and especially for his help in the optics lab. I am also thankful to Abdul shakoor for his help with the chemical and cleanroom work. I thank Ying-Wei Lu for all his attempts towards making silicon-nitride waveguides. I am thankful to CEN staff for training and support on the E-beam and FIB machines. I also thank DANCHIP staff for their support with the cleanroom work. I am thankful to Yuntian Chen for the calculations of the total decay rate enhancements. I would also like to thank Jonas Schou Neergaard-Nielsen and Niels Israelsen Kristiansen for the discussions, and also for their help with the translation of the 'Abstract' of this thesis to the Danish language.

I would like to thank Ander S. Sørensen and Peter Lodahl for all the discussions during our 'Plasmon meetings', which was very helpful.

I thank Mikael Lassen for sharing his interesting thoughts, it has been really nice to have him as an office-mate. I thank all the group members of QUIN for their help, and for keeping a nice and friendly atmosphere for work. I would also like to thank Dorte for her support with the administrative work.

I would like to thank my family and friends for their continuous support.

Abstract

This PhD thesis describes work towards the enhancement and efficient channeling of photons emitted from a single photon emitter. The emitter used is a defect center, the Nitrogen-Vacancy (NV) center, in diamond. The NV-center has many unique properties, such as long coherence time of its electronic spin states and the possibility of the optical readout of the spin states, which makes it a possible candidate for quantum computing applications. Efficient channeling in combination with enhancement of the emission from the NV-centers will be useful for its application in quantum optics and other applications such as sensing of the magnetic field. In this work, NV-centers in nanodiamond crystals smaller than 100 nm were used.

For enhancing and channeling emission from the NV-centers, metallic waveguides are used in this work. In such waveguides, electromagnetic waves are guided at the interface between metallic and dielectric structures. These electromagnetic waves are known as surface plasmon polaritons. The metallic waveguides, and in general plasmonic waveguides, can confine light far beyond the diffraction limit known for the dielectric waveguides. This confinement of light enables the enhancement and channeling of the emission from an emitter into the plasmonic waveguide.

Plasmonic waveguides can have many structures, which can guide and confine light. For instance, a straight cylindrical nanowire made of silver is a plasmonic waveguide, which is used for coupling to an NV-center in this thesis. Another structure used for the coupling is two nanowires placed in parallel, which supports plasmonic modes in the gap between nanowires. The distribution of electromagnetic field in the plasmonic mode depends on the structure of the waveguide. The coupling between an emitter and the plasmonic mode, in turn, depends on the confinement of the plasmonic mode. The coupling between a single NV-center and a single silver nanowire was obtained controllably, by moving the nanodiamonds across the sample near to a silver nanowire. Due to the coupling between the emitter and the plasmonic waveguide, the decay rate of the emitter is enhanced. An enhancement of the NV-center's decay rate by a factor

of 4.6 was observed. Using the gap modes of two parallel silver nanowires for coupling to an NV-center, an increased efficiency of coupling was obtained. In this case, a decay rate enhancement by a factor of 8.3 was observed. Coupling of the NV-centers to the plasmonic mode of silver nanowires was also achieved by placing the emitter at the end of a nanowire and in the gap between two end-to-end aligned nanowires. All these coupled systems were assembled using an atomic force microscope (AFM), by manipulating the nanodiamonds containing the NV-centers and the silver nanowires.
Silver nanowires used for the experiments mentioned above were chemically synthesized. Predesigned silver structures were also fabricated, using two methods. In the first method, structures were sculptured with focused ion beam (FIB) milling of chemically synthesized single crystalline silver nanoplates. The silver nanowire made using this technique was characterized optically, and the propagation of plasmons was observed. In the second method, the silver nanowires were fabricated by carving them from the silver nanoplates with the tip of an AFM cantilever. These nanowires were subsequently used for coupling to an NV-center.
A drawback of the plasmonic waveguides is their high propagation loss. This makes it necessary to couple out photons, e.g. channeled from an emitter, into a dielectric waveguide. The numerical simulation of evanescent coupling between a plasmonic waveguide and a dielectric waveguide made of silicon nitride suggest that the two waveguides can be coupled with a coupling loss of around 30 percent. Evanescent coupling between two plasmonic waveguides is also studied which can be useful for all integrated quantum plasmonic circuits.

Dansk Resumé

Denne PhD-afhandling beskriver arbejdet med forstærkning og effektiv kanalisering af fotoner emitteret fra en enkelt-foton-kilde. Den anvendte emitter, nitrogen-vakance (NV) centeret, er et defektcenter i diamant. NV-centret har mange unikke egenskaber såsom lang kohærenstid af dets elektron-spin-tilstande og muligheden for optisk at aflæse dets spintilstand, hvilket gør det nyttigt til kvanteberegningsanvendelser. Effektiv kanalisering i kombination med forstærkning af emission fra NV-centeret vil være nyttigt i anvendelser inden for kvanteoptik såvel som i andre anvendelser så som højpræcisionsmålinger af magnetfelter.

Til forstærkning og kanalisering af emission fra NV-centret benyttes i dette arbejde metalliske bølgeledere. De elektromagnetiske bølger ledes i grænsefladen mellem dielektrikum og metalliske overflader i sådanne bølgeledere. Disse elektromagnetiske bølger betegnes overflade-plasmon-polaritoner. De metalliske bølgeledere, også kaldet plasmoniske bølgeledere, kan indskrænke lyset langt udover diffraktionsgrænsen for dielektriske bølgeledere. Denne indskrænkning af lyset muliggør forstærkning og kanalisering af emissionen fra en emitter ind i en plasmonisk bølgeleder.

Plasmoniske bølgeledere kan have mange strukturer, som for eksempel silver bølgeledere med cirkulære tværsnit og to bølgeledere med cirkulære tværsnit med en spalte mellem sig, som kan lede og indskrænke lys. Distributionen af det elektromagnetiske felt af en plasmonisk mode afhænger af strukturen. Koblingen mellem en emitter og den plasmoniske mode afhænger af indskrænkningen af den plasmoniske mode. Koblingen mellem nogle få af de mange mulige plasmoniske strukturer og et enkelt NV-center er præsenteret i denne afhandling.

Kobling mellem et enkelt NV-center og en enkel sølvnanotråd opnåedes. Grundet koblingen mellem emitteren og den plasmonisk bølgeleder blev henfaldsraten af emitteren forstærket. En forstærkning af henfaldsraten af NV-centeret med en faktor 4,6 blev observeret i dette tilfælde. Ved brug af en spalte-mode fra to parallelle sølvnanotråde til kobling til NV-centeret blev en henfaldsrateforstærkning på en faktor

8,3 observeret. Koblingen af NV-centeret til den plasmoniske mode af sølvnanotrådene ved at placere emitteren ved enden af en nanotråd og i spalten af to ende-til-ende lineærede nanotråde er også beskrevet. Alle disse koblede systemer var konfigureret ved brug af et Atomic Force Microscope (AFM) ved at manipulere nanodiamanterne indeholdende NV-centre og sølvnanotrådene. Sølvnanotrådene benyttet til disse eksperimenter var kemisk syntetiseret.
Foruddefinerede sølvstrukturer blev fremstillet med fokuseret ionstråle (FIB) fræsning af kemisk fremstillede enkelt-krystallinske sølv-nanoplates. Sølvnanotrådene fremstillet ved anvendelse af denne teknik blev karakteriseret optisk, og udbredelse af plasmoner blev observeret. Sølvnanotråde blev også fremstillet ved udskæring fra sølv nanoplates med spidsen af en AFM kantilever, som derefter blev anvendt til kobling til et NV-center.
Plasmoniske bølgeledere har højt udbredelsestab, hvilket gør det nødvendigt at koble fotoner kanaliseret fra en emitter videre ind i en dielektrisk bølgeleder. Numeriske simuleringer af den evanescente feltkobling mellem en plasmonisk bølgeleder og en dielektrisk bølgeleder estimerer at de to bølgeledere kan kobles med et koblingstab på ca. 30 procent. Evanescent feltkobling mellem to plasmoniske bølgeledere, som kan være brugbart i forbindelse med al slags kvanteplasmonteknologi, er også blevet studeret.

Contents

List of Figures

Chapter 1

Introduction

Plasmons are collective oscillations of charge densities. The field that studies plasmons and related effects is known as 'plasmonics'. Plasmons can couple to photons and form quasiparticles known as plasmon polaritons. In recent years, there has been a rapid expansion of research into nanophotonics based on surface plasmon polaritons. These electromagnetic waves propagate along metal-dielectric interface and allows for a localization of light that can be much smaller than the associated wavelength in vacuum [1, 2]. This can be used to build very compact optical devices. Plasmonics can also be a platform for merging electronic and optical devices [3], because the size of optical and electronic devices can match with plasmonic devices whereas plasmonic waveguides allows for propagation of high bandwidth signals similar to optical waveguides [4]. In the visible and near infrared (NIR) part of the spectrum, noble metals are used as plasmonic waveguide materials due to a large number of free elctrons [5]. Various structures of metals have been studied for guiding light, including silver nanowires, [6], grooves [7, 8] and gaps between metallic structures [9]. Hybrid waveguides with very high confinement of propagating modes have also been demonstrated [10]. Many other passive plasmonic devices, including beam splitters and routers have been realized [11]. Active devices such as spasers [12, 13], and on-chip detectors for plasmons have also been realized [14, 15]. This basically means that many of the components necessary to build an all integrated plasmonic circuit have been demonstrated. However, challenges still remain, mainly due to high intrinsic losses in the metals and stringent requirements for processing of the metals. Further work towards novel plasmonic materials in order to obtain low loss plasmonic devices is needed [5].

Plasmonics allows for high confinement of electromagnetic fields, which has shown to

enable an enhancement of Raman signals [16], generation of high harmonics [17] and enhancement of fluorescence from emitters [18, 19]. Due to the Purcell effect, careful engineering of an emitter's electromagnetic environment can enhance the decay rate of the emitter as well as direct its emission into specified directions. Different emitters, including molecules [20, 21], quantum dots [22] and nitrogen-vacancy (NV) centers in diamond [23, 24] coupled to plasmonic nanoantennas have been used, to benefit from the properties - enhancement and directionality.

Many of the protocols for quantum information processing rely on high photon flux and emission of radiated photons into single spatial optical modes [25, 26]. A single emitter efficiently coupled to a single optical mode can yield single photons on demand [27, 28], or allow for non-linear gate operations at the level of a few photons [25]. Various paths have been followed for channelling of emission from an emitter into single optical modes, such as dielectric waveguides [29, 30], optical cavities [31, 32] and plasmonic waveguides [27, 33]. Coupling to the dielectric waveguides is limited by diffraction. Optical cavities have very small spectral width and usually the challenge is to match the cavity spectrum to the spectrum of the emitter. One more problem with the cavities approach is to couple out light efficiently to a propagating mode. On the other hand, plasmonic approach for coupling to single emitters is not bandwidth limited, and proposals and demonstrations exist for efficient outcoupling of light from plasmonic modes to dielectric modes [28, 34]. The coupling of Nitrogen-Vacancy (NV) centers in nanodiamonds to propagating plasmonic modes is investigated in this thesis.

NV-centers in diamond are a good candidate for quantum information processing at room temperature, because of the long coherence time of its electronic spin states [35]. The electronic spin state of an NV-center can be initialized, and probed optically [36]. Applications of an NV-center, such as detection of magnetic fields [37], can benefit from an efficient collection of photons emitted from the NV-center. Plasmonic modes can provide a way for enhancing as well as channeling of photons from an NV-center. We study different possible ways of an efficient channeling of emission from a single NV-center in a nanodiamond to propagating plasmonic modes.

We investigate a few plasmonic waveguides for coupling of the NV-centers to the propagating modes of a plasmonic waveguide. In Chapter 2, we review the properties of an NV-center and describe our experimental set-up. Theoretical approaches to estimate the coupling between dipole emitters and the propagating modes of plasmonic waveguides is also presented. We couple a single NV-center to a single nanowire plasmonic waveguide. We compare the properties of an emitter before and after coupling by

controllably moving the emitter close to a plasmonic waveguide. This is described in Chapter 3. In Chapter 4, we study coupling of NV-centers to gap plasmonic modes of two parallel silver nanowires. We study this waveguide theoretically and also demonstrate with experiments that the coupling of a quantum emitter to the gap modes of silver nanowires can be more efficient than coupling to a single silver nanowire. Coupling of the NV-centers to the plasmonic mode of silver nanowires was also obtained by placing the emitter at the end of a nanowire. This approach allows for the channelling of emission from the NV-center in one direction. We also coupled an NV-center to the propagating plasmonic mode of silver nanowires by placing a nanodiamond in the gap between two end-to-end aligned silver nanowires. This presents an alternative to coupling when the nanodiamond is placed in a plane transverse to the mode propagation direction in the silver nanowire. These studies of coupling, by placing the nanodiamonds near to ends of silver nanowires, are presented in chapter 5.
Chemically grown silver nanowires are used for all the experiments mentioned above. We have also used some novel methods to fabricate silver nanowires. In chapter 6, we describe a method to fabricate single crystalline designed silver structures, using chemically grown silver nanoplates and subsequent focussed ion beam milling of them. In chapter 7, another method for fabricating designed nanowires is presented, where we sculpture silver nanowires from the silver nanoplates using the tip of an AFM cantilever. Plasmonic modes on these nanowires are then excited with single NV-centers.
Because of higher losses in plasmonic waveguides, they can not directly be used as a channel for long distance communication. Thus for long distance communication applications, it is important to couple out light from a plasmonic waveguide to a dielectric waveguide. We have studied the evanescent coupling between silicon nitride waveguides and silver nanowires. For all integrated plasmonic devices, it is important that one can couple light from one plasmonic waveguide to another. We study coupling between two silver nanowires. The coupling between waveguides is presented in chapter 8. In chapter 9, we present the conclusion of the studies and also an outlook for the future work for obtaining efficient channeling of emission from a single emitter to a dielectric waveguide.

Chapter 2

Nitrogen-Vacancy Centers in Nanodiamonds and Coupling to Plasmonic Structures

2.1 The Nitrogen-Vacancy Center in Diamond

Several types of color centers, arising from defects, in diamond are known, and have been studied [38, 39]. One such color center in diamond is the Nitrogen-Vacancy (NV) center. NV-centers in diamond are a good candidate for quantum information processing at room temperature because of the long coherence time of their electronic spin states [35]. The electronic spin state of an NV-center can be initialized, and probed optically [36]. The NV center is a possible candidate for optically coupled quantum registers [40] and distributed quantum computation [41] as well. It has been shown that the proximal nuclear spins of adjacent atoms can be coherently controlled via a hyperfine interaction [42]. This can be used as a basis for quantum memory with an extremely long coherence time [43]. The spin-photon entanglement of the photons emitted and the electronic spin state of the NV-center has also been demonstrated, which should allow for long distance communication between spin qubits [44]. Clearly, the NV-center in diamond has many unique properties to make it a good candidate for quantum information processing.

The NV-center is formed by substitution of one carbon atom with nitrogen and with an adjacent lattice site vacant, hence the name Nitrogen-Vacancy (NV) center. The NV center has a trigonal C_{3v} symmetry [45]. Figure 2.1 shows a ball and stick diagram

illustrating the NV-center defect in a diamond. NV center has two charged states: neutral (NV^o) and a singly negatively charged (NV^-).

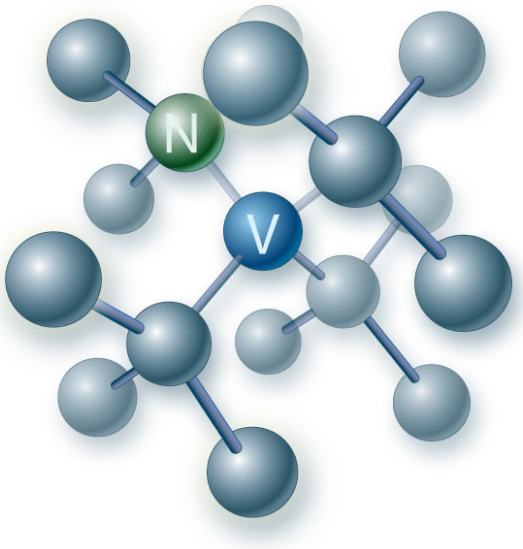

Figure 2.1: Ball and stick diagram of a diamond containing an NV-center defect. The unmarked balls represent carbon atoms. N: Nitrogen, V: Vacancy.

The low temperature energy level diagram is presented in figure 2.2(a) for the negatively charged NV color center [46], which is more commonly observed NV-center in our nanodiamonds. The ground state (GS) of NV^- center is a spin triplet denoted as $^3A_2$. The GS splitting between the S_z ($m_s = 0$) singlet state and doublet state S_x, S_y ($m_s = \pm 1$) is $D_{gs} = 2.88$ GHz due to spin-spin interaction. The excited state (ES), denoted as ^3E, is an orbital doublet, and the degeneracy is lifted by nonaxial strain into two orbital branches, E_x and E_y. Each of the orbital branches is a spin triplet, and consists of the three spin states, S_x, S_y and S_z. Optical transitions between the GS and the ES are primarily spin conserving, illustrated by the red arrows in figure 2.2(a) [47]. Only non-radiative transitions through an intersystem crossing to ^1A are spin non-conserving, which is indicated by the dashed arrow in figure 2.2(a). Nonradiative intersystem crossing to the ^1A state is strongly spin selective, the transition probability from S_x and S_y to ^1A is much bigger than that from S_z to ^1A. In addition to that, the metastable state decays preferentially to the ground state S_z level. With optical pumping, this allows for initialization into the $m_s = 0$ state [47]. The excited state structure depends strongly on the local strain. The local strain of an NV-center can

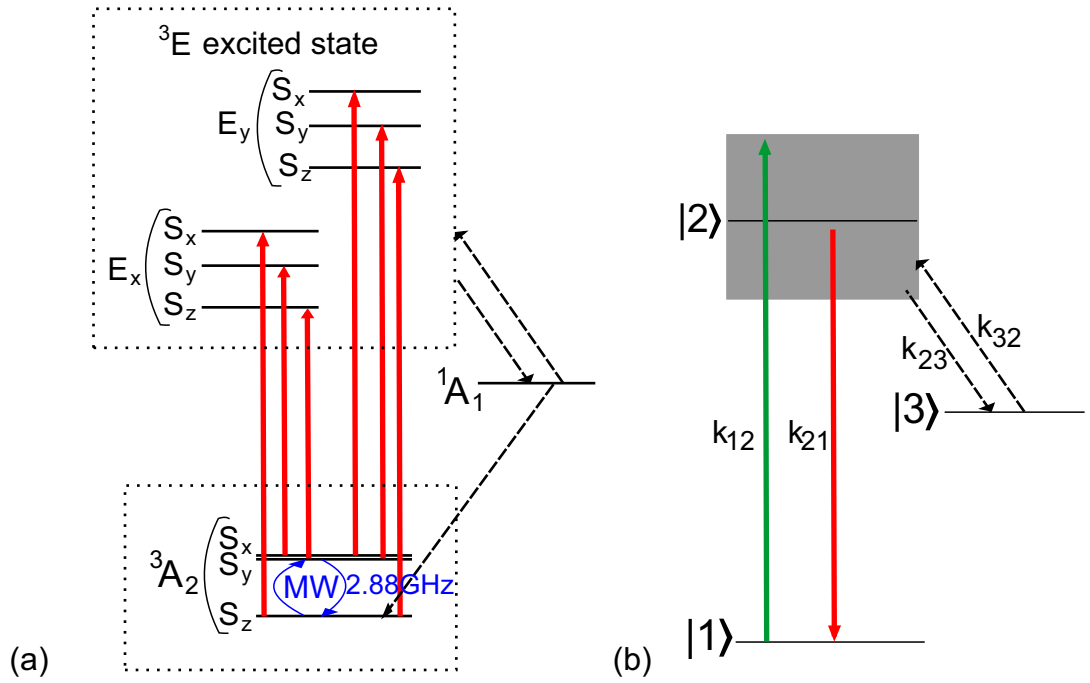

Figure 2.2: (a) Electronic level structure at low temperature. (b) Energy diagram model used as a basis for the rate-equations. Transitions from the shelving state '3' to the ground state '1' are neglected.

be changed by applying a static electric field, and hence the splitting can be controlled using the Stark effect. One can use the stark effect to match the emission spectra of two NV-centers. This has lead to the successful demonstration of two photon interference experiments from two well separated NV-centers [48, 49].

The NV-center in diamond is a stable single photon source at room temperature [50]. The diamond has a high bandgap of 5.50 eV [51, 36]. The NV-center has a single optically active level, which makes it a single photon source, and has been proposed for applications in quantum cryptography [52, 50, 53, 54]. Moreover, nanodiamonds as small as a few nanometers have been shown to contain single NV-centers [55, 56]. The emission properties in small nanodiamonds have been studied and have been shown to emit single photons at room temperature [57]. At room temperature, for NV^o and NV^- centers, one observes optical transitions with zero phonon lines (ZPLs) at 575 nm (2.155 eV) and 637 nm (1.945 eV), respectively, accompanied by a phononic band at higher energy in absorption and lower energy in emission. The emission spectra with excitation at 532 nm continuous wave (CW) laser, measured with our set-up (explained in next section), for emission from NV^o and NV^- centers is shown in figure 2.3. For the

work described in this thesis, we have used NV-centers in nanodiamonds because these are stable single photon sources at room temperature, and because the nanodiamonds can be manipulated with the tip of an atomic force microscope (AFM) cantilever [58, 59].

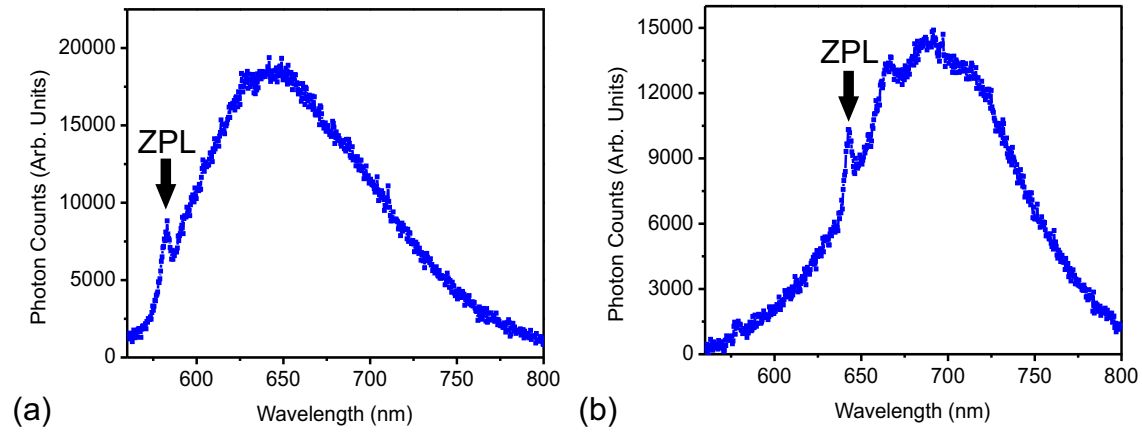

Figure 2.3: Fluorescence spectrum of (a) NV^o and (b) NV^- centers. The zero phonon lines (ZPLs) are indicated by arrows.

One can describe the population dynamics of the NV-center with rate equations of a three level system [50]. The energy level labelling and the different rates are illustrated in figure 2.2(b). If we neglect all coherences, the population dynamics of the ground (1), the excited (2), and the shelving (3) states are governed by,

$$\begin{pmatrix} \dot{\rho}_1 \\ \dot{\rho}_2 \\ \dot{\rho}_3 \end{pmatrix} = \begin{pmatrix} -k_{12} & k_{21} & 0 \\ k_{12} & -k_{21} - k_{23} & k_{32} \\ 0 & k_{23} & -k_{32} \end{pmatrix} \begin{pmatrix} \rho_1 \\ \rho_2 \\ \rho_3 \end{pmatrix}, \tag{2.1}$$

where ρ_i, $i = \{1,2,3\}$, is the population probability of state i and $\rho_1 + \rho_2 + \rho_3 = 1$. In this model, possible non-radiative transitions from the shelving state to the ground state are neglected because they are about three orders of magnitude smaller than all other rates [50]. The emission rate of a photon R is proportional to the population of the excited state $\rho_2(t)$, which in the steady state regime ($\dot{\rho}_1 = \dot{\rho}_2 = \dot{\rho}_3 = 0$) can be written as,

$$\rho_2(t \to \infty) = \frac{k_{32}k_{12}}{k_{12}k_{23} + k_{12}k_{32} + k_{21}k_{32}} \tag{2.2}$$

This population shows a saturation behavior as a function of the pump rate k_{12}.

The emission of a single photon from an emitter is witnessed by the second order autocorrelation function, $g^{(2)}(\tau)$, which for an N-photon Fock state, at $\tau = 0$, is given as [60],

$$g^{(2)}(0)_{\mathrm{N}} = 1 - \frac{1}{\mathrm{N}} \tag{2.3}$$

Hence, the condition $g^{(2)}(0) < 0.5$ is sufficient to prove that the emitted fluorescence is in a single photon state. The autocorrelation function for the NV-center, with the levels and rate equations defined as above, is given by [50, 60]:

$$g^{(2)}(\tau) = 1 + C_2 e^{-|\tau|/\tau_2} + C_3 e^{-|\tau|/\tau_3}, \tag{2.4}$$

with the decay rates and coefficients given by

$$\begin{aligned} 1/\tau_{2,3} &= A/2 \pm \sqrt{(A/2)^2 - B}, \\ C_2 &= \frac{1 - \tau_2 k_{32}}{k_{32}(\tau_2 - \tau_3)}, \; C_3 = -1 - C_2, \end{aligned} \tag{2.5}$$

with

$$\begin{aligned} A &= k_{12} + k_{21} + k_{32} + k_{23}, \quad \text{and} \\ B &= k_{12}k_{23} + k_{12}k_{32} + k_{21}k_{32}. \end{aligned} \tag{2.6}$$

2.2 Experimental Set-up and Characterization of Single NV-centers in Nanodiamonds

Our experimental setup is a home-built inverted scanning confocal microscope using an oil immersion objective with a numerical aperture (NA) of 1.4 combined with a coaxially aligned atomic force microscope (AFM, NT-MDT SMENA), as illustrated in figure 2.4. For the excitation of NV-centers, we either use a CW or a pulsed laser, both operating at a vacuum wavelength of 532 nm. The pulsed laser has a repetition rate of 5.05 MHz and a pulse width of 4.6 ps. The fluorescence emission from the sample is collected by the oil immersion objective and is split into two optical channels with a 50/50 beam splitter. The two channels detect fluorescence with avalanche photo diodes APD_1 and APD_2, respectively. The channel of APD_1 is directly aligned with the pump beam, while the channel of APD_2 is decoupled from the pump beam via a galvanometric mirror, as illustrated in figure 2.4. The fluorescence filters placed in

front of both detectors are highly transmissive for photon wavelengths between 647 nm and 785 nm.

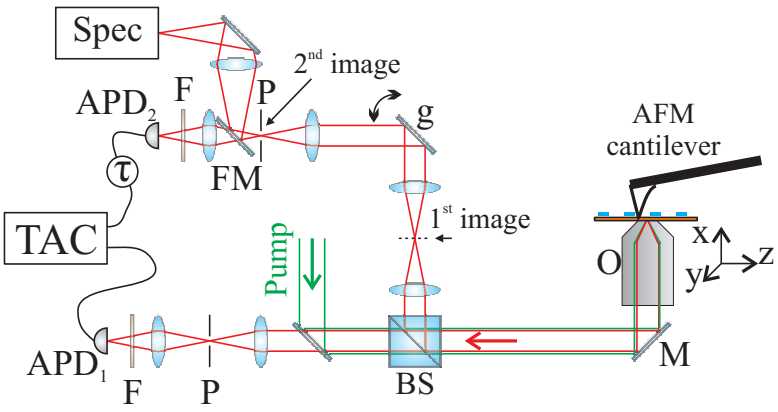

Figure 2.4: Experimental setup: TAC - time to amplitude converter, APD_1 and APD_2 - avalanche photo diodes for detection channels 1 and 2, respectively, g - galvanometric mirror, BS - 50/50 beam splitter, Spec - Spectrometer , FM - Flip Mirror, O - objective (NA=1.4), P - Pin-hole, M - Mirror, AFM - Atomic Force Microscope. The transmitted spectrum of the fluorescence filter F lies between 647 nm and 785 nm.

For this work, nano-crystal diamonds 'MSY 0-0.05 Mikron GAF' or 'MSY 0-0.1 Mikron GAF' from Microdiamant AG were used. 'MSY 0-0.05 Mikron GAF' nanodiamond crystals have a mean diameter of $\approx 30\ nm$ and a maximum size of $\approx 50\ nm$. In 'MSY 0-0.1 Mikron GAF', crystals have a mean diameter of $\approx 50\ nm$ and a maximum size of $\approx 100\ nm$. In less than 1% of the nano-crystals, single NV defects can be found [23]. For the sample preparation, the solution containing nanodiamonds is diluted to obtain a concentration of 2 $carats/liter$. The solution was then spin coated on a plasma cleaned fused silica substrate.

The fluorescence image obtained from a sample containing nanodiamonds is presented in figure 2.5(a). Lifetime of an NV-center is measured by exciting it with the pulsed laser, and measuring the emission times with respect to the excitation times using a time to amplitude converter (TAC). The lifetime measurement data and a model fit, for the NV-center fluorescence shown circled in figure 2.5(a), is presented in figure 2.5(b). The model used for fitting the lifetime measurement data is a single exponential, with a constant offset corresponding to the dark counts. The lifetime in this case is 26 ns. In contrast to NV-centers in bulk diamond, where an excited state lifetime of $\tau_{0,bulk} \approx$ 12 ns is usually measured [61, 62], we attribute the increased lifetime to the decreased

effective refractive index of the surroundings, which is significantly smaller than the refractive index of bulk diamond. The measured emission rate of the NV defect from figure 2.5(a) as a function of excitation power is shown in figure 2.5(c), recorded with APD_1. The count rate (R) in terms of excitation power (P_{ex}) follows a function,

$$R(P_{ex}) = R_\infty \frac{P_{ex}/P_{sat}}{1 + P_{ex}/P_{sat}} \tag{2.7}$$

where R_∞ is the rate for $P_{ex} \to \infty$ and P_{sat} is the saturation pump power defined as $R(P_{sat}) = R_\infty/2$. From the fit in figure 2.5(c), the coefficients obtained are $R_\infty = 48k\,s^{-1}$ and $P_{sat} = 106\,\mu W$. Figure 2.5(d) shows the dependence of fluorescence from a single NV-center on the polarization of excitation laser light. The excitation power in this case was $83\,\mu W$. The measured data is fitted to a sinusoid with a constant offset, which is the red curve in figure 2.5(d). The visibility defined as $V = (R_{max} - R_{min})/(R_{max} + R_{min})$ in this case is nearly 0.5. The visbility, V, is found to vary between 0 and 1 for different NV-centers.

In the set-up, APD_1 and APD_2 compose, together with the beam splitter BS, the well known Hanbury-Brown and Twiss interferometer used for the characterization of a single photon source [63]. Practically, $g^{(2)}(\tau)$ is measured by start-stop technique by accumulating histograms using TAC, as shown in figure 2.4. The signal from APD_1 ($i_1(t)$) is used as the start trigger and the signal from APD_2 ($i_2(t)$) as the stop trigger of the TAC. $g^{(2)}(\tau)$ is given by,

$$g^{(2)}(\tau) = \frac{\langle i_1(t) i_2(t+\tau)\rangle}{\langle i_1(t)\rangle \langle i_2(t+\tau)\rangle} \tag{2.8}$$

where $i_1(t+\tau)$ and $i_2(t)$ are the photon counts of the detectors APD_1 and APD_2, respectively, and $\langle \ldots \rangle$ denotes averaging over time t. The two APDs APD_1 and APD_2 detecting single photons at arrival times $t_1 = t$ and $t_2 = t + \tau$, as shown in figure 2.4, results in a histogram count $\langle i_1(t) i_2(t+\tau)\rangle$ at τ. In order to acquire negative times, the signal of D_2 was delayed by a 260 ns cable delay line. Thus, in case of a single photon emission no coincidences $\langle i_1(t) i_2(t+\tau)\rangle$ are measured for $\tau = 0$. Finally, $g^{(2)}$ was normalized such that $g^{(2)}(\tau \to \infty) = 1$.

In figure 2.6 the measured and modelled (using Eqn. (2.4)) second order correlation function $g^{(2)}(\tau)$ are plotted for pump powers of $10\,\mu W$, $50\,\mu W$ and $170\,\mu W$. At $\tau = 0$, the auto-correlation function $g^{(2)}(\tau) < 0.5$. Hence, the NV-center emits single photons. Generally, this behavior is referred to as photon anti-bunching. On a slightly longer

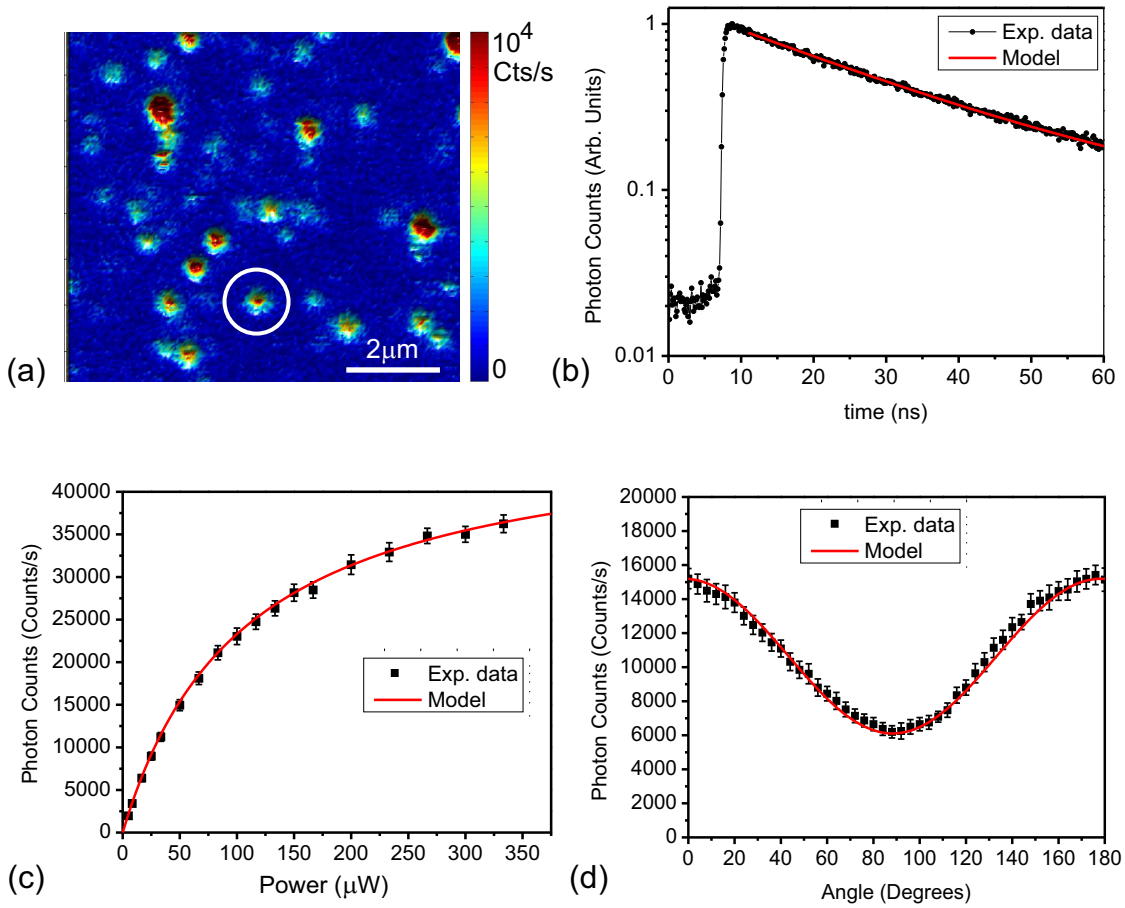

Figure 2.5: **(a)** Fluorescence measured from a sample containing nanodiamonds. The circled region indicates fluorescence from a single NV-center. **(b)** Lifetime measurement data. **(c)** Photon counts obtained as a function of excitation power. **(d)** Photon counts obtained when the polarization of excitation laser was changed.

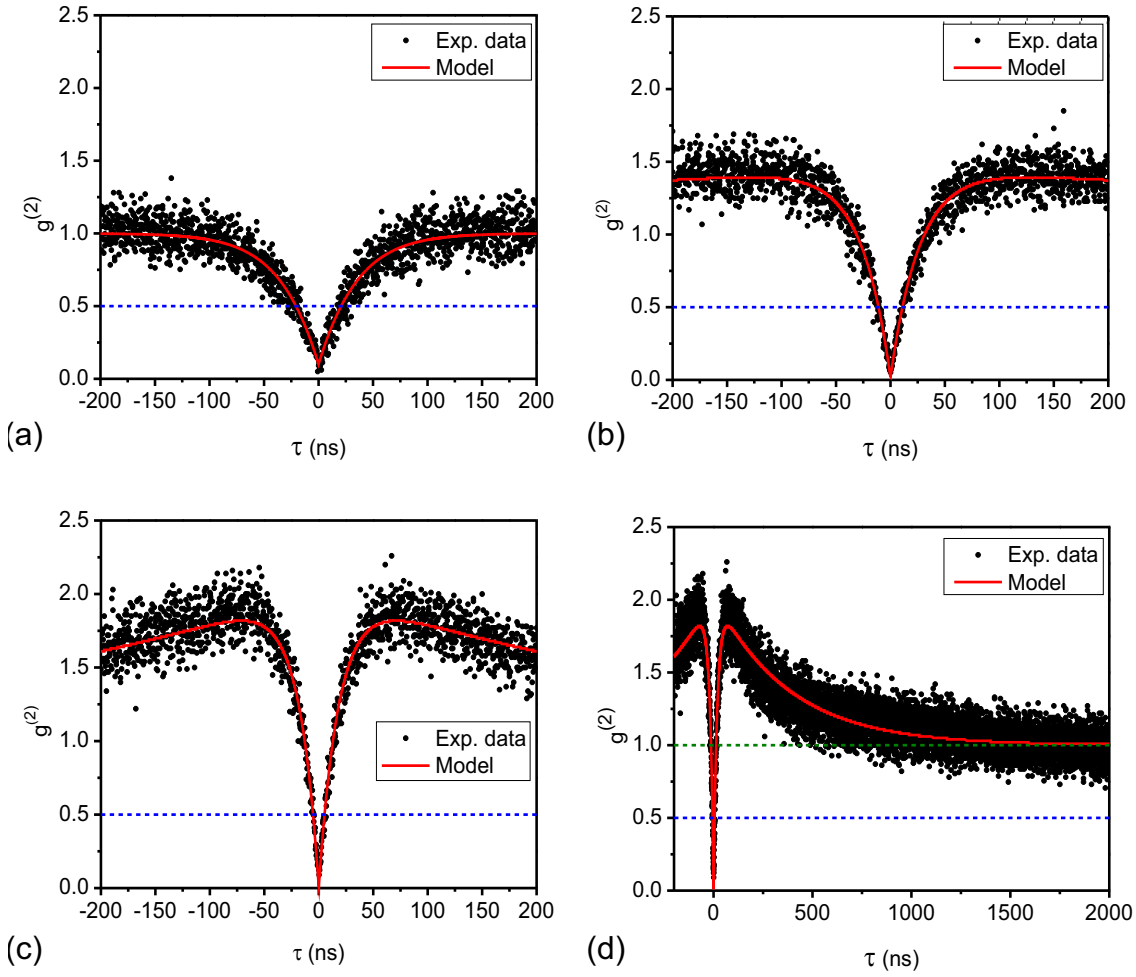

Figure 2.6: **(a)**, **(b)** and **(c)** Autocorrelation measured for an NV-center for excitation powers of 10μ W, 50 μW and 170 μW, respectively. **(d)** Autocorrelation shown for longer τ, for excitation power of 170μW.

time scale, as can be seen from figure 2.6(d), the light field emitted by the NV center bears photon bunching properties, as $g^{(2)}(\tau) > 1$. This behavior is different when compared to a pure two level system, and is due to the presence of the shelving state. As can be seen from figure 2.6, the photon bunching becomes clearly measurable for higher excitation powers.

Our set-up also consists of an AFM, which can be operated in tapping mode or contact mode. Tapping mode operation is used to record the topography of the sample, and with this to measure the height of the nanowire and the nanodiamond crystals as well as the lateral position of individual nano-crystals with respect to the silver nanowire. By using the AFM in contact mode operation, we are able to controllably push a chosen diamond nano-crystal across the sample. This technique is used to place a single diamond nano-crystal near a silver nanowire, for example. We also cut and move silver nanowires with the tip of an AFM cantilever, which is used to assemble different plasmonic systems coupled with single NV-centers in nanodiamonds.

2.3 Propagating Plasmonic Modes

Plasmonic waveguides can confine light much beyond the diffraction limit. In metals, the sign of $Re(\epsilon)$ is negative due to the presence of free electrons in the metallic lattice. This leads to a crucial difference between properties of metallic and dielectric waveguides, as will be seen in the following. The modes for a waveguide can be obtained by solving the wave equation. The wave equation for the electric field can be written as,

$$\nabla \times \frac{1}{\mu_{\mathrm{r}}} \left(\nabla \times \mathbf{E}\left(r\right)\right) - k_0^2 \epsilon\left(r\right) \mathbf{E}\left(r\right) = 0 \tag{2.9}$$

where, $r \equiv (x, y, z)$, $k_0 = \omega\sqrt{\epsilon_0 \mu_0}$ is the vacuum wavenumber with ω the angular frequency of wave, and ϵ_0 and μ_0 the permittivity and permeability of vacuum, respectively. $\epsilon\left(r\right)$ is dielectric function relative to vacuum and μ_{r} denotes the relative permeability constant. μ_{r} will be assumed 1 for all calculations involved in this thesis. For infinitely long waveguides with propagation direction along z-axis, the solution to the wave equation must have the following form:

$$\mathbf{E}(x, y, z) = \mathbf{E}_\alpha(x, y) e^{-i(\omega t - \beta z)} \tag{2.10}$$

For any guided mode in a waveguide (plasmonic or dielectric), at a specific angular fre-

quency ω, α and β specify a complete set of orthogonal modes. α specifies a transverse mode and β represents the propagation constant.

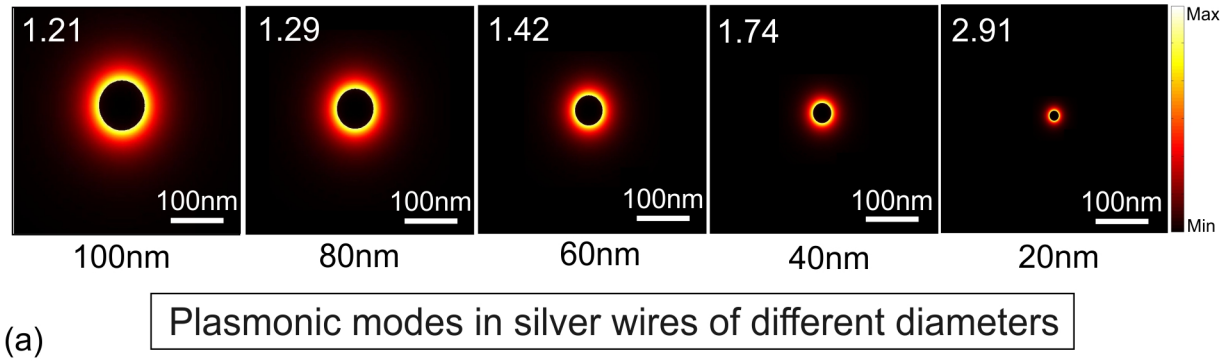

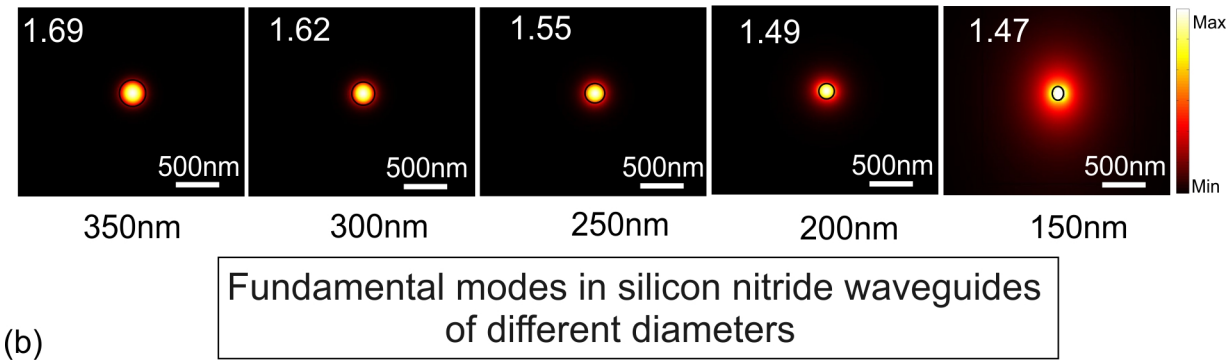

Figure 2.7: Plots of the magnitude of normalized pointing vectors in the propagation direction of fundamental modes of **(a)** silver nanowires for different diameters with air surrounding the nanowires, and **(b)** silicon-nitride waveguide for different diameters with fused silica surrounding the silicon-nitride are presented. The scale and associated effective mode indices are shown in the images.

Guided plasmonic modes can be calculated using a finite element method (FEM). We use a commercial software (COMSOL) for calculating the propagating plasmonic modes with FEM. The emission of an NV-center has a peak around 700 nm, therefore we will be using a vacuum wavelength of 700 nm for all our calculations. The electric permittivity of silver ϵ_{Ag} from [64], i.e. $\epsilon_{Ag} = -20.437 + 1.284i$ will be used. We use fused silica substrate, for which a refractive index of 1.46 will be used. The dielectric waveguide material we use is silicon nitride, for which an experimentally measured refractive index 2.0 will be used for calculations.

In figure 2.7, the component of normalized pointing vector along the propagation di-

rection of different waveguide modes is shown. Figure 2.7(a) presents the propagation modes for silver wires of different diameters placed in a uniform dielectric environment of air. As the diameter of the metallic waveguides is decreased, the mode size also decreases along with an increase in the propagation constant. This can be seen from the effective mode indices indicated in the plots for the modes of different nanowire diameters. The effective mode index is defined as the ratio of the propagation constant for the waveguide mode and that for the electromagnetic wave of the same frequency in vacuum. In figure 2.7(b), plots of component of the pointing vector in propagation direction for the fundamental modes of silicon nitride waveguides are shown. As can be seen, the waveguide modes starts to expand when the cross-section of the waveguide is made much smaller than the wavelength of light. This effect is due to diffraction limit known for the dielectric waveguides [65]. The effective mode index in this case decreases, in comparison to the metallic waveguides. The difference between the two waveguides is due to different signs of $Re(\epsilon)$ for the waveguide materials.

2.4 Coupling of Dipole Emitters to Plasmonic Waveguides

The emitter placed close to a plasmonic waveguide can decay via three channels. One, through radiative decay Γ_{rad} via emission of photons to the far field. Two, the decay into the plasmonic channel Γ_{pl} which is guided in the plasmonic waveguide. Three, decay via non-radiative channels $\Gamma_{\text{non-rad}}$. Among the nonradiative channels include, the resistive heating of metals and the decay via coupling to vibrations. We will only consider the resistive heating for the non-radiative channel, which is the dominating nonradiative channel when an emitter is placed close to a metallic waveguide. In figure 2.8, a schematics of a dipole emitter (μ) coupled to a plasmonic waveguide indicating different channels of decay is presented.

To calculate coupling of an emitter to a plasmonic waveguide, we will use two methods. In chapter 3, we will be using quasi-static approximation to calculate decay rates into different channels for a dipole emitter coupled to a silver nanowire. We will apply the analytical results obtained for a plasmonic waveguide of circular cross-section from the work of Chang et. al. [27, 28], to our coupled system.

The quasi-static approximation has limitations [66], and it cannot be applied to all the plasmonic structures we study for coupling to the NV-centers in diamond. Therefore,

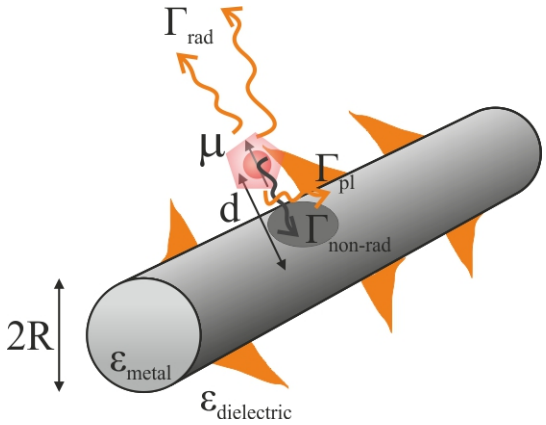

Figure 2.8: Schematics of a coupled system of an emitter (μ) coupled to a plasmonic waveguide. The three channels of decay are indicated.

we also use another method developed by Chen et. al. [66], to calculate the decay rates into plasmonic waveguide and total decay rates. In this method, the Green's function is calculated using FEM and subsequently the decay rate into the plasmonic mode is obtained. For calculating the total decay rate enhancement, the power dissipated by a dipole emitter in vacuum and power dissipated by the emitter coupled to a plasmonic waveguide are directly compared. We apply this method in chapters 3, 4 and 5. We therefore describe the numerical method briefly for completeness.

2.4.1 Decay Rate of an Emitter into a Plasmonic Mode

The electric field dyadic Green's function for a specific guided plasmonic mode can be constructed from the numerical calculation of the plasmonic modes' electric and magnetic fields, which can subsequently be used for calculation of projected local density of states (LDOS) for the plasmonic mode. The electric dyadic Green's function $\bar{\bar{G}}(r, r', \omega)$ is defined as follows,

$$[\nabla \times \nabla \times -k_0^2 \epsilon(\mathbf{r})]\bar{\bar{\mathbf{G}}}(\mathbf{r}, \mathbf{r}', \omega) = \bar{\bar{\mathbf{I}}}\delta(\mathbf{r} - \mathbf{r}') \tag{2.11}$$

where $\bar{\bar{\mathbf{I}}}$ is a unit dyad, and δ is the dirac delta function.
The projected LDOS for the plasmonic mode is given by [67]:

$$\rho_{pl}(r, \omega) = \frac{6\omega[\bar{\mathbf{n}}_\mu \cdot Im\{\bar{\bar{\mathbf{G}}}(r_0, r_0, \omega_0)\} \cdot \bar{\mathbf{n}}_\mu]}{(\pi c^2)} \tag{2.12}$$

where, $\bar{\mathbf{n}}_\mu$ is the unit vector along the dipole emitter. r_0 is the position and ω_0 is the angular frequency of the dipole emitter. c is the velocity of light in vacuum. The Green's function can be calculated from the electric field obtained with FEM simulation in COMSOL as has been described in detail in [66]. The projected LDOS for the plasmonic mode in terms of electric field is given as:

$$\rho_{pl}(r,\omega) = \frac{6\left|\mathbf{E}\left(x,y\right)\cdot\bar{\mathbf{n}}_\mu\right|^2}{Nv_g} \tag{2.13}$$

where the group velocity v_g, and the normalization factor N can be calculated, according to Snyder and Love [65], as follows:

$$v_g = \frac{Re\{\int_{A_\infty}\left(\mathbf{E}\times\mathbf{H}^*\right)\cdot\mathbf{z}_0 dA\}}{\int_{A_\infty}\epsilon_0\epsilon(x,y)\left|\mathbf{E}\left(x,y\right)\right|^2 dA}, \tag{2.14}$$

$$N = 2\pi\int_{A_\infty}\epsilon_0\epsilon(x,y)\left|\mathbf{E}\left(x,y\right)\right|^2 dA \tag{2.15}$$

where, $\mathbf{E}$ and $\mathbf{H}$ are the electric and magnetic fields of the plasmon mode, respectively, $\mathbf{z}_0$ is a unit vector along the z-direction and A_∞ denotes integration over the transverse plane.

The spontaneous emission decay rate into the plasmonic mode can be calculated from LDOS:

$$\Gamma_{pl} = \frac{\pi\omega_0}{3\hbar\epsilon_0}\left|\mu\right|^2\rho_{pl}(r,\omega) \tag{2.16}$$

where $\hbar = h/2\pi$ with h the planck's constant. Then, the spontaneous emission enhancement due to plasmonic excitation, normalized by the spontaneous emission decay rate in the vacuum, in the xy-plane (normal to the propagation direction) is given as:

$$\boxed{\frac{\Gamma_{pl}}{\Gamma_0} = \frac{6\pi^2c^3\left|\mathbf{E}\left(x,y\right)\cdot\bar{\mathbf{n}}_\mu\right|^2}{{\omega_0}^2 Nv_g}} \tag{2.17}$$

The decay rate into the plasmonic mode as a function of position coordinates, in a plane transverse to the propagation direction can be calculated with the following equation:

$$\boxed{\frac{\Gamma_{pl}}{\Gamma_0} = \frac{3\pi c\epsilon_0\left|\mathbf{E}\left(x,y\right)\cdot\bar{\mathbf{n}}_\mu\right|^2}{Re\{k_0^2\int_{A_\infty}\left(\mathbf{E}\times\mathbf{H}^*\right)\cdot\mathbf{z}_0 dA\}}} \tag{2.18}$$

According to equations 2.17 and 2.18, the confined mode and high propagation con-

stant enhances the LDOS and increases the coupling efficiency of a nearby quantum emitter to the plasmonic mode.

2.4.2 Total Decay Rate of an Emitter

We have briefly described the method followed for calculating the decay rate into the plasmonic mode by calculating the Green's dyadic function. This is possible due to confinement of the plasmonic modes. A similar approach to calculate the total decay rate due to the non-confined radiation modes can not be followed. To calculate the total decay rate, one needs to take into account the nonradiative and radiative channels of decay, in addition to the plasmonic channel of decay. A 3D model is implemented to include the radiation modes as well as the nonradiative contributions. The following equation with a harmonic source (time dependent current source) term is solved to calculate the total decay rate:

$$[\nabla \times \nabla \times -k_0^2 \epsilon\,(\mathbf{r})]\mathbf{E}(\mathbf{r},\omega) - i\omega\mu_0 \mathbf{J}(\omega) = 0 \tag{2.19}$$

where $\mathbf{J}$ is the current density. Equation 2.19 is solved by formulating an appropriate functional of the above equation which can be solved with FEM using COMSOL. Proper truncation of computational domain is crucial. In the direction transverse to the propagation direction of the plasmonic mode, the computational domain is truncated with perfectly matched layers with a thinkness of half a wavelength in vacuum. Along the propagation direction, the computational domain is terminated by a mode matching boundary condition, which behaves as a sink for electromagnetic waves. The mode matching boundary condition is obtained from the mode field calculation for the plasmonic mode in 2D, as described in the last section.

The total decay rate, Γ_{total} is extracted from the total power dissipation of the current source coupled to the nearby metallic waveguide as follows:

$$\frac{\Gamma_{total}}{\Gamma_0} = \frac{P_{total}}{P_0} \tag{2.20}$$

where $P_{total} = 1/2 \int_V Re(\mathbf{J}^* \cdot \mathbf{E}_{total}) dV$ and $P_0 = 1/2 \int_V Re(\mathbf{J}^* \cdot \mathbf{E}_0) dV$ are the powers dissipated by the same current source near to a plasmonic waveguide and in vacuum, respectively.

One can also compare two different environments by calculating the total decay rates using the procedure defined in this section. In chapter 5, we will use this procedure to

compare total decay rates when an NV-center is placed in a dielectric environment to when it is placed in the vicinity of plasmonic waveguides.

2.4.3 β-factor and Purcell Factor

β-factor and Purcell factor are figures of merit which have been defined for coupling of an emitter to plasmonic waveguides. The β-factor and Purcell factor (P) are defined as:

$$\beta = \frac{\Gamma_{pl}}{\Gamma_{total}} \tag{2.21}$$

$$P = \frac{\Gamma_{pl}}{\Gamma_{total} - \Gamma_{pl}} \tag{2.22}$$

These two factors are related, $P = \beta / (1 - \beta)$, and can be calculated using the procedure defined in this section. We will be using β-factor as a figure of merit for the plasmonic waveguides that we study.

Chapter 3

Controlled Coupling of a Single NV-center to a Single Silver Nanowire

To obtain an efficient coupling to a specific spatial mode while exploiting the enhancement properties of strongly confined surface plasmons, it has been suggested to use propagating plasmons on cylindrical wires [27]. By using this method, it is possible to enhance the emissive process into one particular propagating plasmon mode which can be further transferred into a photonic mode of an optical waveguide with high efficiency [68, 69]. The coupling of individual single photon emitters to propagating surface plasmon modes on individual silver nanowires has been demonstrated for CdSe quantum dots [33] and for NV-centers in nano-crystal diamonds [70]. In these experiments, however, the wire-crystal systems were not deterministically assembled thus rendering the rate enhancement estimation highly uncertain. By comparing an ensemble of uncoupled single emitters with an ensemble of coupled single emitters, they estimated rate enhancement factors of 1.7 [33] and 2.5 [70].

In this chapter, we demonstrate the controlled coupling of a single NV-center in a diamond nano-crystal to a surface plasmon mode propagating along a silver nanowire. The wire-crystal system is deterministically assembled by the use of an AFM. This approach allows us to directly compare the emission properties of a particular NV-center in a homogeneous dielectric environment with the emission properties of the same emitter but placed in the near vicinity of a silver nanowire supporting a propagating surface plasmon mode. The coupling to the propagating surface plasmon mode is

evidenced by a decrease in the emitter lifetime and the emission of a single photon is verified by a measurement of the second-order correlation function.

3.1 Experiment

First, the sample was prepared on a plasma cleaned fused silica substrate. The nano-diamonds with sizes < 50 nm were spin coated on the sample. Chemically grown silver nanowires with the diameters in the range $50 - 70$ nm and the lengths in the range $1 - 10$ μm fabricated by a polyol reduction process of silver nitrate, described in Appendix A, were subsequently spin-coated on the substrate resulting in a sufficient number of individual and well separated nanowires.

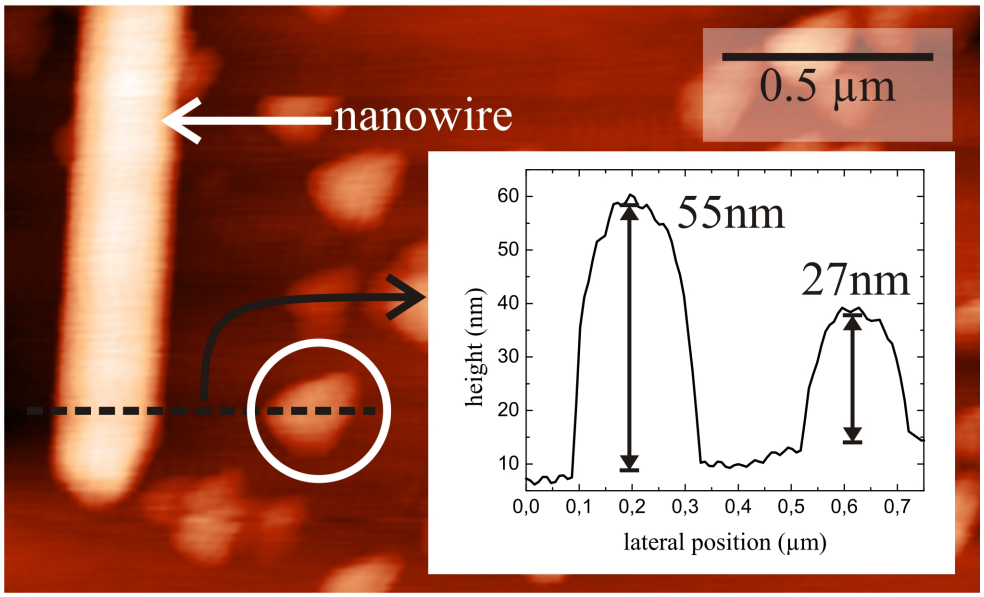

Figure 3.1: AFM topography of the nanowire and the nano-diamond containing the investigated NV-center (white circle). The inset shows the height profile of the wire and the diamond, taken along the black dashed line.

We started the experiment by recording a fluorescence image with APD_1. The AFM topography image of the same area was then used to locate a suitable nano-diamond containing a single NV-center. This diamond was separated from other diamonds and brought near the nanowire for characterizing the NV-center in a dielectric environment. At this step of the experiment, the diamond was still well separated from the silver nanowire, as illustrated by the AFM-topography image shown in figure 3.1. In the inset

of figure 3.1 we present the height profile of the silver nanowire and the diamond, which at maximum were measured to be 55 nm and 27 nm, respectively. The length of the nanowire was measured with the AFM to be about 2.8 μm. With the diamond in this position, we measure the decay time τ_0 of the NV-center's excited state, which is shown by the black dots in figure 3.2. A single exponential fit yields an excited state lifetime of $\tau_0 \approx 17.3 \pm 0.1$ ns. The measured second order correlation function $g^2(\tau)$ of this NV-center is presented by the black dots in figure 3.3 and the red line is a best fit to the data using the model described in chapter 2. The emission of single photons is clearly confirmed by the fact that $g^{(2)}(0)$ is well below 0.5. By measuring the fluorescence count rate as a function of the linear polarization of the pump beam, we verified that a large component of the NV-center's dipole moment is aligned perpendicular to the nanowire axis [71, 23].

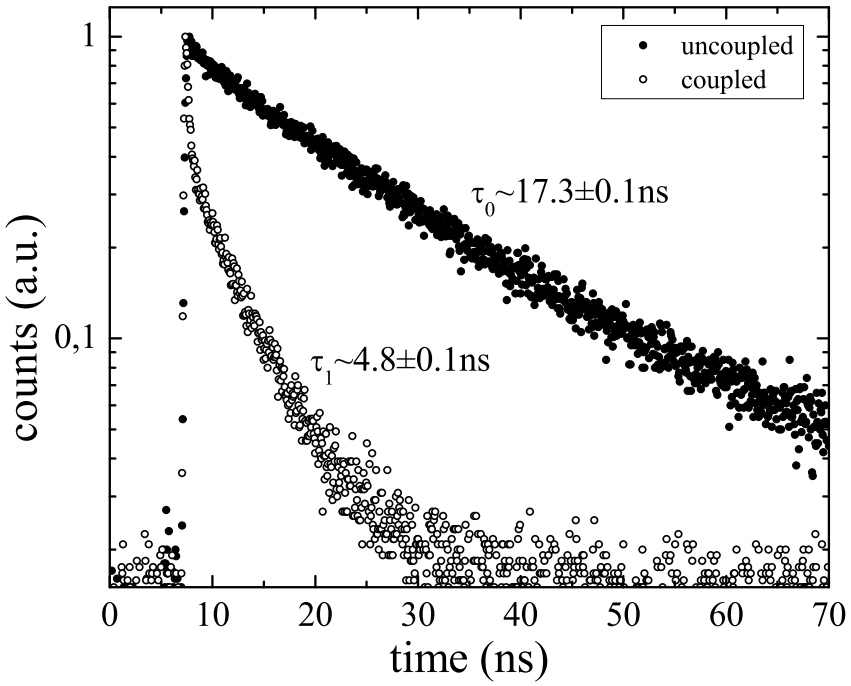

Figure 3.2: Fluorescence lifetime measurement of the uncoupled NV-center in a dielectric environment (black dots) and of the same NV-center after it has been coupled to the propagating SPP mode of the silver nanowire (open circles).

As a next step, we carefully pushed the nano-diamond in the very close proximity of

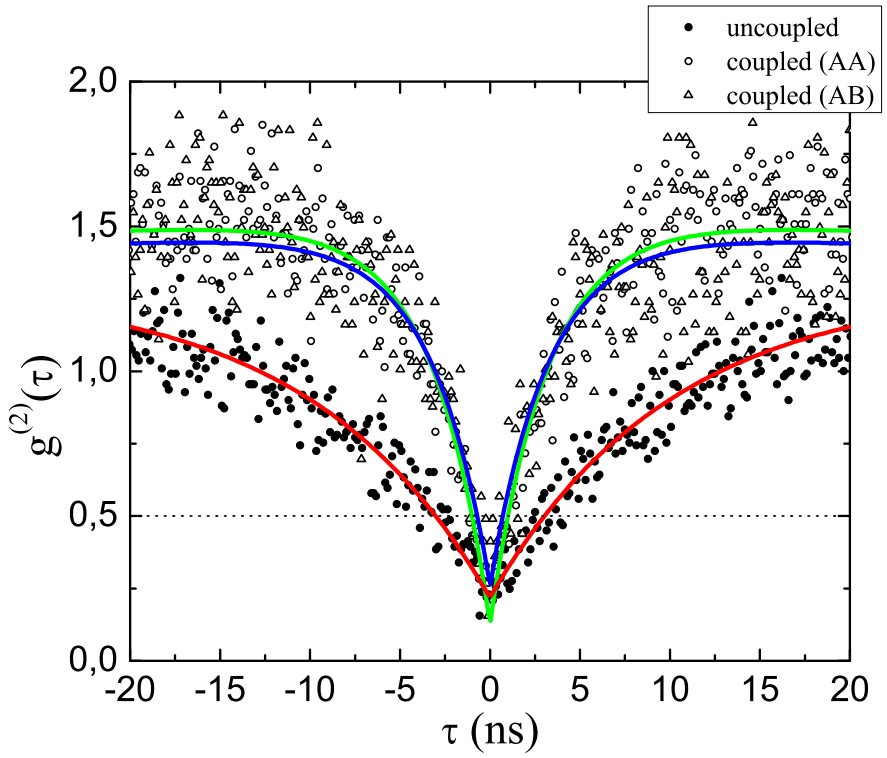

Figure 3.3: Second order correlation function measurement of the uncoupled NV-center (black dots) and the coupled NV-center with both detectors aligned to spot 'A' (open dots) and APD1 aligned to spot 'A' and APD2 aligned to spot 'B' (open triangles). The lines are a best fit to the data: red - uncoupled, green - coupled AA, and blue -coupled AB.

the nanowire by operating the AFM in contact mode. The final position of the nanodiamond near the silver nanowire is indicated by the white arrow in the AFM topography image shown in figure 3.4(a). The NV-centers dipole moment was still largely aligned perpendicular to the nanowire axis, which was verified by a new measurement of the count rate as a function of the linear polarization of the pump beam. As a consequence, the NV-center was in a changed dielectric environment compared to its previous position. This is witnessed by the decrease of its excited state lifetime, as shown by the open circles in figure 3.2. Directly compared to the lifetime τ_0 of the NV-center in its previous position, we measured a decrease of the excited states' lifetime of the coupled system τ_1 by a factor of $\tau_0/\tau_1 \approx 3.6 \pm 0.1$. In the vicinity of the nanowire, the NV-center does not only radiate to the far field, but also couples to the propagating plasmonic mode of the silver nanowire [27].

Evidence for the excitation of the propagating plasmonic mode is given by the fluorescence image recorded with the detector APD_2, which is shown in figure 3.4(b). This image has been obtained by continuously exciting the NV-center while scanning the image plane using the galvanometric mirror. Two emission spots can be seen in figure 3.4(b). The emission spot labeled as 'A' in figure 3.4(b) comprises the radiative emission from the NV-center together with emission from the nearby nanowire end face. Spot 'B' in figure 3.4(b) only comprises emission from the far nanowire end face. The intensity measured from spot 'B' is thus proportional to the coupling of the NV-center to the propagating plasmonic mode [27, 33, 70]. However, an exact estimation of the NV-center coupling to the propagating plasmonic mode by measuring the intensity of spot 'B' is difficult due to plasmon propagation losses along the nanowire and the complex reflections at the nanowire end face in conjunction with the broad emission spectrum of the NV-center.

The $g^{(2)}(\tau)$ function measurement with the detectors APD_1 and APD_2 being both aligned on emission spot 'A' is shown by the open dots in figure 3.3. With the open triangles we present the $g^{(2)}(\tau)$ function measurement between emission spot 'A' and 'B'. The green and blue line represent a best fit to the data for both measurement realizations. In both cases, a $g^{(2)}(0) < 0.5$ confirms the generation of single photons, and the excitation of *single* propagating surface plasmon modes is confirmed by the correlation measurement between spot 'A' and 'B'.

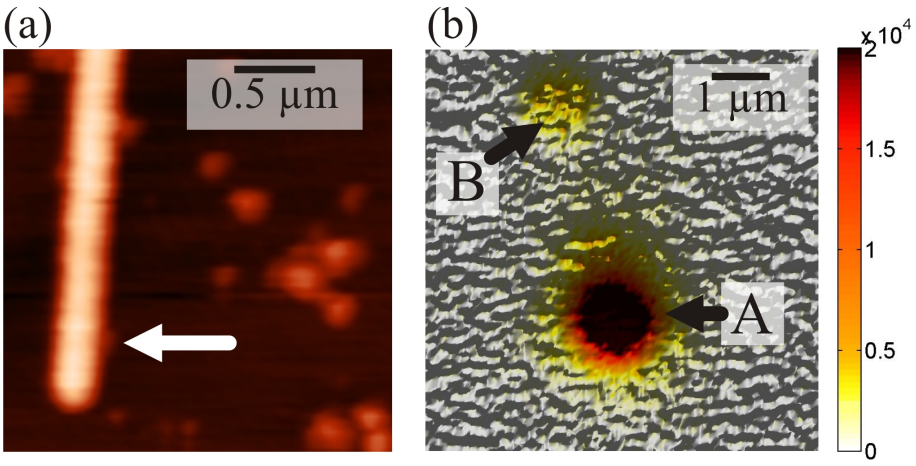

Figure 3.4: (a) AFM image taken after the nano-diamond has been located near the wire. The location of the diamond is indicated by the white arrow. (b) Photoluminescence image of the coupled NV-center nanowire system, taken while continuously exciting the NV-center, scanning the sample with the galvanometric mirror and recording the signal with APD2. Encoded in the color scale is the APD signal in counts/s.

3.2 Theoretical Estimation of Enhancement Factors and Comparison with Experiment

We compare our experimental results with theoretical predictions [66, 28]. We first use an approach which uses quasi-static approximation for calculating the decay rate enhancements [28]. We also use the approach that has been described in chapter 2 to obtain the rate enhancements. We then compare the experimentally obtained decay rate enhancements to the enhancements calculated using the two approaches.

In order to account for the relatively high refractive index of diamond, the electric permittivity of the dielectric medium ϵ_1 surrounding the nanowire was set to 3 in the calculations done using quasi-static approximation. In figure 3.5(a), the rate enhancements for a silver nanowire diameter of 55 nm is presented. One can observe that the radiative decay rate is the dominating part when the distance between the emitter and surface of the silver wire (d') is larger than 30 nm. For the d' between 5 nm and 30 nm, the plasmonic decay channel dominates. And, if d' becomes smaller than 5 nm, the non-radiative channel dominates. We also noted from our calculations using quasi-static approximation that the non-radiative decay rate depends only on the distance from the silver nanowire surface and not on the nanowire diameters.

For the nanowire diameter of 55 nm and a diamond height of 27 nm we expect a total rate enhancement of 4.21 from these calculations, assuming that the NV-center is located at the maximum position of 27 nm away from the nanowire surface and that the NV-centers dipole moment is aligned parallel to the radial electric field component $\mathbf{E}_r$ of the propagating plasmonic mode. This expected rate enhancement is close to our experimental result of 3.6 ± 0.1. We emphasize that only for parallel alignment of the NV-centers dipole moment to $\mathbf{E}_r$, an efficient coupling to the propagating plasmonic mode is achieved, since for the relevant range of parameter $|\mathbf{E}_z| \ll |\mathbf{E}_r|$, where $\mathbf{E}_z$ is the plasmon electric field along the nanowire axis.

In figure 3.5(b), the total decay rate enhancement as a function of the nanowire diameter and d' is shown. In figure 3.5(c), we present the total decay rate enhancement and the decay rate in plasmonic channel optimized over d' for the maximum β-factor for different nanowire diameters. The optimum d' is plotted in figure 3.5.

It has been shown that the quasi-static approximation underestimates the decay rate enhancements [66]. Also, in quasi-static approximation approach, we assumed a uniform dielectric environment surrounding the nanowire. The assymetric environment surrounding the nanowire also makes the plasmonic mode in the nanowire assymetric. This can be observed from figure 3.6(a), where we plot real part of the z-component of the normalized Pointing vector $P(x,y)_z = (\mathbf{E} \times \mathbf{H}^*)_z$ in the transverse plane (x,y) of a silver nanowire of diameter 55 nm. The coupling between the emitter and plasmonic mode depends on the mode localization and the electric field distribution of the plasmonic mode in the transverse plane. We therefore calculate the rate of emission into the plasmonic mode using the procedure described in Chapter 2. We calculate the decay rate into the plasmonic mode normalized to the decay rate when the emitter is placed in vacuum (Γ_{pl}/Γ_0) at a distance equal to the height of the nanodiamond, assuming the dipole moment alignment along the electric field. This we project as the minimum enhancement of decay rate because on top of plasmonic enhancement, the decay rate can also be enhanced by nonradiative and radiative decay channels. However, we note that decay into the nonradiative channel is much less than that compared to plasmonic enhancement, for the relatively small enhancements we have observed experimentally. In figure 3.6(b) we plot the magnitude of the decay rate into the plasmonic mode, normalized to the decay rate in vacuum, for a nanowire diameter of 55 nm.

In Table 3.1, we summarize the relevant physical parameters for various NV-center coupled to silver nanowire systems that we have successfully assembled. For all realizations, we observe the excitation of a single surface plasmon, confirmed by $g^{(2)}(0) < 0.5$. The

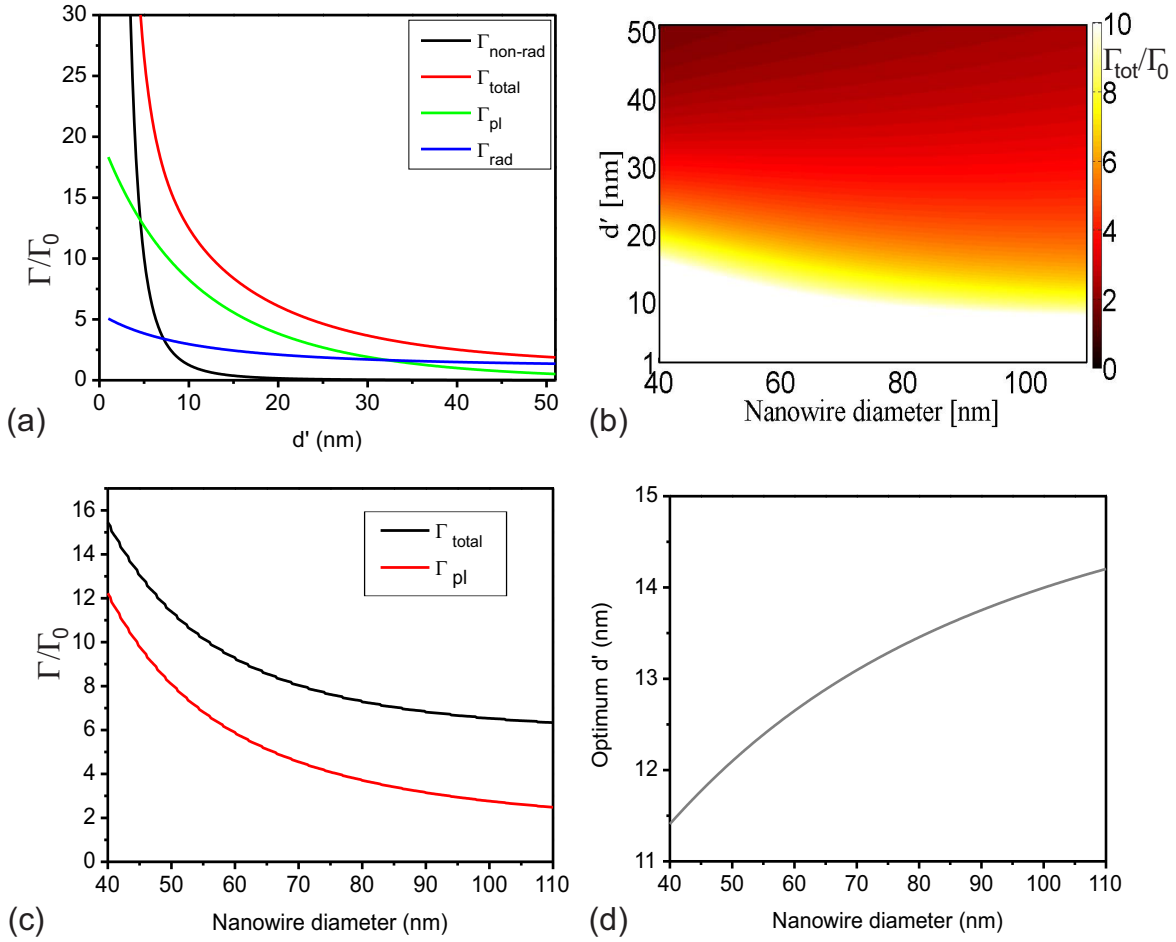

Figure 3.5: (a) Rate enhancements calculated for a wire diameter of 55nm as a function of distance from the surface (d') of the wire. (b) Total decay rate enhancements plotted as a function of nanowire diameter and d'. (c) Optimum enhancement factor, and (d) Optimum d', plotted as a function of the nanowire diameter.

Table 3.1: Summary of the relevant physical parameters for successfully assembled NV-center/nanowire systems.

nanowire diameter (nm)	diamond height (nm)	*total rate enhancement* τ_0/τ_1	min. expected rate enhancement	Γ_{pl}/Γ_0
55	27	**3.6±0.1**	4.21	8.39
65	45	*4.6±0.1*	2.27	3.45
60	40	*2.9±0.1*	2.56	4.34
51	40	*4.4±0.2*	2.48	4.66
63	17	*3.6±0.1*	6.74	13.12
50	35	*4.2±0.1*	2.98	5.78

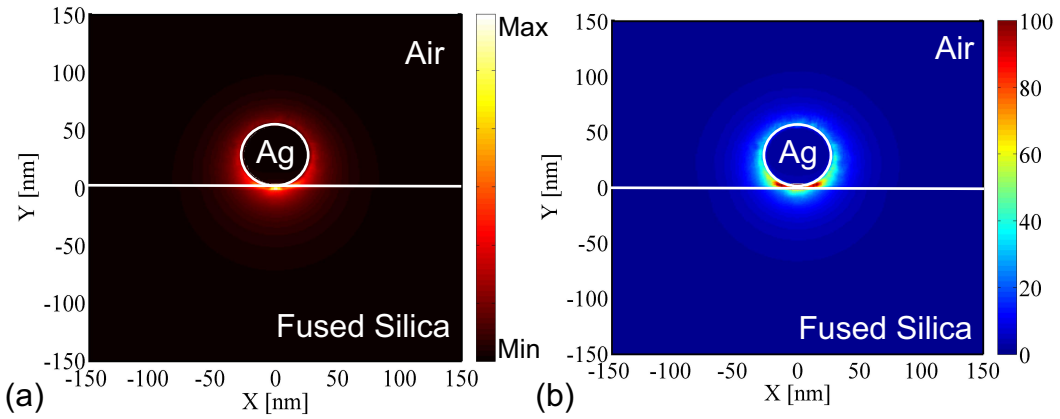

Figure 3.6: (a) The z-component of the pointing vector plotted for the plasmonic mode of a silver nanowire lying on fused silica substrate. (b) Maximum decay rate into the plasmonic mode plotted for the nanowire normalized to decay rate when the emitter is placed in vacuum ($\Gamma_{\mathrm{pl,\ max}}/\Gamma_0$).

coupling to the propagating plasmonic mode was witnessed by rate enhancement factors τ_0/τ_1 and verified by the observation of photon emission from the nanowire distal ends. In addition to the experimentally obtained rate enhancements we also present the minimum expected rate enhancement calculated using the quasi-static approximation and the numerical method in columns four and five of Table 3.1, respectively. We can observe from the table that the rate enhancements calculated using quasi-static approximation is smaller than that calculated using the numerical method. The discrepancy between the measured and calculated decay rate enhancements can be explained by difference in assumed dipole orientation, the position of the NV-center in the nanodiamond and the broad spectral width of NV-center emission.

3.3 Outlook and Conclusion

In view of improving the coupling efficiency of the NV-center to the plasmonic mode of a single silver nanowire, it is necessary to decrease both the diameter of the nanowire and the size of the diamond as can be observed from figure 3.5(c). Thinner nanowires can, for instance, be obtained by an optimization of the nanowire fabrication process described in Appendix A. We have found experimentally, that nanowires made by electron beam lithography and metal deposition are not suitable for coupling single NV-centers to their propagating plasmonic mode. This is presented in Appendix B in this thesis. Fluorescence from those nanowires largely overlaps with the emission spectrum of an NV-center, which as a direct consequence limits the possibility of detecting single photons. Surface roughness of lithographically prepared nanowires further limits the propagation distance of plasmonic modes [6]. Nano-diamonds with sub-10 nm diameters containing single NV-centers with stable photon emission rates have recently been reported in the literature [55, 56]. However, we have found it difficult to move very small diamonds ($\approx 10\ nm$) with the tip of an AFM cantilever.

In conclusion, by the aid of an atomic force microscope we have nano-assembled a system comprising a single NV center in a diamond nanocrystal and a chemically grown silver nanowire. This method allowed us to directly compare the emission properties of a single NV-center in a uniform dielectric environment with the emission properties of the same emitter coupled to the nano-wire. An enhancement of an NV-center's decay rate by a factor of 4.6 is directly measured and the excitation of single surface plasmons is evidenced by the observation of single photon emission at the far end of

the nanowire.

[Note: The contents of this Chapter has been published [72]. However, in section 3.2 of this chapter, we have used the dielectric permittivity of silver ϵ_{Ag} from [64], whereas in the article [72] ϵ_{Ag} was taken from [73].]

Chapter 4

Coupling of NV-center to Gap Modes of Parallel Silver Nanowires

In chapter 3, we presented the results obtained for coupling between a single NV-center in a nanodiamond to a single silver nanowire. Coupling of individual quantum emitters to propagating plasmonic modes of single metallic nanowires has been achieved before as well [33, 70, 74]. However, the coupling efficiency of the emitter to the propagating plasmonic mode observed so far have been moderate. We have seen in Chapter 3 that the smaller diameter metallic nanowires couples more efficiently to an emitter. This is due to the localization of the mode, which results in an increasing local density of states ρ with decreasing wire diameters. Although ρ increases, the propagation losses become higher with decrease in the wire diameter. Also, the outcoupling from small diameter plasmonic nanowires becomes more difficult [27]. We here compare NV-center's coupling to a single nanowire and to the gap modes of two parallel silver nanowires. We assemble the coupled systems by manipulating nanodiamonds and silver nanowires with tip of an AFM cantilever. We also compare the two systems theoretically by estimating the strengths of coupling into their respective plasmonic modes. We demonstrate efficient channeling of emission from a single NV-center in a nanodiamond to a quasi-single mode plasmonic structure of moderate size.

4.1 Theory

In case of a single metallic nanowire located on top of a silica surface, the highest field intensities are found in the vicinity of where the nanowire touches the substrate

for the fundamental mode. This is illustrated in figure 4.1(a), where we plot the real part of the z-component of the normalized Pointing vector $P(x,y)_z = (\mathbf{E} \times \mathbf{H}^*)_z$ in the transverse plane (x,y) of the nanowire. This plot has been obtained for a silver nanowire of diameter 110 nm. The area of highest field intensities is difficult to access experimentally, i.e. when the aim is to place an emitter at the points of highest field magnitudes in order to excite the plasmonic mode. Coupling of a dipole emitter to a single nanowire, and to a 'dual nanowire system' are compared. 'Dual nanowire system' consists of two silver nanowires placed in parallel to each other with a few nanometers gap in between.

We do numerical simulations to compare the two systems: 'single silver nanowire' and 'dual silver nanowire'. The distribution of electromagnetic fields in the modes of the 'dual nanowire system' depends on the gap between two nanowires of the system. A pair of parallel metallic nanowires with a few nanometer gap in between them, supports two bound fundamental modes which we refer to as the symmetric (S) mode and the anti-symmetric (AS) mode, depending on the charge distribution of induced dipoles in the transverse plane of the two individual nanowires [75]. The highly confined AS mode, with a $(+.-)$ charge distribution, has its maximum field in the inter-gap area between the two nanowires, which is illustrated by a plot of the Pointing vector $P_{z,AS}(x,y)$ in figure 4.1(b). The S mode with a $(+.+)$ charge distribution has a mode profile with high fields at the interface between the nanowires and the substrate, as shown by the Pointing vector $P_{z,S}(x,y)$ in figure 4.1(c).

The decay rate into the plasmonic mode as a function of position coordinates, in a plane transverse to the propagation direction, is calculated using a numerical model introduced in chapter 2. We compare the coupling into the plasmonic modes of a 'dual nanowire system' to a single nanowire with the same diameter as each of the wires in the 'dual nanowire system'. In figure 4.1(d), we plot $\Gamma_{pl,max}$ (maximized over dipole moment orientations) resolved in the transverse plane for a single wire of diameter 110 nm. In figure 4.1(e) and 4.1(f), we plot $\Gamma_{pl,max}$ resolved in the transverse plane for a dual wire system with wires of diameter 110 nm and a gap of 9 nm for AS and S modes, respectively. Clearly, the coupling to the dual wire system is dominated by AS mode in the gap region. In this case, coupling to the AS mode is an order of magnitude higher in comparison to a single nanowire.

For single silver nanowires of diameters ranging from 45 nm to 130 nm the electric fields, magnetic fields, and the mode indices for the existing modes were calculated. After calculating the fields for the modes using FEM, we calculate the coupling to

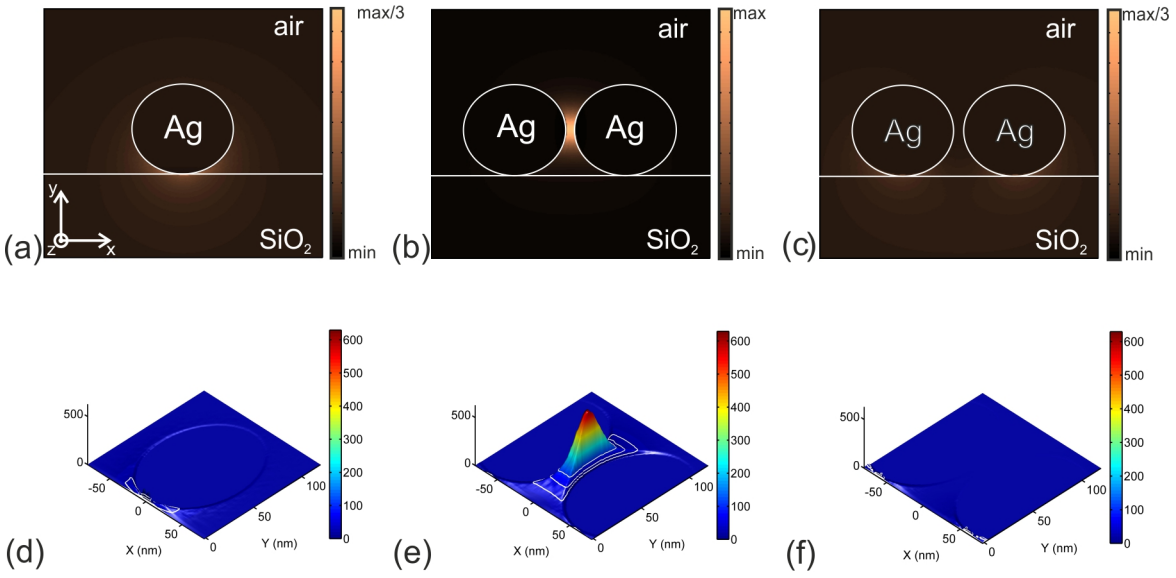

Figure 4.1: **Pointing vector and Decay rate into Plasmonic modes. (a)**, **(b)** and **(c)**, Normalized pointing vector of a single silver wire (a), the symmetric (b) and anti-symmetric (c) mode of a dual silver nanowire. **(d)**, **(e)** and **(f)**, Expected decay rate into the plasmonic mode(s) with respect to the rate in free space of a single silver nanowire (d) the anti-symmetric (e) and symmetric (f) mode of a dual silver nanowire. In all plots, the nanowire diameter is $110nm$, the substrate is fused silica glass and superstrate is air. The gap between the wires in (b), (c), (e) and (f) is 9 nm.

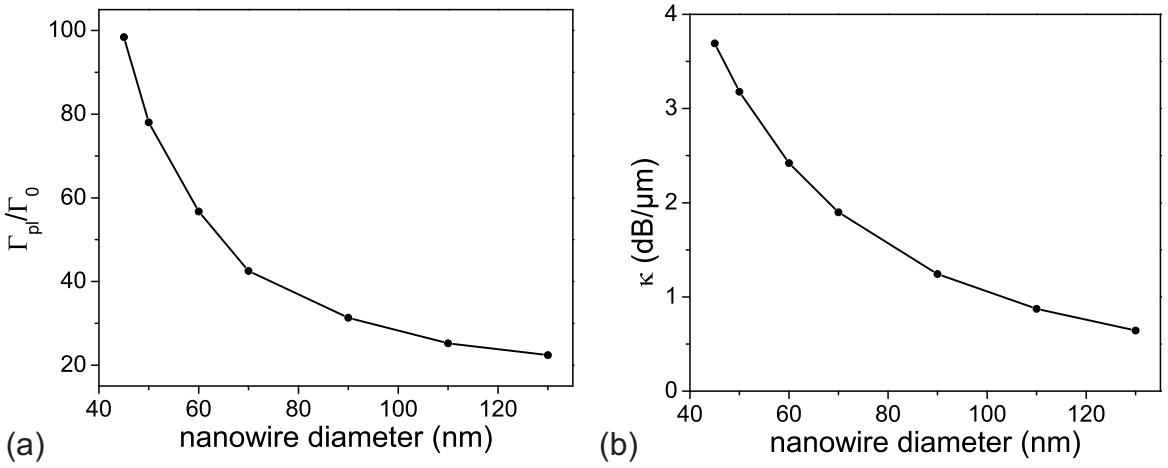

Figure 4.2: **Single Wire Plasmonic decay rates and Propagation losses. (a)** and **(b)** Total Plasmonic decay rate and Propagation losses, respectively, as a fuction of diameter of single nanowire.

the plasmonic mode as described in Chapter 2. If the emitter is placed very close to metal, the decay via nonradiative channel increases, as has been shown in Chapter 3. To calculate the maximum decay rates into the plasmonic channels, distances from the silver wire surface closer than 5 nm were not considered. Using mode indices obtained from the FEM simulations, the propagation losses were calculated for the plasmonic mode in single wires. In figure 4.2(a), the maximum coupling rate into the single wire mode as a function of the wire diameter is shown. The propagation losses as a function of the wire diameter is presented in figure 4.2(b).

For a range of wire diameters and gaps, the electric fields, the magnetic fields, and mode indices for the AS and S modes were calculated. From the fields and mode indices, propagation losses and maximum decay rate into corresponding modes were calculated following a similar procedure as in the case of the single nanowire system. In figures 4.3(a) and 4.3(b), the maximum decay rate and propagation losses, respectively, of the AS mode of dual nanowire system as a function of the gap size is plotted for different wire diameters. Similarly, figures 4.4(a) and 4.4(b) present the maximum decay rate and propagation losses, respectively, of the S mode of dual nanowire system as a function of the gap size plotted for different wire diameters. By comparing the losses of the fundamental mode in a single wire to the losses of the AS and S modes in figures 4.2(b), 4.3(b) and 4.4(b), it is clear that the losses of anti-symmetric and symmetric mode would become equal to loss in a single wire asymptotically, because if the wires are separated far apart, then the wires will have single wire modes instead

of AS and S modes of the dual nanowire system. For small gaps, the propagation loss is higher for the AS mode and lower for the S mode in comparison to the single wire of diameter equal to one of the wires in dual nanowire system. Similarly, the maximum decay rate of the AS and S modes would become equal to maximum decay rate in a single wire mode asymptotically, which can be seen by comparing figures 4.2(a), 4.3(a) and 4.4(a).

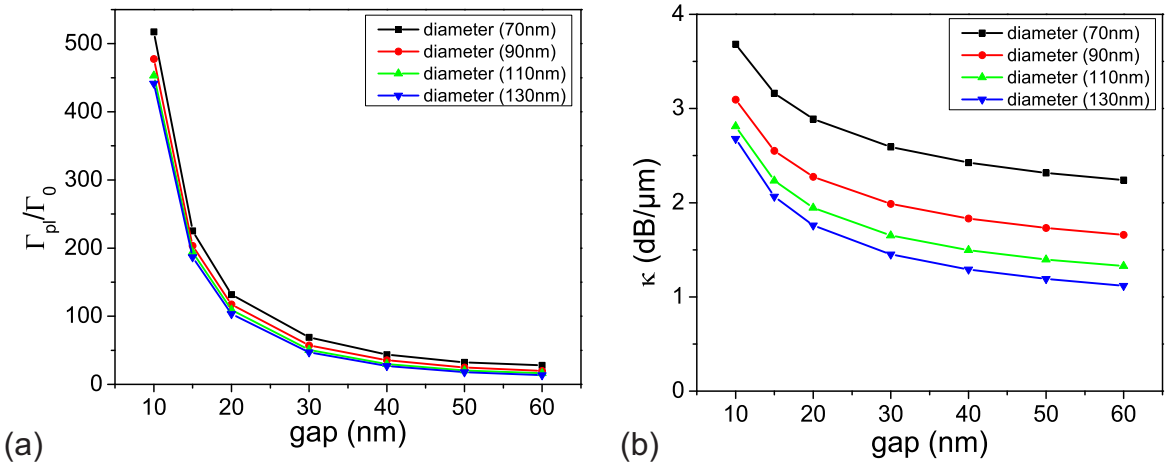

Figure 4.3: **Plasmonic decay rates and Propagation losses for the AS mode of dual wire system. (a)** Maximum Plasmonic decay rate and **(b)** Propagation losses as a fuction of the gap size between two nanowires for different diameters.

We now compare the single and the dual nanowire systems, when the gap and diameters are varied, for coupling to the plasmonic mode versus the propagation losses (κ). For single nanowires, the plotted range of κ corresponds to nanowire diameters of $d = 130$ nm at $\kappa = 0.64$ dB/μm till $d = 45$ nm at $\kappa = 3.69$ dB/μm. For realistic silver nanowire diameters and losses, only moderate maximum plasmonic decay rates $\Gamma_{pl,max}/\Gamma_0$ are expected while keeping κ low, as shown in figure 4.5. We also plot the maximum decay rate into the plasmonic modes of a dual nanowire system as a function of propagation losses for various nanowire diameters and gaps separating the nanowires in figure 4.5. Due to high localization in the inter-gap area, the AS mode is the dominating mode for plasmonic decays, which can be seen by comparing the intensities of the S and AS modes in figure 4.1(b) and 4.1(c), respectively. For wire separations > 30 nm, the excitation of plasmons occurs at a lower rate compared to the single wire case for similar propagation losses. In case the gap size is further decreased to values below 30 nm, the plasmon excitation rate exceeds the threshold given by the single nanowire case and can be more than the single wire threshold by around one

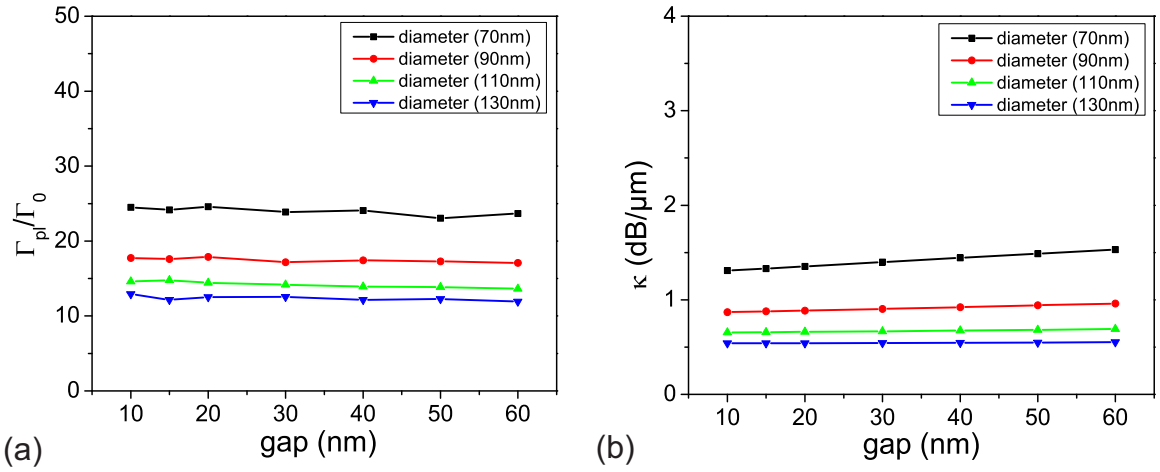

Figure 4.4: **Plasmonic decay rates and Propagation losses for the S mode of dual wire system. (a)** Maximum Plasmonic decay rate and **(b)** Propagation losses as a fuction of the gap size between two nanowires for different diameters.

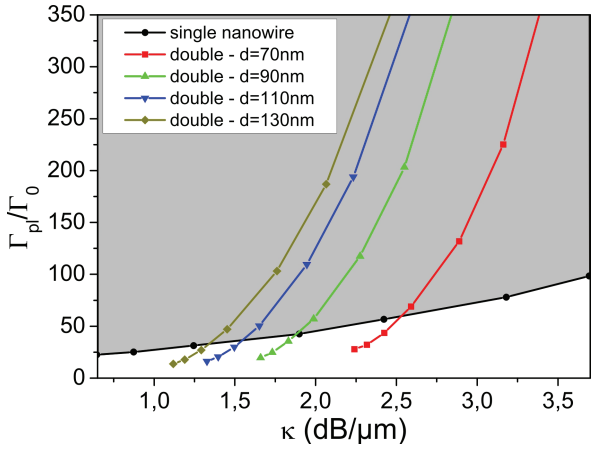

Figure 4.5: **Plasmonic decay rates as a function of Propagation losses.** Plasmonic decay rate as a fuction of propagation losses of the fundamental mode of a single silver nanowire as the diameter is changed. Total Plasmonic decay rate as a fuction of propagation losses of anti-symmetric mode on a 'dual silver nanowire system' as the gap is changed for different wire diameters. The inset shows colour codings for different curves.

order of magnitude for a gap of $\approx$ 10 nm. For gaps lower than 10 nm, the use of the bulk dielectric constant for silver becomes increasingly invalid [76], and therefore we do not compare the two systems for much smaller gaps.

4.2 Experiment

The sample for this experiment was prepared in a similar way as has been described in chapter 3. However, the silver nanowires used in this case had the diameters between 70 nm and 130 nm and lengths between 2 μm and 15 μm.

In this experiment, we first identified a silver nanowire with a length of $\approx$ 8 μm and a diameter of 110 nm. This nanowire was cut into two halves using the tip of an AFM cantilever. To cut the wire, length of the wire was measured and the midpoint was chosen. The AFM tip was pressed with a force of $\approx$ 1 μN on the fused silica substrate in contact mode operation of AFM, and it was moved at a high speed ($\approx$ 5 μm/s) across the wire. The wire was found cut. Then the lower part of the cut wire was moved slowly by touching the wire on the side at 10-12 points with the tip of AFM cantilever. The contact force between the substrate surface and AFM tip, when moving the wire was kept 10 times smaller, compared to when the wire was cut. In each step, the wire was moved by $\approx$ 0.1 μm. The area was scanned in semicontact mode operation of the AFM after every step of the wire movement. It took around 70 steps to move the wire to a position that is shown by figure 4.6(b), from a position where it was cut. The two wires were then located next to each other with a separation $>$ 0.5 μm between the wires.

We then located and characterized a diamond crystal with a height of 28 nm containing an NV center in the dielectric environment of the substrate-air interface. At this position, the diamond nanocrystal was still well separated from the nanowires, as shown in the AFM topography image in figure 4.6(a). This NV-center was characterized by a long lifetime $\tau_1 \approx 45.2$ ns , as shown by the black trace in figure 4.6(d). A measurement of the second order correlation function $g^{(2)}(\tau)$ verifies the emission of single photons, shown by the measured trace in figure 4.6(e). The crystal was then brought into the near vicinity of one silver nanowire. An AFM topography image of the resulting system is presented in figure 4.6(b). The NV center was thus coupled to the plasmonic mode propagating along the single nanowire. This is evidenced by the photon emission from the top ('B') and bottom ('C') wire ends shown in figure 4.6(c),

obtained while continuously exciting the NV-center. In addition to this, the NV centers lifetime decreased to a value of $\tau_2 \approx 11.9$ ns (see red trace in figure 4.6(d)), which yields a spontaneous emission rate enhancement of 3.8 relative to the emission in the environment of the substrate-air interface. A measurement of $g^{(2)}(\tau)$, which is shown in figure 4.6(f), verifies the preservation of single photon emission from the NV-center.

We then position the second wire (the one to the right in figure 4.6(b)) closer to the single nanowire - NV-center system such that the NV center lies in the gap between the closely spaced nanowires. Figure 4.7(a) shows an AFM topography image of the final *dual* nanowire - NV center system, where the location of the NV-center is indicated by the arrow. At the NV-center's position the gap between the wires was estimated to be ≈ 9 nm by measuring the distance between the highest points on the nanowires and relating it to the nanowire diameter of 110 nm. In figure 4.7(b), we present the photoluminescence image of the coupled NV center - dual wire system taken under continuous excitation of the NV center with the same power as used for the single wire case. In the double wire case, the emission from the wire ends is > 4 times higher than that in the single nanowire system, although the emission from the NV-center, spot 'A' in figures 4.6(c) and 4.7(b), remains the same. This results from a combination of two effects. First, the decay into the plasmonic mode of dual nanowire system is higher. Second, the outcoupling to the far field from the dual nanowire system from the ends is higher in comparison to single nanowire ends [77]. In addition to this, the NV centers lifetime after coupling to the dual nanowire system decreases to 5.4 ns, as shown by the blue trace in figure 4.7(c). Thus, with the realized *dual* nanowire system we demonstrate an increase of the spontaneous emission rate by a factor of 2.2 compared to the single nanowire system and a total factor of 8.3 compared to the emission rate when the nanodiamond containing NV-center was in the environment of the substrate-air interface.

Measurement results of the second order correlation function $g^{(2)}_{i,j}(\tau)$ of the dual nanowire system are presented in figure 4.7(d), where the subscripts i, j describe detector alignments to the emission spots $\{A, B, \text{and } C\}$ of figure 4.7(b). The black dots correspond to $g^{(2)}_{\mathrm{A,A}}(\tau)$, the red triangles to $g^{(2)}_{\mathrm{A,B}}(\tau)$, and the blue triangles $g^{(2)}_{\mathrm{A,C}}(\tau)$. A value of $g^{(2)}_{\mathrm{i,j}}(0) < 0.5$ verifies that all three radiation spots in figure 4.7(b) are due to the emission of single photons by the NV center.

We have also assembled a few more dual wire systems which are summarized in table 4.1.

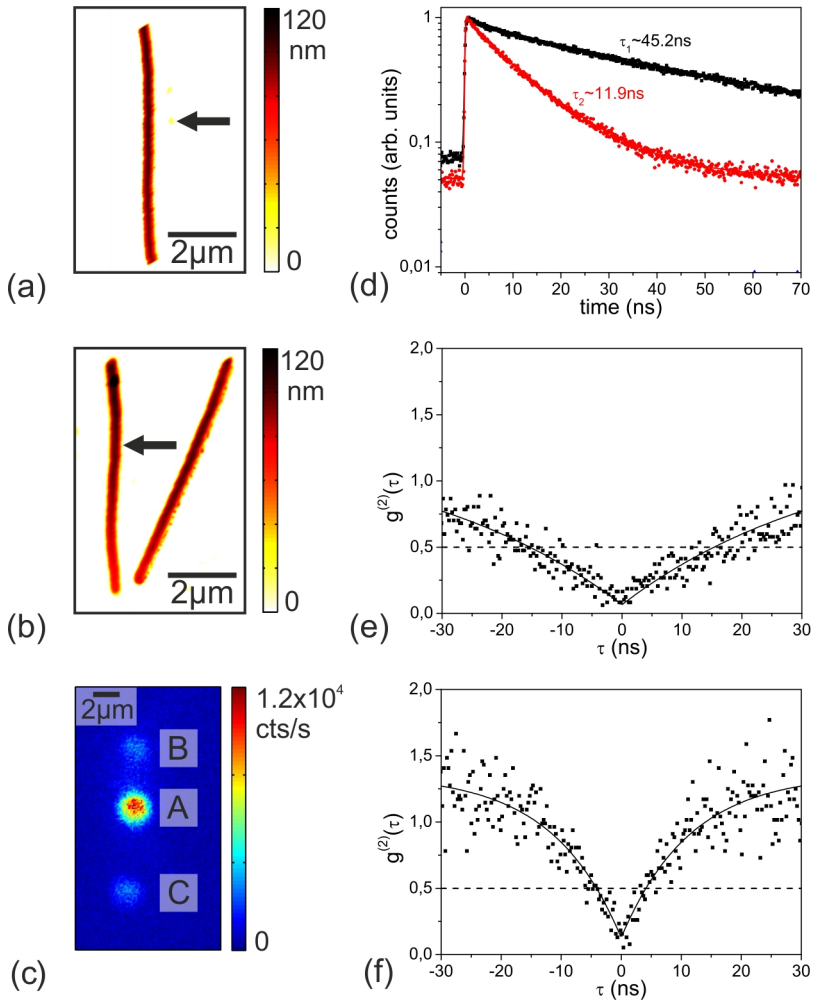

Figure 4.6: **Experimental results of coupling an NV-center to a silver nanowire of diameter 110 nm. (a)** and **(b)** AFM topography image of the single nanowire and the nano-diamond with a height of 28nm containing the NV-center. In further steps, the nano-diamond has been coupled to the single wire (b). In both the images, the location of the diamond containing an NV-center is indicated by the black arrow. **(c)** Photoluminescence image of the coupled NV-center - *single* nanowire system. Emission spot 'A' corresponds to radiative emission from the NV-center, while the spots labeled 'B' and 'C' correspond to emission from the upper and lower wire ends, respectively. **(d)** Lifetime of NV-center measured in the homogenous environment of the substrate (black trace) and after coupling to the single wire (red trace). **(e)** and **(f)** Second order correlation function $g^{(2)}(\tau)$ measurement of the NV-center in the dielectric environment of the substrate and the NV-center - *single* nanowire system, respectively. The curves are fits to the data.

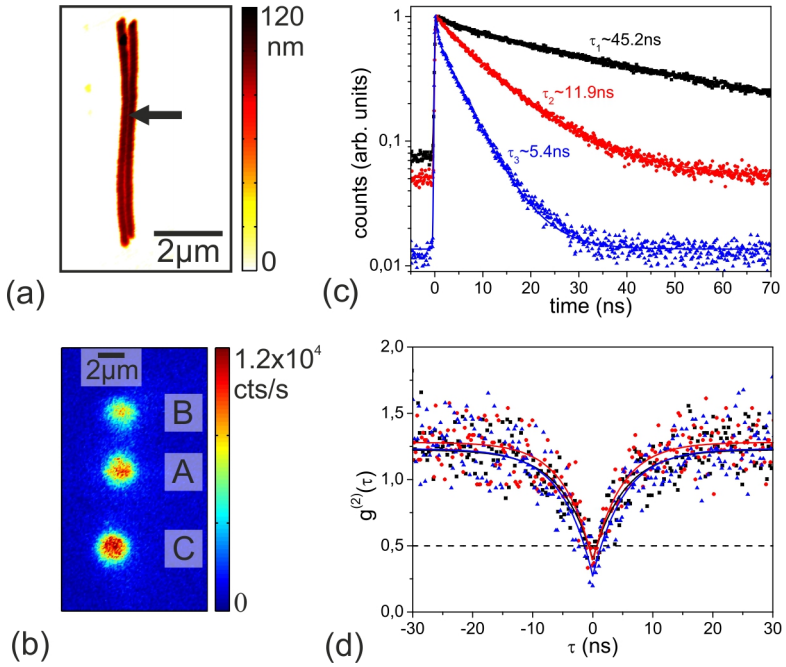

Figure 4.7: **Experimental results of coupling to the gap modes of two parallel silver nanowires.** **(a)** AFM topography image of two silver nanowires positioned close to each other with a few nanometers gap, forming the dual wire system. The location of the diamond containing an NV-center is indicated by the black arrow. **(b)** Photoluminescence image of the coupled NV-center *dual* nanowire system. Emission spot 'A' corresponds to radiative emission from the NV-center, while the spots labeled 'B' and 'C' correspond to emission from the upper and lower wire ends, respectively. **(c)** Lifetime of NV-center measured in the dielectric environment of the substrate (black trace), after coupling to the single wire (red trace), and after coupling to the dual wire system (blue trace). **(d)** Second order correlation function $g^{(2)}(\tau)$ measurement of the NV-center coupled to *dual* nanowire system. The dots correspond to measurements for which detector 1 was aligned to emission spot A and detector 2 to emission spot A (black), spot B (blue), and spot C (red) of the image shown in (b). The lines of same color as the dots are fits to the data.

Table 4.1: Summary of the relevant physical parameters of successfully assembled NV-center coupled to silver nanowire systems.

nanowire diameter (nm)	diamond height (nm)	*Single nanowire rate enhancement* τ_0/τ_1	Gap between nanowires (nm)	*Dual nanowire rate enhancement* τ_0/τ_2
110	28	3.8	9	8.3
130	70	1.82	61	3.0
90	35	1.83	57	3.3
65	29	2.89	69	3.3

4.2.1 Discussion of Experimental Results

In each of the realized coupled systems, the lifetime increased when the emitter was coupled to the dual wire system compared to when it was coupled to a single silver nanowire. One can also observe from Table 4.1, that the decay rate enhancements were not as high as expected from theoretical estimations. The rate enhancements depends on the gap, the position of the emitter as well as the orientation of the dipole moment with respect to the direction of the electric field of the plasmonic mode. When the gap was high, which applies for all the cases except for when the gap was 9 nm, the enhancements obtained were close to 3. In case of the system of 130 nm diameter nanowire, the gap size was limited by the size of the diamond. In other cases, the wires were damaged when they were moved closer. Therefore, the rate enhancements obtained are not as high as in the case of 9 nm gap. The position and orientaion of the dipole emitter as well as the size of the gap needs to be optimized for obtaining higher coupling efficiencies.

For a gap size of 9 nm and wires of diameter 110 nm, the β-factors for coupling to the AS mode of the 'dual nanowire system' as a function of position in the cross-section is shown in figure 4.8. The β-factors are calculated for the optimized orientation of the dipole, following the procedure described in Chapter 2. It can be observed from the plot of β-factors that the channeling of photons will be high if the emitter is placed in a region around the line of symmetry.

The tip of AFM cantilever has an angle of 18 degrees. When the nanodiamond was moved close to one nanowire, the nanodiamond was no longer visible in the AFM images, which means that the nanodiamond and the nanowire were touched by the tip tangentially. Using these conditions and assuming the nanodiamond shape to be

spherical, the position of the nanodiamond indicated in figure 4.8 was determined. From the plot of β-factors, the rate enhancement obtained experimentally, and the plasmonic decay rates shown in figure 4.1 - it can be concluded that the emission from the NV-center was enhanced mainly because of coupling to the AS mode .

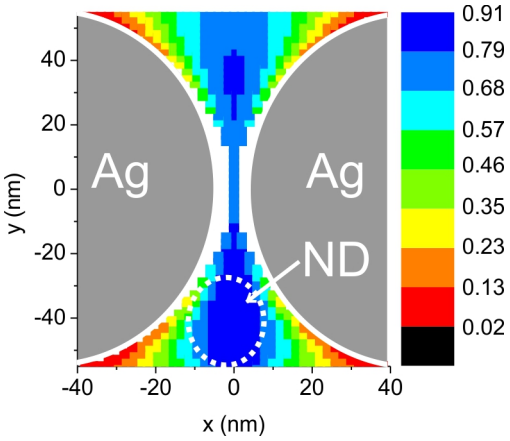

Figure 4.8: β-factor for coupling a dipole emitter to the AS mode of 'dual nanowire system' with nanowire diameter 110 and a gap of 9 nm. The position of the diamond is also indicated which is calculated from geometric contraints.

4.3 Conclusion and Outlook

We have compared coupling of a single NV-center to single and dual nanowire systems theoretically and experimentally. In each of the cases, the decay rate of the emitter increased when one more silver nanowire was placed in the vicinity of the first silver nanowire. We have seen theoretically that the coupling to such dual silver nanowire systems can be high. However, to obtain efficient coupling, the gap sizes needed are small (less than 30 nm). One needs to carefully assemble the system so that the NV-center lies in the optimum region of the gap mode, in order to observe high beta-factors in such systems. This should be possible with systems that can be made lithographically and if the emitter can be placed deterministically.

It should also be emphasized that the propagation losses of a dual nanowire system can efficiently be tuned by a variation of the gap size, which is similar to tapering of a single plasmonic waveguide [78]. A region of small gap might then be used for efficient plasmon excitation and a subsequent increased gap will lower the propagation losses and thus improve the device efficiency.

Chapter 5

Coupling of an NV-center to End-to-end Aligned Silver Nanowires

In the last two chapters, we have studied coupling between a single NV-center and propagating plasmonic modes when the emitter was placed in a plane transverse to the propagation direction of the mode. In this chapter, one part of the study is coupling of a single NV center in a nanodiamond to an end of a chemically synthesized silver nanowire. By placing a dipole emitter near to an end of a metallic waveguide of appropriate radius, at an appropriate distance, the decay rate of emitter can be enhanced and emission can be channeled into the metallic waveguide [27, 28]. We observe enhancement in decay rate of the NV-center as well as coupling to propagating mode of silver nanowire, when nanodiamond containing NV-center is moved close to an apex of single silver nanowire (SNW). Second part of our study is coupling of NV-centers in nanodiamonds to end-to-end aligned silver nanowires. This presents an alternative to coupling of an emitter by its placement in a plane transverse to the plasmon propagation direction. We observed futher enhancements in decay rates of the NV-centers coupled to end-to-end aligned SNWs when compared to single SNW. Emission from the distal ends confirmed coupling into the propagating modes in case of coupling to single SNWs as well as end-to-end aligned SNWs. We assemble the coupled systems by manipulating SNWs and nanodiamonds with the tip of an AFM cantilever. We also show, through simulations, that end-to-end aligned SNWs can be used as a controllable splitter for emission from a dipole emitter.

5.1 Estimation of Possible Coupling Strengths

In figure 5.1, we present the schematic structure of our systems under interrogation. The first system is an NV-center in a nanodiamond crystal coupled to the apex of a single SNW, whose side-view and top-view schematics are shown in figures 5.1(a) and 5.1(c), respectively. Similarly, figures 5.1(b) and 5.1(d) show the side-view and top-view schematics, respectively, of the second system, which comprises an NV-center in a nanodiamond coupled to end-to-end aligned SNWs. We note that in these figures the SNWs are cut short for presentational reasons; in the simulations and the experiments the wires are much longer (a few μms) than size of the nanocrystal. The coordinate system used in this chapter is also drawn in figure 5.1.

We have simulated the coupled systems using a finite element method in COMSOL, following the procedure described in Chapter 2. In the simulations, it is assumed that SNWs have a cylindrical shape with hemispherical ends. The radius of the SNWs is taken as 25 nm and the nanodiamond is assumed to have a spherical shape with a radius of 15 nm. The distance of the center of the nanodiamond from the edge of the SNW along the y-axis is set to 15 nm. In the case of end-to-end aligned SNWs, the gap between the wires equals the diameter of the nanodiamond. The refractive indices of diamond used for the simulations is 2.409. The material surrounding the dipole emitter also effects its decay rate [79]. Therefore, we normalize the decay rate enhancements of the coupled systems with decay rates of a dipole emitter inside the nanodiamond without SNWs, for each of the orientations and positions of the dipole. The decay rate enhancements obtained from the simulations for a dipole emitter coupled to a single and end-to-end aligned SNWs are presented in figure 5.2.

Figure 5.2(a) shows the decay rate enhancements when a nanodiamond with a dipole emitter is lying close to a single SNW. For various dipole orientations of the emitter lying in xy-plane inside the nanodiamond, the decay rate enhancements are plotted. The decay rate enhancements depend, in general, on the distance of the NV center inside the nanodiamond to the SNW. The closer the emitter to the SNW, the higher the enhancements. For a dipole emitter oriented along the x-axis, the decay rate can be either enhanced or suppressed, depending on the position of the dipole. In this case we obtained an enhancement of 3.98 and a suppression by a factor of 0.81. For dipole orientation along the y-axis, which is along the axis of the wire, the decay rates are highly enhanced. For a certain position, the enhancement obtained is as high as 73.0. For dipole emitter oriented along the z-axis, the decay rates are enhanced in general,

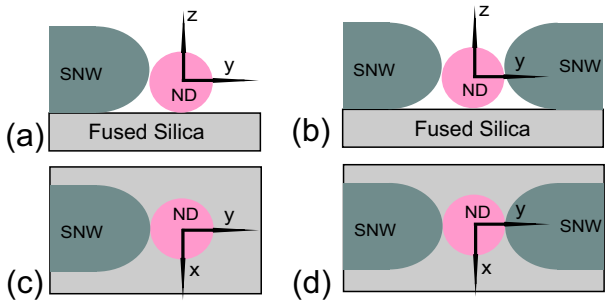

Figure 5.1: **(a)** and **(b)** Side view schematics of a coupled system of NV-centers in a nanodiamond to apex of an SNW and two SNWs placed end-to-end. **(c)** and **(d)** Top view schematics of a coupled system of NV-centers in a nanodiamond to apex of an SNW and two SNWs placed end-to-end. SNW: silver nanowire, ND: nanodiamond.

but the enhancements are smaller than that for the dipoles oriented along the y-axis. The enhancements in this case ranges from 1.38 to 8.68. Clearly, for dipole orientation along the y-axis, high enhancements can be obtained. We also calculated decay rate enhancements for different positions in the xz-plane for a y-oriented dipole, which is presented in figure 5.2(c). One can again observe that the decay rate enhancements are high if the NV-center is lying close to SNW, i.e. for positive z values.

The decay rate enhancements for the end-to-end aligned system is presented in figure 5.2(b) and 5.2(d). The position dependence of the decay rate enhancements becomes symmetrical about xz- and yz-planes, due to symmetry about these planes. Similar to the coupling of an emitter in a nanodiamond to single SNW, for x-axis oriented dipole emitter, the decay rate of the emitter can be either enhanced or suppressed depending on the position of dipole. In case of coupling to two SNWs, however, the enhancements and suppressions are higher, an enhancement of 4.0 and a suppression of 0.68 is estimated. For y-oriented dipole emitters, the enhancements are higher than that for a single wire coupling case, ranging from 40.8 to 103. For z-oriented dipoles also, the decay rate enhancements are higher when compared to single SNW coupled system, but the enhancements are smaller than that compared for the y-oriented dipoles. In figure 5.2(d), the decay rates in xz-plane for y-oriented dipoles show a pattern similar to the one obtained in the case of single SNW. However, the magnitude of decay rate enhancements are higher.

In general, it can be concluded from the simulations that the decay rate gets enhanced for a dipole emitter when it is brought closer to an SNW, and it gets further enhanced when the dipole emitter is placed in the gap between two SNWs. We now verify this

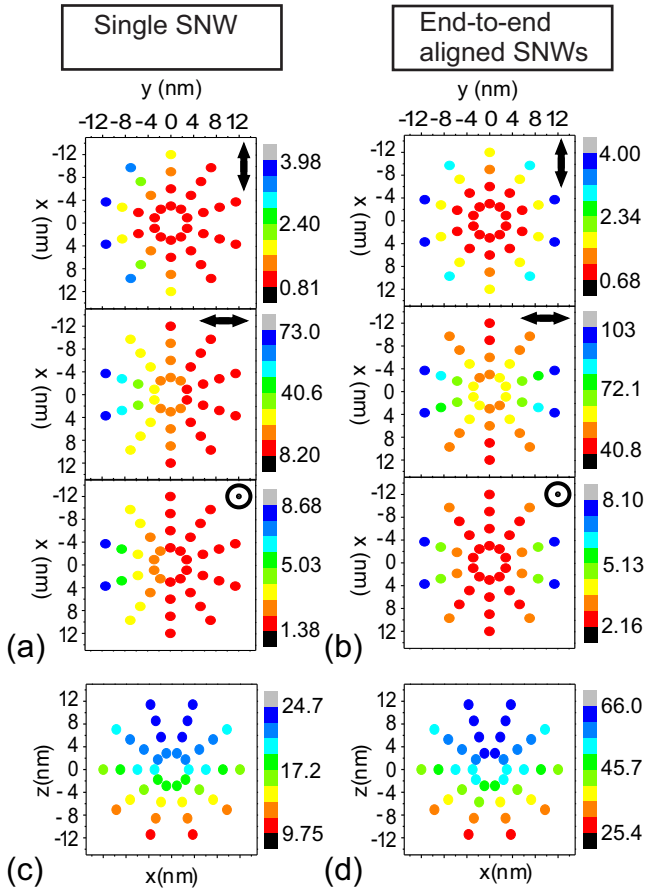

Figure 5.2: Simulation results showing decay rate enhancements as a function of position and orientation of the dipole. Decay rate enhancements are shown in color scale. All decay rate enhancements are normalized to a dipole emitter in a nanodiamond placed on glass substrate without SNWs. **(a)** and **(b)** Plots of decay rate enhancements for coupling of a dipole emitter in a nanodiamond to an SNW and two end-to-end aligned SNWs, respectively. The emitter is lying in xy-plane in the nanodiamond. The dipole orientations used for the simulations are indicated in the plots for various cases. **(c)** and **(d)** Plots of decay rate enhancements, for a dipole oriented along Y-axis in xz-plane for single and end-to-end aligned SNWs, respectively.

pattern of decay rate enhancement experimentally.

5.2 Assembling and Characterization of Coupled Systems.

For assembling and characterization of coupled systems, we use the homebuilt standard confocal fluorescence microscope in combination with an AFM, described in chapter 2. The sample was prepared in a similar manner as in Chapter 4. However, the nanodiamonds in this case had a mean diameter of 50 nm and a maximum diameter of 100 nm (microdiamant MSY 0-0.1).

5.2.1 Coupled System Consisting of an NV-center Placed Near to Apex of an SNW.

To make sure that the coupled system consists of a single NV-center in a nanodiamond and SNWs, we identified nanodiamonds containing a single NV-center lying close to the SNWs by matching the location of the fluorescence from the tip of the cantilever and fluorescence from the nanodiamond. Figures 5.3(a), 5.3(b) and 5.3(c) show AFM images of the SNWs and nanodiamonds containing NV-centers. Nanodiamonds containing single NV-centers are indicated by arrows in the corresponding figures. Fluorescence spectrum and experimentally measured data of the autocorrelation (for the nanodiamond indicated in figure 5.3(a)) are presented in figures 5.3(d) and 5.3(e), respectively. The fit to the experimental data for autocorrelation measurement is shown by the red curve in figure 5.3(e). We observe a clear dip in the $g^{(2)}$ function measurement with $g^{(2)} << 0.5$. Hence, we conclude that the NV-center indeed yields single photons in this case.

We push the nanodiamonds across the sample close to one end of an SNW by dragging the diamond with the AFM cantilever using the AFM in contact mode operation. Figures 5.4(a), 5.4(c) and 5.4(d) show AFM images of the nanodiamond-SNW system with a nanodiamond containing a single NV-center that has been moved close to one end of an SNW. The galvanometric scan of the fluorescence for the system shown in figure 5.4(a), taken by keeping the excitation spot fixed on the nanodiamond containing NV-center, is shown in figure 5.4(b). One can clearly see two spots, 'A' and 'B', in the fluorescence scan image. Spot 'A' comes from the NV-center emitting into free

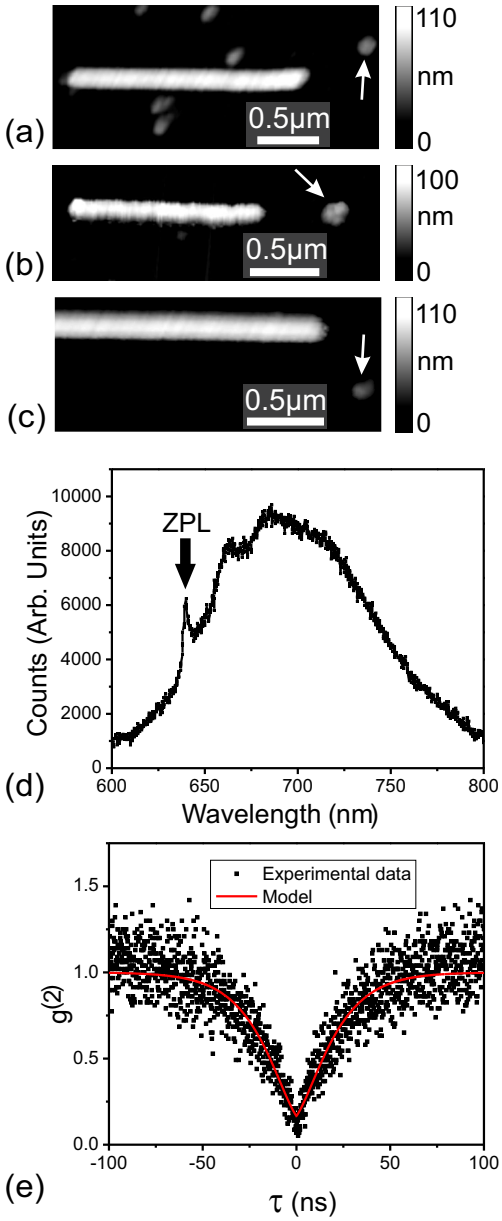

Figure 5.3: **(a)-(c)** AFM images of silver nanowires and nanodiamonds containing single NV-center placed closeby. **(d)** Spectra obtained for emission from an NV-center contained in the nanodiamond indicated in (a). **(e)** Autocorrelation measurement data and a model fit to the data for an NV-center contained in the nanodiamond indicated in (a).

Table 5.1: Decay rate modification when an NV-center is coupled to one nanowire end.

System number	SNW diameter (nm)	ND height (nm)	Decay rate enhancement
1	72	49	1.23
2	80	59	1.28
3	95	48	1.61

space modes whereas spot 'B' results from the coupling of the NV-center fluorescence into the plasmonic mode of the silver nanowire, its propagation to the distal end of the wire and the subsequent scattering of the plasmon into the far field. The lifetime measurement data for the NV-center indicated in figure 5.3(a) is shown by black dots in figure 5.4(e). We also measured the lifetime at the two spots, i.e. 'A' and 'B' shown in figure 5.4(b). The lifetime measurement data for the spots 'A' and 'B' is shown in figure 5.4(e). We see that there are two lifetime slopes (both for 'A' and 'B'). The very fast decay curve corresponds to fluorescence from the wire while the slow decay curve corresponds to fluorescence from the NV-center in nanodiamond. We observe a decrease in the lifetime for the single wire case by a factor of around 1.23. We note that the slow decay curve obtained from both spots, 'A' and 'B', are the same (within the small uncertainty limited by our measurement), indicating that the coupling of the NV center to the propagating mode of SNW does play a role.

The change in lifetime observed for 3 different systems consisting of different nanowires and nanodiamonds is summarized in Table 5.1. In all the cases, enhancement in decay rate was observed, and also the emission from the distal end verifies the coupling of NV-center emission into the propagating plasmonic mode of the SNWs.

5.2.2 Coupled System Consisting of an NV-center and Two End-to-end Aligned SNWs.

After coupling the NV-center to one end of a single SNW, we assemble one more SNW close to the nanodiamond containing an NV-center so that the two SNWs are aligned along a straight line with a small gap left between the ends of the two SNWs. The second SNW is either cut from the first nanowire, or it is a different nanowire. Figures 5.5(a), 5.5(c) and 5.5(d) show the AFM images of two wires aligned along a straight line with nanodiamond placed in the gap between the two nanowires. In the

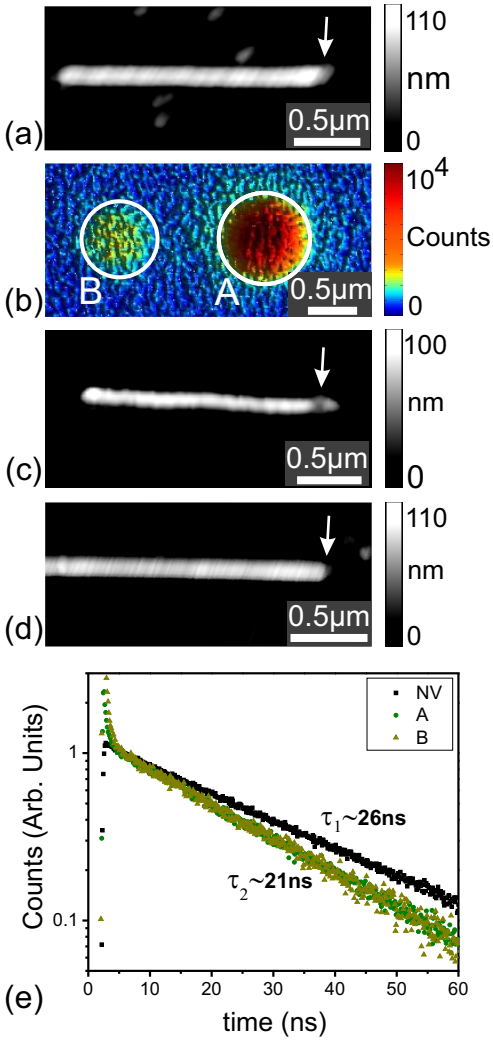

Figure 5.4: **(a)** **(c)** and **(d)** AFM images of nanodiamonds placed close to single SNWs. **(b)** Fluorescence image of the nanowire-nanodiamond system shown in figure (a), where excitation spot is the nanodiamond containing an NV-center. **(e)** Graph showing measurement data for change in lifetime when the nanodiamond containing NV-center is moved near to one end of the wire as shown in (a).

fluorescence image shown in figure 5.5(b), one can observe the fluorescence from three spots; 'D', 'E' and 'F'. 'D' is the spot corresponding to nanodiamond containing an NV-center, and 'E' and 'F' are the two distal ends of two wires. We also measure lifetime at the three spots by exciting the NV-center at spot 'D'. One can observe from figure 5.5(e) that the lifetimes for the spots 'D', 'E' and 'F' are the same, which indicates the excitation by the same NV-center. The emission from the spot 'F' is less than that from the spot 'E', even though end 'F' is closer to the nanodiamond than end 'E'. This happens due to the asymmetric placement of the NV-center inside the nanodiamond in the gap between two end-to-end aligned nanowires.

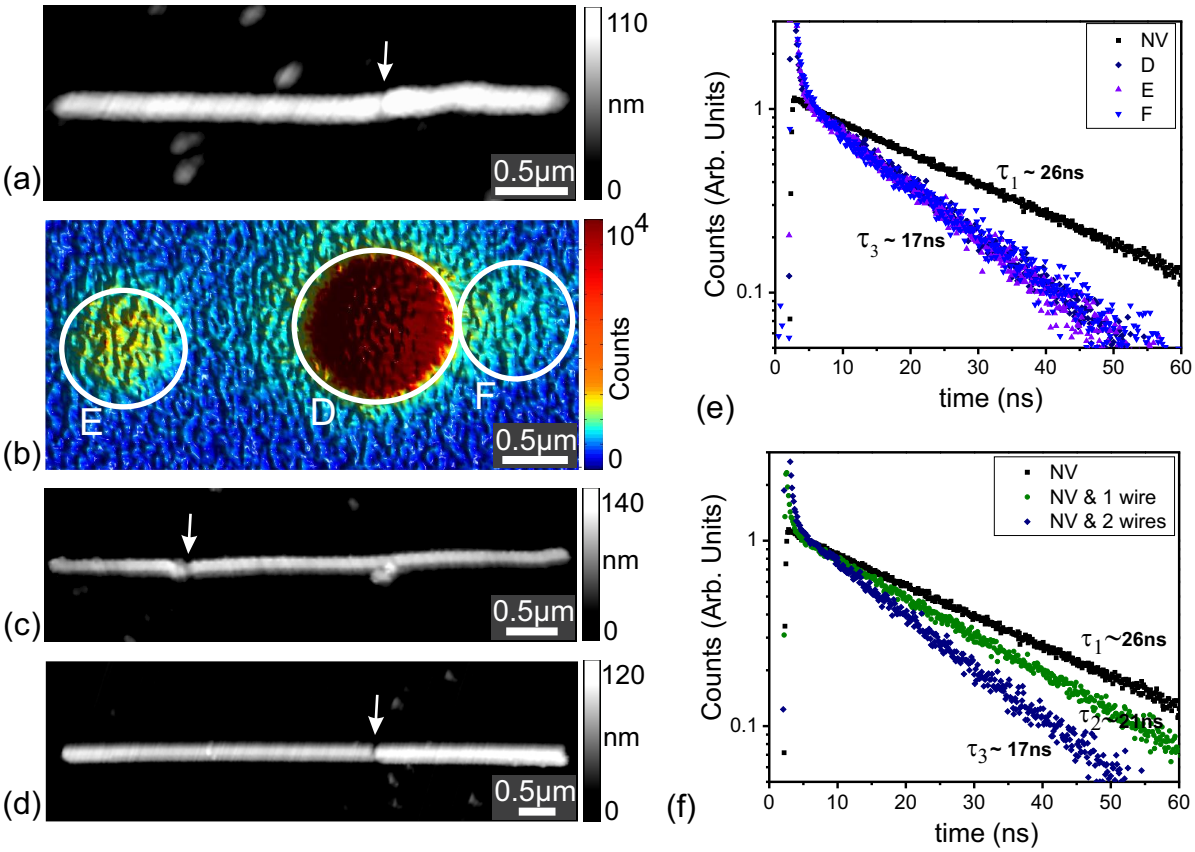

Figure 5.5: **(a), (c)** and **(d)** AFM images of end-to-end placed nanowires, and nanodiamonds containing single NV-centers placed in the gap. **(b)** Fluorescence image of the system shown in (a), when the excitation point is located near to the nanodiamond containing NV-center. **(e)** Graph showing measurement data for lifetimes from the three points shown circled in (d), and initial lifetime for the NV-center without coupling to SNWs. **(f)** Graph showing change in lifetimes when nanodiamond is not coupled to SNWs and when it is coupled to one and two SNW ends.

Table 5.2: Decay rate enhancements due to the coupling to end-to-end aligned SNWs, normalized to the decay rate of the NV-centers without SNWs.

System number	SNW1 diameter (nm)	SNW2 diameter (nm)	ND height (nm)	Decay rate enhancement
4	72	72	49	1.54
5	80	80	59	1.94
6	95	115	48	2.28

In figure 5.5(f), we have summarized the measured lifetimes observed for the NV-center in the nanodiamond in three diferrent conditions for the environment of the NV-center. We observe that the lifetime changed from 26 ns to 21 ns for coupling to a single nanowire which changed to 17 ns for coupling of the NV-center to two SNWs. In Table 5.2, we present the decay rate enhancements observed for different systems labelled by 4, 5 and 6. In systems 4 and 5, the radii of the two wires are the same, while in system 6, the second wire has a slightly larger diameter. In all these cases, we observed the decay rate enhancement of the NV-center with respect to the NV-center single SNW coupled system. And the coupling into the propagating plasmonic modes of both SNWs is also observed.

5.3 Controllable Emission Splitter

So far, we have presented change in decay rates of NV-centers. One more parameter of importance for the application of such coupled systems is the spontaneous emission β-factor, which is defined as the ratio of emission into a particular mode to the total emission including all the modes. In figure 5.6, we present theoretical predictions on the spontaneous emisison β-factors for coupling, when a dipole emitter is placed in the gap between two end-to-end aligned SNWs. The SNW diameter in this case is 25 nm and the gap between two SNWs is 34 nm. The blue and red curves in figure 5.6 represent β-factors for propagating modes of left and right SNWs, respectively. Clearly, emission into a particular SNW can be controlled and emission into two SNWs for end-to-end aligned SNWs is unbalanced depending on the position of the emitter. This is in contrast to coupling of an emitter to a SNW by putting the emitter in the transverse plane of the plasmonic waveguide, in which case the emission is always symmetrical in two opposite directions.

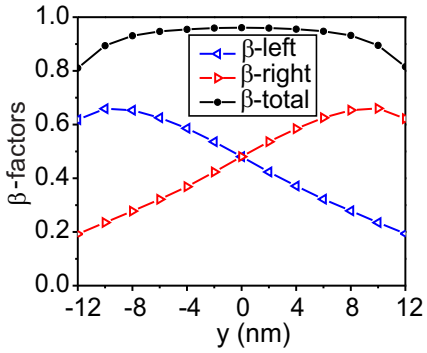

Figure 5.6: Spontaneous emission β - factor for coupling to the two SNWs which are aligned end-to-end. Black curve shows the total β - factor ($\beta_{left} + \beta_{right}$), whereas blue and red curve shows β - factors for coupling to left and right SNW respectively.

5.4 Conclusion and Outlook

In this chapter, we have shown theoretically that coupling of dipole emitters to the plasmonic modes of silver nanowires can be high, if the ends of two SNWs are placed so that a very small gap is left in between. It substantially depends on the orientation and position of the dipole with respect to wires as well. We have expermentally observed enhancement in deacy rate when the NV-center in nanodiamonds are placed close to an end of a single wire, which is further enhanced when placed in the gap between two end-to-end aligned nanowires. We also verified the emission from the two nanowires' end by comparing the lifetimes measured from the NV-center spot directly and the lifetime of the emitter measured from the ends of the SNWs.

We have used the ends of the chemically grown silver nanowires, which may not have the most optimum shape of its ends for coupling of a single emitter to its propagating plasmonic modes. Coupling to the SNWs can be improved substantially by structuring the ends of SNWs better, and by placing the NV-centers at optimum positions.

Chapter 6

Fabrication of Designed Single Crystalline Silver Nanostructures

So far we have used single-crystalline nanowires of silver with exquisite propagation properties that have been fabricated using chemical synthesis. The drawback, however, of this fabrication method is that predesigned structures cannot be made. To develop nanocircuitry for controlled light guiding and enhanced coupling, another method must be considered. The standard approach for obtaining the desired metallic nanostructures has been electron-beam lithography followed by thermal evaporation of metal. This method, however, results in polycrystalline metallic nanostructures which leads to severe scattering of a propagating field from the grain boundaries [6]. Thermal evaporation of metal is thus unsuitable for the fabrication of low loss metallic nanocircuitry.

For chip based realizations of quantum information processing [25], one needs to make miniaturized plasmonic circuits. As a result of the strong field confinement and thus field enhancement, the requirements on the fabrication of the nanostructures become very critical. Nanometer sized defects in the fabrication process may result in unwanted scattering centers leading to poor optical performance in terms of increased optical losses [6]. Therefore, to circumvent such detrimental effects, it is important to develop a fabrication method that produces single-crystalline structures with atomically smooth surfaces.

Recently, a different and very promising method that combines bottom-up and top-down approaches has been applied to fabricate complex, single-crystalline nanostructures of gold [80]. Single-crystalline gold plates were produced using chemical synthesis [81] and, subsequently, the desired structure was formed by the use of focused ion

beam (FIB) milling. Using this method, they showed a dramatic increase in the surface smoothness of some gold nanoantennas. However, due to the high intrinsic losses of gold, the losses in these structures remained large. These losses are in particular large in the visible and near-infrared optical spectrum, due to the relatively low plasma frequency and high interband transition strengths of gold [73, 5]. On the other hand, the intrinsic loss of silver is much lower and is therefore a more natural choice in many applications.

In this chapter, we describe fabrication and characterization of predesigned single-crystalline nanostructures made of silver. Using chemical synthesis and FIB milling we make nanowires and nanotips with prespecified dimensions and with a high degree of smoothness. Finally, we demonstrate the propagation of plasmons and the creation of a cavity effect in the fabricated nanowires.

6.1 Chemical Synthesis of Silver Nanoplates

The first step in producing single-crystalline and designed silver nanostructures is the fabrication of silver nanoplates (SNPs). Various chemical procedures have been followed to synthesize such SNPs [82, 83, 84, 85]. In all these previous accounts, however, the SNPs were either too small [85] or too thick [82], to allow for the carving of nanoplasmonic circuits from them. We synthesize single crystalline SNPs of average thickness of around 65 nm and with areas of around 100 μm^2 by modification of a process [82], which was previously used to synthesize silver plates of thicknesses of about 0.5 μm. All the chemicals used to make the SNPs were purchased from Sigma-Aldrich. Our chemical process starts by preparation of solutions of 100 mg silver nitrate ($AgNO_3$) in 30 ml deionized (DI) water, 15 mg of iron sulfate heptahydrate ($FeSO_4 \cdot 7H_2O$) in 30 ml DI water, and 200 mg of polyvinyl pyrollidone (PVP-K30) in 40 ml of DI water. These solutions were cooled to temperatures between 8 and 20 degrees celcius. The silver nitrate solution was then put into a conical flask at room temperature and 3.6 mg of H_2SO_4 was added to the solution. Then the PVP-K30 solution was added to the mixture, followed by addition of the $FeSO_4 \cdot 7H_2O$ solution. The reaction was run for 3 hours at room temperature under continuous stirring using a magnetic stirrer. Then the solution was centrifuged at 4000 rpm for half an hour, and SNPs were obtained as precipitate. The SNPs thus obtained were washed twice with ethanol and once with water. After washing, the SNPs were stored dissolved in water. We also made SNPs us-

ing different weights of $FeSO_4 \cdot 7H_2O$, where 50 mg, 100 mg and 150 mg of $FeSO_4 \cdot 7H_2O$ (referred to as processes 2, 3 and 4, respectively, in the following discussion) was used instead of 15 mg of $FeSO_4 \cdot 7H_2O$ (referred to as process 1 in the following discussion).

6.2 Characterization of Silver Nanoplates

To characterize the dimensions of the SNPs thus obtained, the solutions containing SNPs were spin coated on a fused silica substrate, and AFM images of SNPs were taken. AFM images of SNPs made using process 1 are shown in figures 6.1(a), 6.1(d) and 6.1(e). The number of SNPs on the substrate in an area of 100×100 μm^2 was 1 or 2. From the AFM images, it can be seen that the solutions contain some silver particles in addition to the SNPs, which are side products obtained in small amount. It was also observed that the SNPs obtained with different processes were of uniform thickness. Height profile of an SNP along the line shown in figure 6.1(a) is presented in figure 6.1(b). We have also conducted X-ray diffraction and transmission electron microscope (TEM) studies, which confirmed the single crystallinity of our SNPs, summarized in figures 6.1(c), 6.1(f) and 6.1(g). In table 6.1, we present the average thickness and the average maximum lengths of the SNPs obtained using different synthesization processes. The root mean square (RMS) roughness in table 6.1, represents the variation in the thickness over an area of 1 μm^2. To obtain the average RMS roughness of SNPs independent on the substrate, we first made measurements of the roughness of the substrate and subsequently subtracted this value from the value obtained by measuring directly onto the SNPs. This then gave us a good estimate of the roughness stemming directly from the SNPs. From table 6.1, it is clear that SNPs obtained in process 1 are thinner, have larger transverse dimensions and are smoother than SNPs obtained with the other processes. Therefore, SNPs obtained in process 1 are more suitable for fabrication of miniaturized plasmonic circuits.

6.3 Fabrication of Designed Structures using Focussed Ion Beam Lithography

The desired structures were fabricated by cutting the SNPs by means of FIB milling (Helios Nanolab from FEI). We made silver wires and tips, which have been found to be effective for coupling quantum emitters to propagating plasmonic modes [27]. The

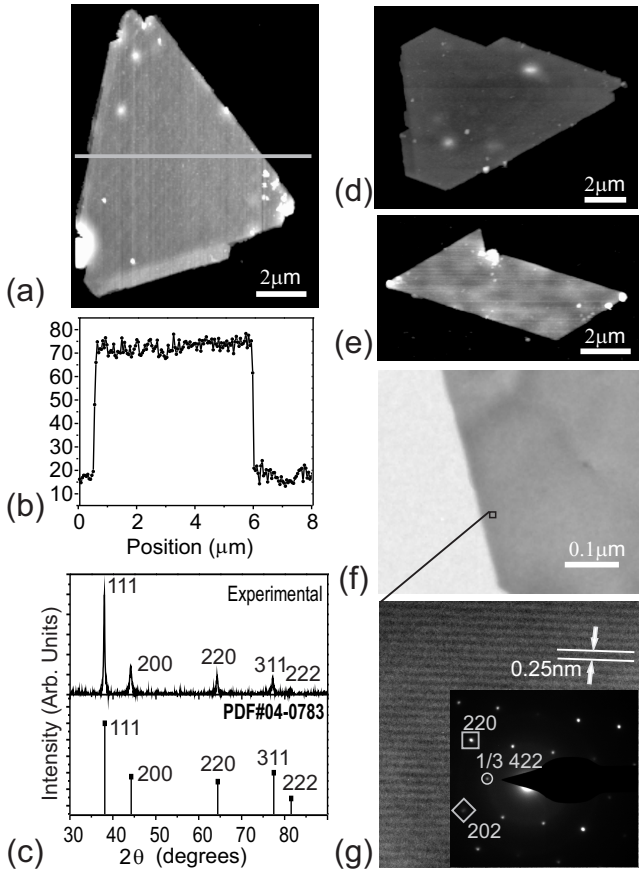

Figure 6.1: **Structural characterization of SNPs (a),(d)** and **(e)** AFM images of SNPs obtained with process 1. **(b)** Height profile of the SNP shown in (a) along the horizontal line indicated in (a). **(c)** X-ray diffraction pattern for the SNPs along with standard pattern for silver (PDF#04 − 0783), showing dominance of the (111) crystalline plane for SNPs. **(f)** TEM image showing the edge of an SNP. **(g)** High resolution TEM image of the SNP from which the lattice spacing is clearly visible. The inset shows a selected area electron diffraction pattern, which proves the single crystallinity of our SNPs.

Table 6.1: Properties of SNPs obtained using different chemical processes.

Process	Average thickness, SNP (nm)	Average maximum lengths, SNP (μm)	Average RMS roughness, Substrate (nm)	Average RMS roughness, SNP on substrate (nm)	Average RMS roughness, SNP (nm)
1	63.6	10.75	3.87	4.78	0.91
2	97.2	8.51	4.01	6.76	2.75
3	151.7	8.59	4.43	7.12	2.69
4	259.0	3.13	4.14	5.99	1.85

substrate used for FIB milling of SNPs was a fused silica glass plate coated with a 50 nm layer of conducting Indium Tin Oxide (ITO), which is required for FIB milling. We plasma cleaned our substrates for 5 minutes. Then, the solution containing SNPs was spin coated onto the substrates. To obtain nanostructures in the FIB milling process, we chose an acceleration voltage of 30 kV and a Ga-ion current of 1.5 pA. Figure 6.2(a) shows a scanning electron microscope (SEM) image of some wires and tip structures made with FIB milling of a large SNP, whereas figures 6.2(b) and 6.2(c) show zoom-in high resolution SEM images. The apex angle of the tip shown is 10 °, and width of the wire shown is 50 nm. Structures obtained with this method are smooth (roughness of the order of the SNP roughness) and single crystalline.

6.4 Optical Characterization of Structures made with FIB Milling

When SNPs are FIB milled with Ga ions, very small clusters of silver gets redeposited on silver structures [86]. The silver clusters have sizes less than the resolution of SEM images taken ($\approx$ 2 nm), and can be as small as a cluster of few atoms. These small clusters of silver give rise to fluorescence [87] when illuminated by light. Another source of fluorescence could be some Ga ions deposited during the FIB process. This is however less likely as the concentration of Ga ions deposited is very low [80].
To optically characterize the structures, we used the optical set-up described in Chapter 2. A fluorescence image of an SNP (before FIB milling) is shown in figure 6.3(a), where it can be observed that the fluorescence from SNP is negligible. By comparing

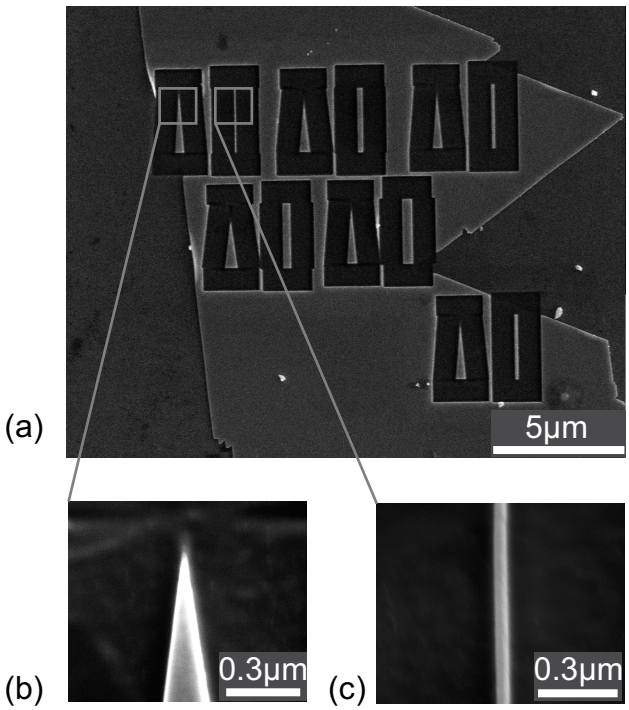

Figure 6.2: **SEM images of structures made with FIB milling of an SNP. (a)** Some tips and nanowires of different tip angles and wire widths made using FIB milling of an SNP. **(b)** Magnified image of tip shown in left rectangle in (a). **(c)** Magnified image of wire shown in right rectangle in (a).

the fluorescence image in figure 6.3(a) to SEM image of the SNP in figure 6.1(e), we conclude that the fluorescence stems from particles lying close to the SNP. A fluorescence image of the wire, whose SEM image is shown in figure 6.3(b), is shown in figure 6.3(c). The wire has a length of 3 μm, a width of 100 nm and a height of approximately 100 nm. It is clearly seen that, there is pronounced fluorescence which presumably stems from the clusters of silver particles.

We now demonstrate plasmon propagation along one of the nanowires by local optical excitation on one end of the wire and collection of fluorescence photons at the opposite end. This is done by focussing the excitation beam (532 nm) with a microscope objective onto the end while scanning the image plane containing the wire with a galvanometric mirror. The focussed laser beam creates fluorescence, a fraction of which is coupled to the plasmonic mode which then propagates to the distal end of the wires. Due to a symmetry break at the end, a fraction of the plasmonic mode is coupled to the far field which is then collected by the microscope. Figures 6.3(d) and 6.3(e) show such fluorescence images when the laser was focussed on spots 'A' and 'B', of figure 6.3(c), respectively, and it is clearly seen that plasmons are supported by the wires as they lit up at the end opposite to the excitation end (corresponding to spots 'B' and 'A' in figures 6.3(d) and 6.3(e), respectively). We also note that part of the 532 nm light can also get coupled to the plasmonic mode and, in principle, propagate to the distal end where silver nanoclusters can be excited and subsequently fluoresce [88]. However, since the estimated loss for 532nm light for reaching the distal end is around 95dB, we conclude that this process is unlikely to take place in practice.

At the distal end of the nanowire some of the fluorescence light is reflected back into the plasmonic mode, and thus the nanowire works as a cavity. This can be proven by measuring the spectrum of the fluorescence, which in case of a cavity effect should exhibit oscillations with a period equal to the free-spectral-range of the cavity. Spectra of the wire in figure 6.3(c) taken at both spots 'A' and 'B' are presented in figure 6.3(f). The spectrum of spot 'A' in figure 6.3(f) originates mainly from the fluorescence light that is not coupled into the wire and thus it does not show oscillations but purely the spectrum of the fluorescence. However, the spectrum obtained from spot 'B' (the fluoresence, which purely comes from the propagating plasmon) exhibits strongly damped oscillations thereby proving the presence of a very low-finesse cavity [89].

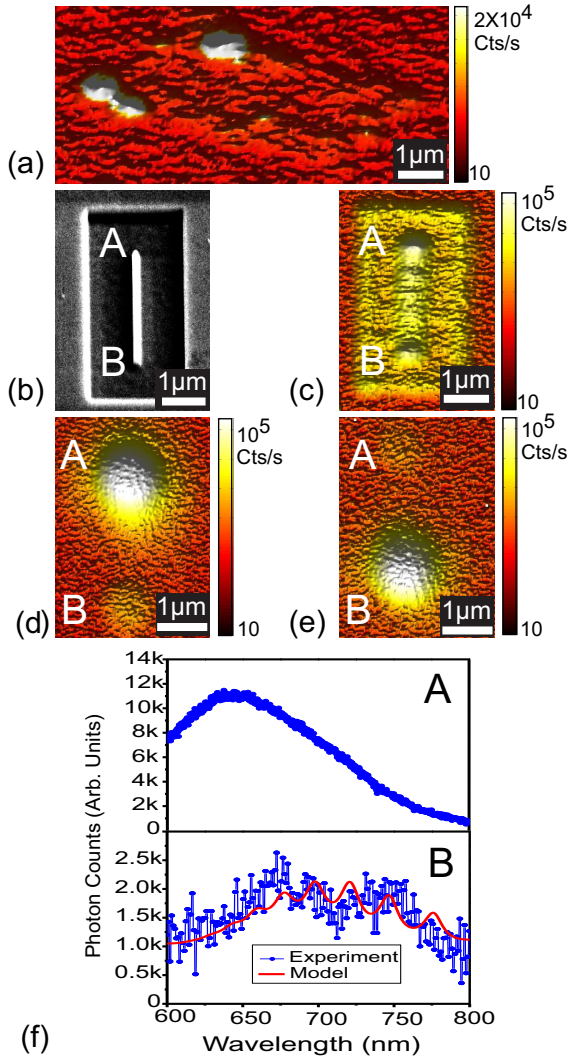

Figure 6.3: **Optical Characterization.** **(a)** Fluorescence image of the SNP shown in figure 1(e). Color scale for all the fluorescence images is exponential. **(b)** SEM image of a wire made by FIB milling of an SNP. **(c)** Confocal microscope fluorescence image of the area shown in (b). **(d)** and **(e)** Galvanometric fluorescence images taken when the laser is focussed onto ends 'A' and 'B' of the wire shown in (c), respectively. **(f)** Spectrum taken at end 'A' and end 'B' of the wire in (d). A model based on the spectrum of end 'A' as input and silver wire as a Fabry-Perot cavity is also plotted.

6.5 Simulations

We calculate the fundamental plasmonic mode of a silver wire using COMSOL, as has been described in Chapter 2. The Pointing vector (P_z) for the fundamental plasmonic mode of a wire (with a 100 × 100 nm^2 cross-section) is shown in figure 6.4(a). One clearly sees that the mode is strongly confined at the edges of the wire near the interface to the ITO layer. We also obtained different effective refractive indices for a range of wavelengths as electric permittivity of silver and ITO varies between 600 nm and 800 nm [64, 90]. From the simulations we find the plasmon propagation losses (α_{pl}) as well as the plasmonic wavelength (λ_{pl}). The results are presented in figure 6.4(b) as a function of the vacuum wavelength and the data points were fitted to a polynomial of fourth order. The large propagation losses are a result of the strong localization at the ITO-silver interface.

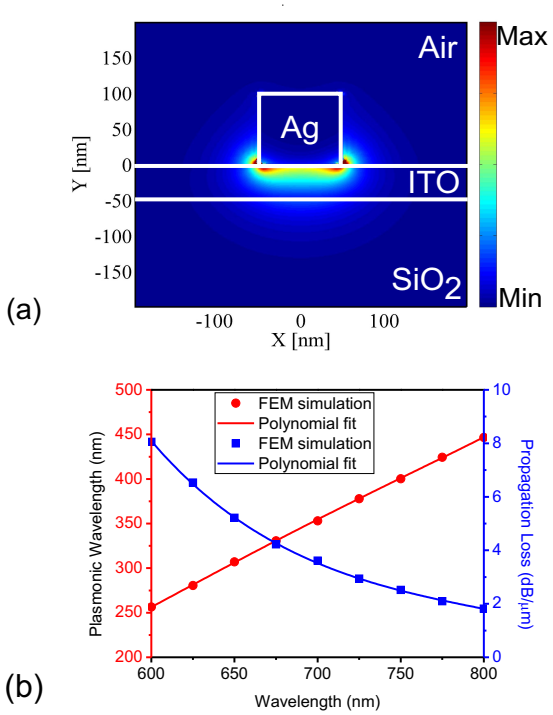

Figure 6.4: **FEM simulations.** **(a)** The z-component of pointing vectors for the fundamental plasmonic mode is plotted for a silver wire of cross-section 100nm by 100nm situated on ITO coated fused silica substrate. **(b)** Plasmon wavelength and propagation losses as a function of wavelength.

Using the results from the FEM simulation and the fluorescence spectrum from wire

end 'A' in figure 6.3(f), the expected spectrum for the oscillating plasmonic field is also shown in figure 6.3(f) by the solid curve. It shows modulation features similar to that of the spectrum obtained experimentally. In the calculations we have not taken into account the fact that the coupling of fluorescence light into the wire as well as the reflections of the plasmons at the wire ends depend on the wavelength [91]. Moreover, the cross-section of the fabricated nanowire may not match exactly to the cross-section of the simulated wire. These facts might explain the discrepancy between the experimentally obtained spectrum and the simulated one. However, the relatively close match between theoretical and experimental spectrum suggests that the wires fabricated are of high quality.

6.6 Conclusion

We have made single crystalline and very smooth silver plates with a thickness around 65 nm and lengths and widths in order of 10 μm using a wet chemical synthesis. These plates were then used for the fabrication of nanowires and nanotips with very high precision using FIB milling. The structures were optically addressed, and it was found that the wires support propagating plasmons and that they act as low-finesse cavities. The optical characterization also revealed the presence of large fluorescence, which probably stems from redeposition of small silver particles during the FIB milling process. This fluorescence is a deterrant for the observation of single photons emitted from an NV-center. We therefore did not couple NV-centers to the structures fabricated using the method described in this chapter.

Chapter 7

Fabrication of Silver Nanowires with the Tip of an AFM Cantilever

In chapter 6, it was shown that silver nanoplates (SNPs) can be structured using focussed ion beam milling. However, the fluorescence from the structures obtained with such a method is high even though fluorescence from the SNPs is negligible. In this chapter, we describe a novel method for the fabrication of single crystalline silver nanowires. We use the tip of an AFM cantilever to carve out the desired silver nanowires from SNPs. In contrast to focussed ion beam milling, this method does not depend on the kind of substrate used. We also present the characterization of these nanowires as well as the coupling of an NV-center to such a nanowire.

7.1 Fabrication of Nanowires by Etching of SNPs with the AFM Cantilever

If a sharp and hard material is pressed onto a softer material, the harder material penetrates into the softer material. If a sharp and hard material is pressed and moved on top of a softer material, the harder material cuts the softer one. Also, depending on the force applied for pressing the harder material onto the softer material, multiple movements might be needed to cut the softer material. This principle of cutting has been known for centuries [92]. We apply this principle to make silver nanowires by etching away parts of the single crystalline SNPs. Using a similar technique, single crystalline wires have been fabricated from gold nanoplates, where diamond ultramicrotome is used to cut the gold nanoplates embedded in epoxy [93].

SNPs used for this fabrication were synthesized using the chemical process described in chapter 6. We spin coat solution containing SNPs on a fused silica substrate. Then AFM and fluorescence images are taken for an SNP. We make nanowires in a region of SNP where fluorescence is negligible. To carve out silver nanowires from SNPs, we either use diamond coated silicon cantilevers or bare silicon cantilevers. Diamond is known to have the highest hardness of 10 on Mohs' scale of 0-10, which is an ordinal scale [94]. Silicon has a hardness of 7, and silver in the range of 2.4-4 in comparison. To make the nanowires, we press the substrate with the AFM cantilever with a contact force of ≈ 1 μN, and scan the area of SNP that we want to etch away in contact mode operation of the AFM. This cuts the silver nanoplates and also takes away most of the silver particles that are produced in the process. Some additional cleaning with the AFM cantilever is needed in order to take away all the silver particles, which is done by scanning the area in contact mode of the AFM once again, but with nearly 10 times lower contact force.

Figure 7.1 shows AFM images of 5 different nanowires made with this process. They all have different dimensions as can be observed from the images. The height and the maximum length of the nanowire is limited by the dimensions of the SNPs. The width of the nanowire is mainly limited by the contact force between the silver nanowire, that is being made, and the substrate. By using a substrate whose adhesive force with silver is higher, thinner wires can be fabricated. In some cases, for example figure 7.1(a), some particles produced in this process of fabrication remain with the silver nanowires.

7.2 Propagation of Plasmons

The SNPs used for fabrication of silver nanowires are single crystalline as described in the previous chapter. Etching of SNPs with the AFM cantilever does not change their crystallinity. This should lead to lower propagation losses when compared to polycrystalline silver nanowires. However, etching with the AFM cantilever produces some roughness on the surface of the nanowires. This should lead to higher propagation losses when compared to single crystalline silver nanowires produced using the chemical method.

We have tested the silver wires, made with the process described above, to know whether they support propagating plasmon modes. Silver particles are known to fluoresce when excited with a laser in visible spectral region [87]. This can be seen from

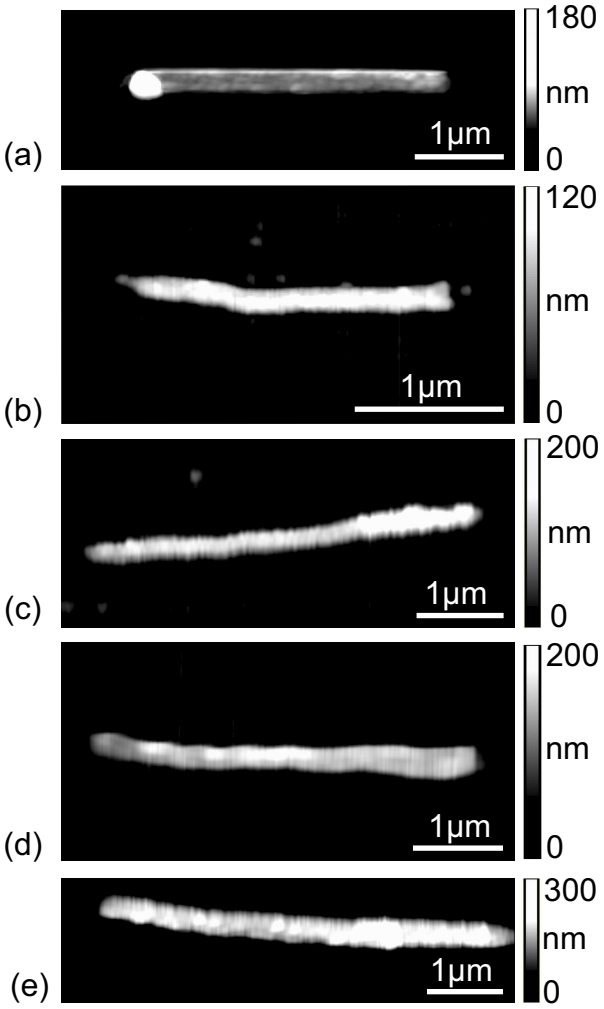

Figure 7.1: **AFM fabricated wires. (a)-(e)** AFM images of 5 different wires fabricated by etching of SNPs with an AFM cantilever.

the fluorescence image in figure 7.2(a), for the wire with the AFM image shown in figure 7.1(a). We used fluorescence from the silver particles to excite the propagating plasmonic modes into the nanowires. Figure 7.2(b) shows a galvanometric scan image taken by continuously exciting end 'A' of the wire with the fluorescence image shown in figure 7.2(a). In the scan, fluorescence from the distal end of the nanowire could be observed. This means that the fluorescence from spot 'A' in figure 7.2(b) got coupled to propagating modes of the nanowire, propagated to the distal end, and some of the plasmon polaritons got scattered into the far field. This appears as spot 'B' in figure 7.2(b). Similarly, a galvanometric scan image of fluorescence was taken while continuously exciting end 'B' of the wire in figure 7.2(a), and some fluorescence from end 'A' was observed. This verifies the propagation of plasmon polaritons in silver nanowires fabricated with AFM.

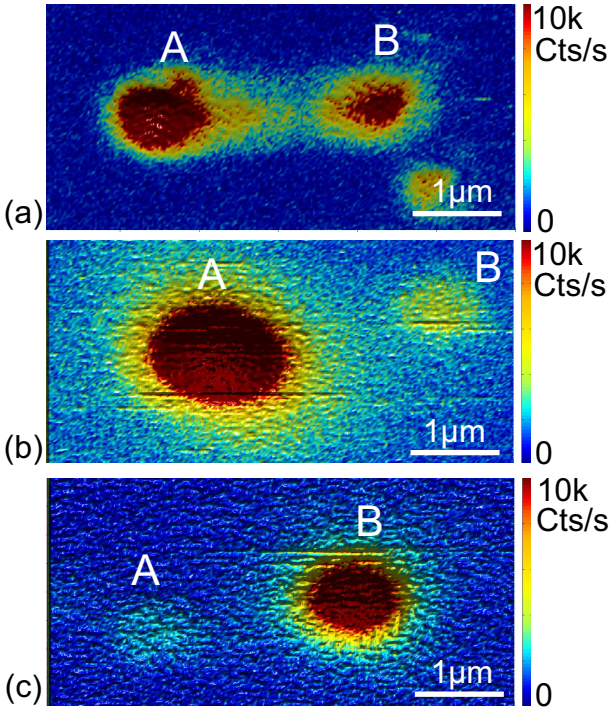

Figure 7.2: **Propagation in wires made with an AFM. (a)** Fluorescence image of the silver nanowire whose AFM image is shown in figure 7.1(a). **(b)** Galvanometric image when spot A in (a) is excited. **(c)** Galvanometric image when spot B in (a) is excited.

7.3 Coupling an NV-center to the AFM Fabricated Nanowires

We have shown that silver nanowires can be fabricated by etching of SNPs with an AFM cantilever, and these nanowires support propagating plasmon modes. In this section, we use such a nanowire for coupling an NV-center in a nanodiamond to its plasmonic modes.

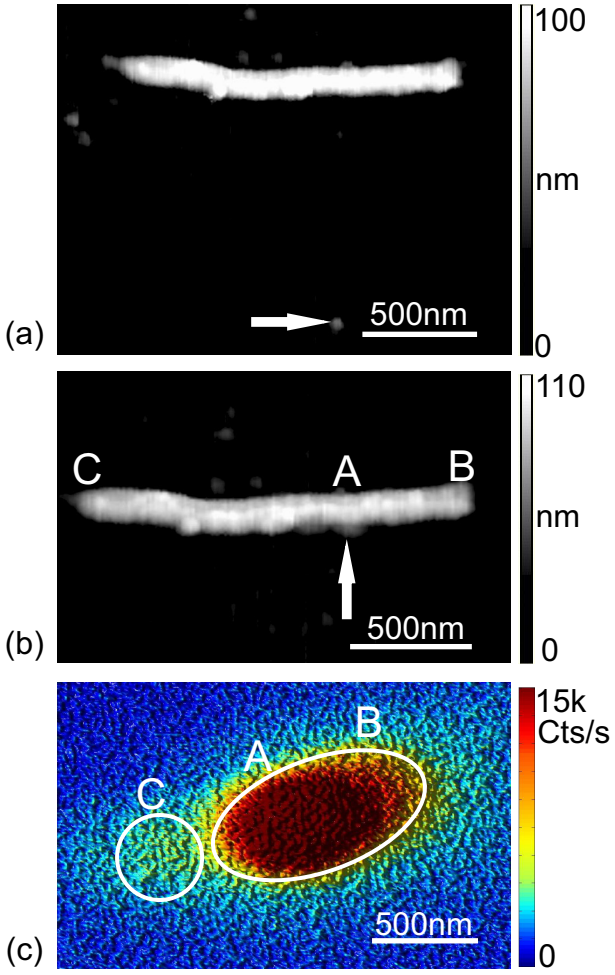

Figure 7.3: **Coupling of an NV-center's emission to a silver nanowire made with AFM. (a)** and **(b)** AFM images of a silver nanowire and a nanodiamond containing an NV-center. The position of the nanodiamond is indicated with arrows. **(c)** Galvanometric image when NV-center in (b) is excited.

To do this experiment, solutions containing nanodiamond and that containing SNPs

were spin coated on a fused silica substrate. A silver nanowire was then fabricated, and then a nanodiamond containing a single NV-center was identified using a process that has been described in chapter 3. Lifetime, spectrum and autocorrelation measurements were also taken confirming that the nanodiamond contained a single NV-center. An AFM image of the wire along with a nanodiamond containing a single NV-center is shown in figure 7.3(a).

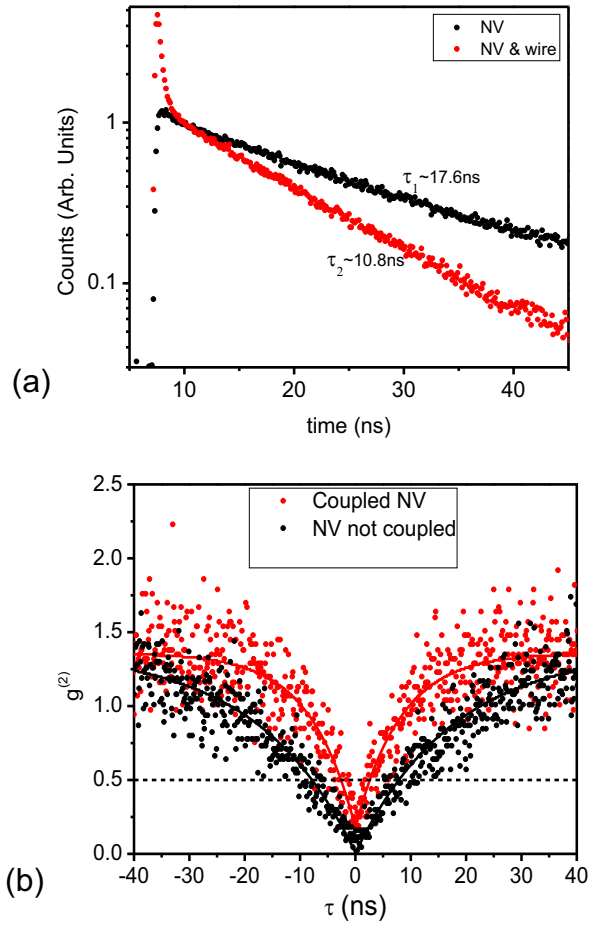

Figure 7.4: **(a)** Lifetime measurement data for the NV-center in figure 7.3 before and after coupling to a silver nanowire. **(b)** Autocorrelation measurement data for the NV-center before and after coupling to the silver nanowire. Fitted curve according to a three level model is also shown.

After locating the nanodiamond with an NV-center, we move the nanodiamond across the sample so that the nanodiamond is placed within a few nanometers from the surface of the nanowire. An AFM image of the coupled system is shown in figure 7.3(b). Figure 7.3(c) shows a galvanometric image of the coupled system, when the NV-center

(spot 'A') is excited continuously with 532 nm CW laser. The emission spot is elongated, and it also shows some fluorescence from end 'C' in figure 7.3(c). End 'C' is 1.1 μm away from the nanodiamond and end 'B' is $0.7\mu m$ far from the nanodiamond. This results in an overlap of spots 'A' and 'B'. Also, spot 'C' is not clearly isolated from spot 'A'. The emission from spot 'C' is small, which is mainly due to small coupling between the NV-center and the nanowire as discussed below.

Figure 7.4(a) shows lifetimes of the NV center in the nanodiamond when it was far from the nanowire as shown in figure 7.3(a), and when the nanodiamond was close to the wire as shown in figure 7.3(b). From a comparison in the lifetimes, a rate enhancement of 1.63 is observed in this case. In the lifetime measurement data of the NV-center after coupling to the nanowire, we can also observe very fast decay, which comes from fluorescence of the particles created alongwith the nanowire. We also measured correlation before and after coupling of the NV-center to the nanowire. One can observe from figure 7.4(b) that $g^2(0) < 0.5$ for the NV-center, when it is coupled to the nanowire as well as before it was coupled. However, $g^2(0)$ increased from 0.01 to 0.18, mainly due to fluorescence from the nanowire. The autocorrelation shows that the fluorescence from the wire itself is not too high to suppress the single photon emission characteristics completely.

7.4 Conclusion

We have fabricated single crystalline silver nanowires by carving it from SNPs using an AFM cantilever. We have shown that the nanowires fabricated using such a method support propagating plasmonic modes. We have also shown coupling between such a nanowire and an NV-center in a nanodiamond.

This process of making silver nanowires can be optimized further to make very thin wires. This can be done by increasing the adhesion between the SNP and the substrate. Use of thinner SNPs in fabrication of these wires can also allow for the fabrication of thinner wires. The process described in this chapter can also be used for making different structures, other than nanowires, by obtaining control over the tip movement.

Chapter 8

Channeling Photons from a Silver Nanowire to Another Waveguide

Plasmonic waveguides are very efficient in channeling and enhancing the emission of a single photon emitter. However, they cannot be used for long distance communication, because of the high propagation losses. It is therefore important to couple the light from the plasmonic waveguides to dielectric waveguides, in which light may propagate for long distances without much loss [28]. Efficient coupling between a plasmonic waveguide and a dielectric waveguide can also lead to hybrid integrated optical devices, such as a compact polarizer [95] and a refractive index sensor [96]. In this chapter, we present some theoretical results obtained for the evanescent coupling between dielectric waveguides and silver nanowires. We use silicon nitride as the waveguide material, because of its higher refractive index($\approx$2.0) and low propagation losses in the visible spectral region [97, 98].

In previous chapters, we have described the coupling of NV-centers in nanodiamonds to plasmonic structures made using different techniques. It is also important for quantum optics applications to make an integrated plasmonic circuit. We here describe some theoretical and experimental studies conducted for evanescent coupling of two chemically grown silver nanowires. Such coupling has been demonstrated [99]. We here couple a single NV-center in a nanodiamond to a silver nanowire, which is then evanescently coupled to another silver nanowire.

8.1 Evanescent Coupling between a Silver Nanowire and a Dielectric Waveguide

We want to evanescently couple the propagating plasmonic mode of a silver nanowire to a dielectric waveguide mode. Figure 8.1 shows a schematic of the coupling system that we have studied. The silver nanowire is assumed to have a circular cross-section, with a diameter D. The silicon nitride waveguide has a rectangular cross-section of height H and width W. The 'Gap' denotes the separation between the two waveguides.

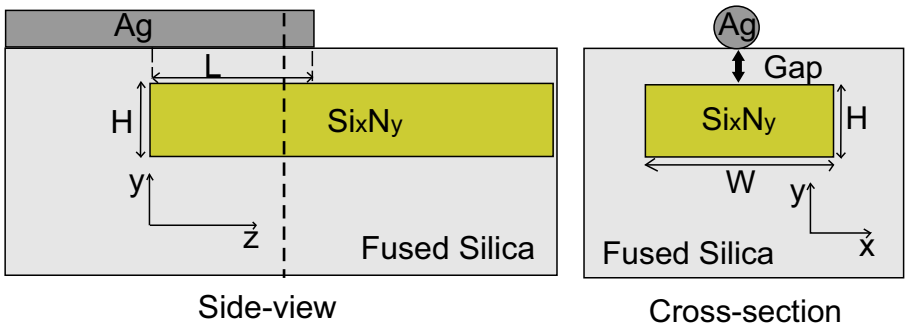

Figure 8.1: **Schmematics of Coupled structure.** Side view schematics of coupled structure is shown. Cross-section of the coupling region along the dashed line of the coupling structure is also presented. H: Height, W: Width, L: Length of coupling region.

The z-component of the normalized pointing vector of a plasmonic mode for a silver nanowire lying on top of a fused silica substrate is presented in figure 8.2(a), whereas the z-component of the normalized pointing vector for the transverse magnetic (TM) mode for a silicon nitride waveguide is shown in figure 8.2(b).

When two waveguides are brought close to each other, they form coupled modes, which we will refer to as even (E) and odd (O) modes. Even and odd modes have different effective indices, due to their different distribution of fields in the cross-section of the coupled system, and hence propagates with different velocities. The beating of the two coupled modes allows for coupling of power from one waveguide to another. For efficient coupling between metallic and dielectric waveguides, the velocities of propagation in dielectric and metallic waveguides should be matched [100, 101, 102]. According to standard coupled mode theory, the maximum fraction of power that can be transferred

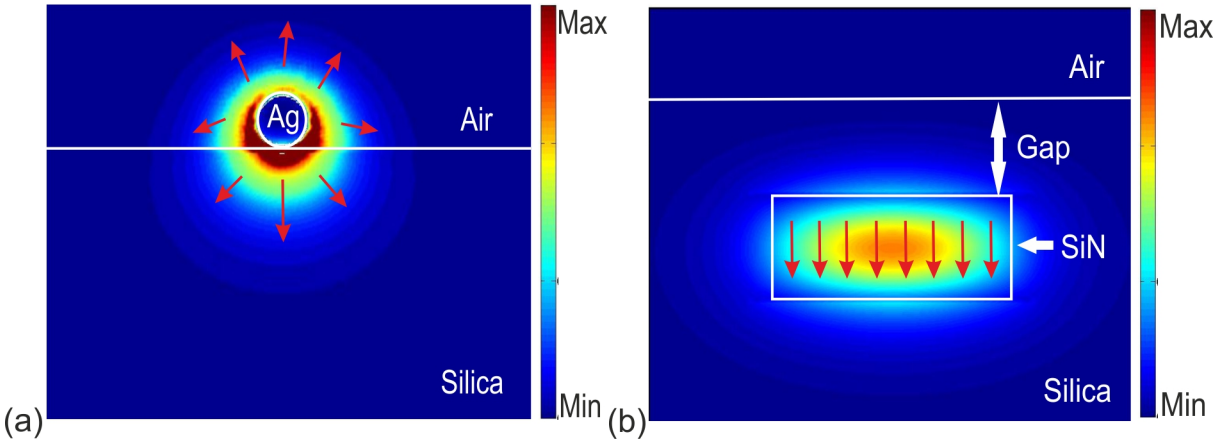

Figure 8.2: **Waveguide modes.** Plot of z-component of normalized pointing vector for **(a)** the plasmonic mode of a silver nanowire of diameter $71nm$ lying on top of a fused silica substrate, and **(b)** the TM mode of silicon nitride waveguide with a cross-section of 400×230 nm^2, $200nm$ deep in the fused silica substrate. The arrows represent the direction of the electric field.

from one waveguide to another is given by [102]:

$$F = \frac{1}{1 + (Re\{n_{Ag} - n_{SiN}\}/Re\{n_E - n_O\})^2} \tag{8.1}$$

where, n_{Ag} and n_{SiN} are effective mode indices for the metallic and dielectric waveguides, respectively. n_E and n_O are mode indices of even and odd modes, respectively, of the coupled waveguide system.

8.1.1 Mode Indices of Individual Waveguides

In COMSOL, we calculated the effective mode indices for the silver nanowires by varying its diameter, and the mode indices of the silicon nitride waveguides by varying its cross-section. The plot of effective mode index, for the plasmonic mode in silver nanowire, as a function of the nanowire diameter is presented in figure 8.3. Figure 8.4 shows the variation of the mode indices of the transverse electric (TE) and transverse magnetic (TM) modes of the silicon nitride waveguide, when the cross-section of the waveguide is changed. These mode indices are calculated for the silicon nitride waveguides buried deep into the fused silica substrate. Horizontal dashed lines represent the effective indices of the fundamental plasmonic mode of the silver nanowire of diameters

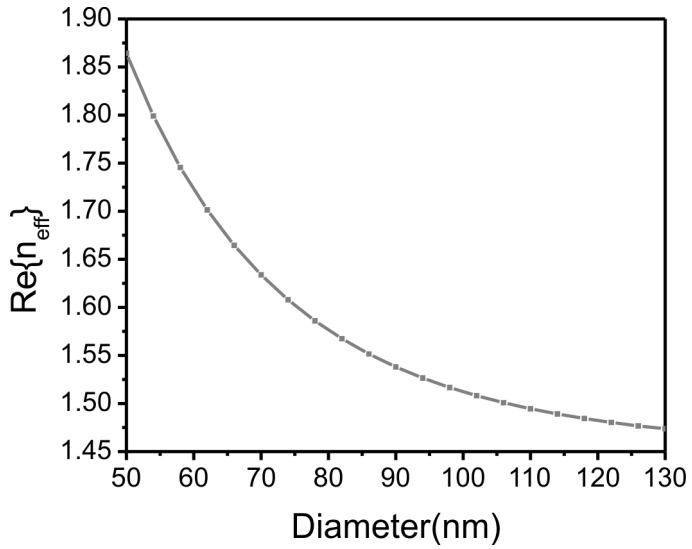

Figure 8.3: **Silver nanowire mode indices.** The real part of the effective mode index as a function of the diameter of the silver nanowire.

indicated on the lines. The dashed lines and the curve representing the variation of mode indices of the silicon nitride waveguide cross at a point where the effective mode indices match for the two waveguides and they can be coupled efficiently, in principle. We also noted that the mode indices of silicon nitride would change depending on the depth of the waveguide inside the fused silica substrate. We therefore calculated the mode indices as a function of the depth from the surface of the fused silica substrate for a chosen silicon nitride cross-section, which is 400×230 nm^2. The variation of the mode index, as the 'Gap' between the surface of the substrate and the surface of the waveguide is varied, is shown in figure 8.5 along with the mode indices of silver nanowire for the diameter range 70-80 nm. We observe from figures 8.5(a) and 8.5(b) that the mode indices can be matched closely for the two kinds of waveguides for appropriately chosen cross-section of the waveguides for a given 'Gap'. In the calculations below, we keep the cross-section of the silicon nitride waveguide constant (i.e. 400×230 nm^2) and we change the depth. To keep the mode indices of the two waveguides close, we need to correspondingly change the diameter of the silver wire.

8.1.2 Numerical Simulation of Coupling

When the electromagnetic field is launched from the silver nanowire at $z = 0$, the $\mathbf{H}_{Ag}$ field in the silver nanowire can be expressed as a superposition of the even and odd

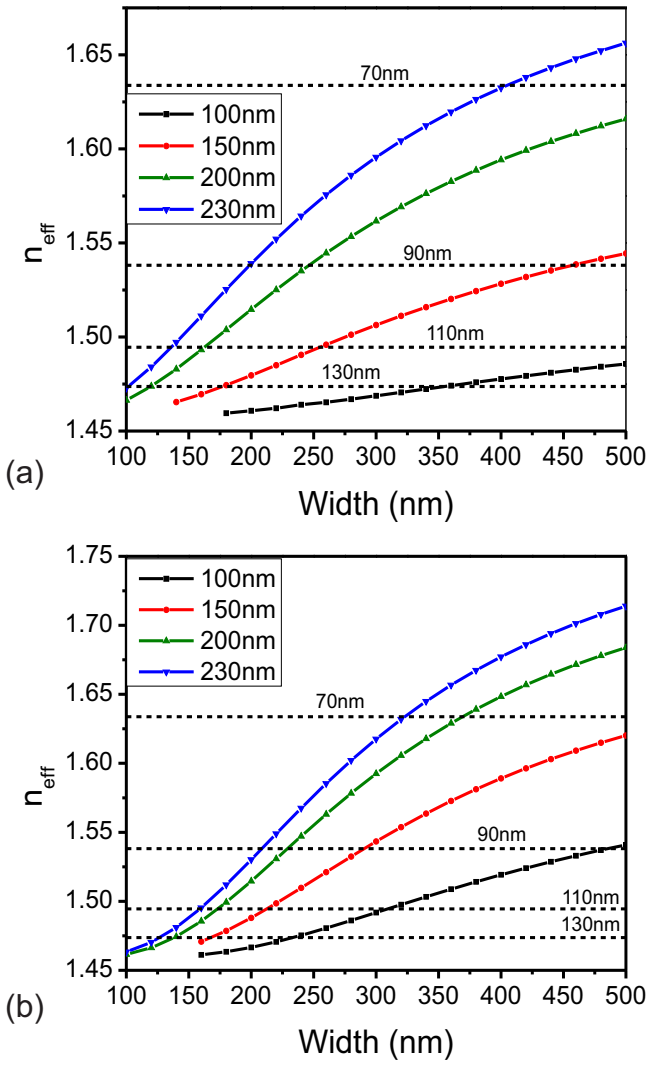

Figure 8.4: **Silicon nitride waveguide mode indices.** Plots of effective mode indices of the TE **(a)** and TM **(b)** modes of the silicon nitride waveguide buried deep in fused silica substrate as the width of the waveguide is changed for different heights of the waveguide. Horizontal dashed lines represent the real part of effective indices for silver nanowires of the diameter indicated on the horizontal line.

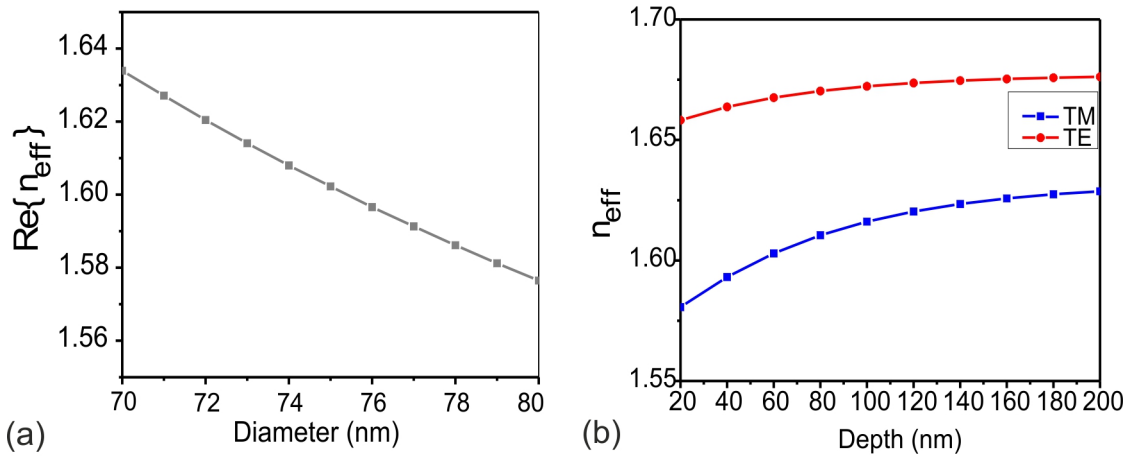

Figure 8.5: (a) Real part of the mode indices in the range of silver nanowire diameters between 70 nm and 80 nm. (b) Mode indices as a function of distance from the surface of the fused silica substrate for a silicon nitride waveguide of cross-section 400×230 nm^2.

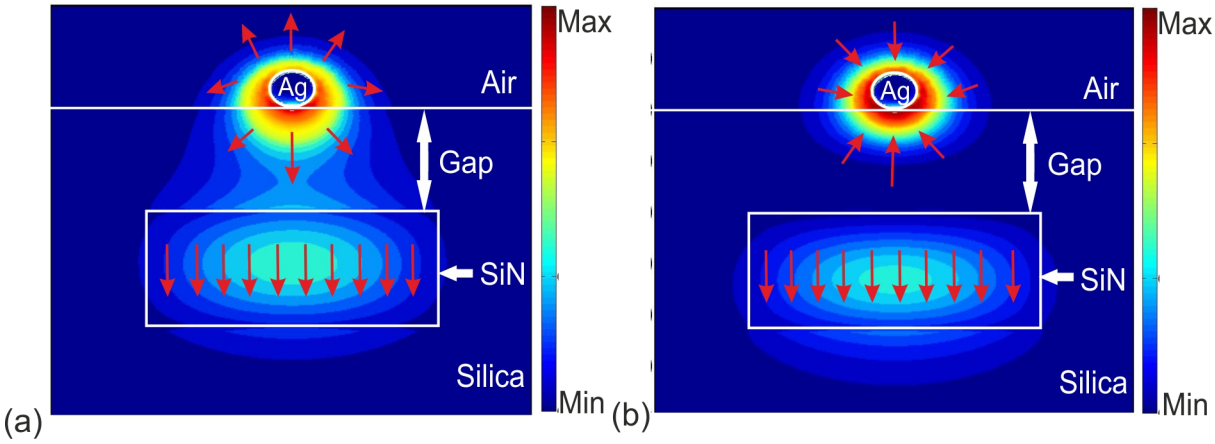

Figure 8.6: **Coupled modes.** Plot of pointing vector of the even **(a)** and odd **(b)** modes for silver wire of diameter 71 nm lying on top of fused silica substrate and silicon nitride waveguide of cross-section 400×230 nm^2 lying 200 nm deep in the fused silica substrate.

modes with an additional term representing the radiation field [103].

$$\mathbf{H}_{Ag}(x,y,0) = a_E \mathbf{H}_E(x,y) + a_O \mathbf{H}_O(x,y) + \mathbf{H}_r(x,y,0) \tag{8.2}$$

where, $\mathbf{H}_E$, $\mathbf{H}_O$ are complex magnetic fields of even and odd eigen modes supported by the coupled system, and $\mathbf{H}_r$ is the magnetic field of the radiation modes. a_E and a_O are coupling constants from the silver nanowire to even and odd modes, respectively, and are given by,

$$a_E = \frac{1}{2}\int_{A_\infty} [\mathbf{E}_{Ag} \times \mathbf{H}_E] \cdot \hat{z} dA \tag{8.3}$$

$$a_O = \frac{1}{2}\int_{A_\infty} [\mathbf{E}_{Ag} \times \mathbf{H}_O] \cdot \hat{z} dA \tag{8.4}$$

$\mathbf{E}_{Ag}$ is the electric field of the plasmonic mode in the silver nanowire. A_∞ denotes integration over xy-plane. It is important to note that all the mode fields are normalized. The normalization of the mode fields is done as follows:

$$N_m = \frac{1}{2}\left|\int_{A_\infty} \left[\mathbf{E'}_m \times \mathbf{H'}^*_m\right] \cdot \hat{z} dA\right| \tag{8.5}$$

where, $m \equiv E, O, Ag, SiN$, and $\mathbf{E}'$ and $\mathbf{H}'$ are mode fields before normalization. Then, the normalized fields are given by:

$$\mathbf{E}_m = \frac{\mathbf{E'}_m}{\sqrt{N_m}} \tag{8.6}$$

$$\mathbf{H}_m = \frac{\mathbf{H'}_m}{\sqrt{N_m}} \tag{8.7}$$

The different eigen modes are orthogonal modes. So, the modes used for calculating coupling constants are orthonormalized. At z, the mode field inside the coupled region can be written as:

$$\mathbf{H}(x,y,z) = a_E \mathbf{H}_E(x,y)\, e^{i\beta_E z} + a_O \mathbf{H}_O(x,y)\, e^{i\beta_O z} \tag{8.8}$$

where β_E and β_O are complex propagation coefficients for even and odd modes, respectively. It is the difference between the real parts of these propagation coefficients that leads to beating between even and odd modes and enables power transfer from one waveguide to another. The coupling length, defined as half of the beat length, is given as:

$$L_c = \frac{\pi}{Re\left(\beta_E - \beta_E\right)} \tag{8.9}$$

At the output end $z = L$, the coupling coefficient between the coupled mode and the TM mode of the silicon nitride waveguide is given by:

$$a_{SiN} = \frac{1}{2}\int_{A_\infty} \left[\mathbf{E}_{SiN} \times \mathbf{H}\left(x, y, L\right)\right] \cdot \hat{z} dA \tag{8.10}$$

and the total coupling loss is subsequently obtained as,

$$\text{Loss}_{\text{coupling}} = -20log_{10}|a_{SiN}|. \tag{8.11}$$

All the modes and complex propagation coefficients are calculated in COMSOL. Figure 8.6 shows the two coupled modes, even and odd, when a silver nanowire of a diameter 71nm and silicon nitride waveguide with a cross-section of 400×230 nm^2 are kept so that a 'Gap' of 200 nm remains.

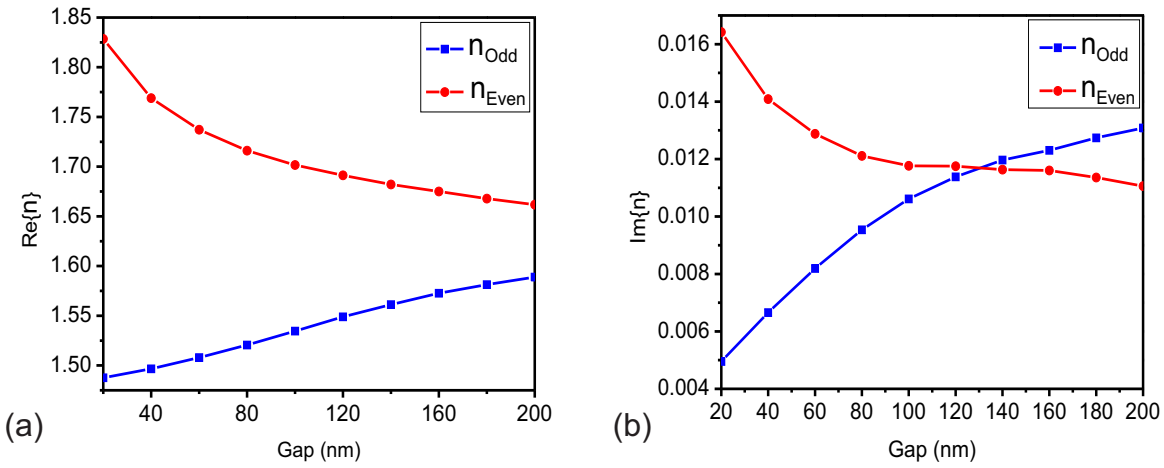

Figure 8.7: **Coupled mode indices.** Plot of real **(a)** and imaginary **(b)** mode indices as the 'Gap' between the 230×400 nm^2 cross-section silicon nitride waveguide and the silver nanowire of corresponding diameter is changed.

Real and imaginary parts of the effective mode indices are presented in figure 8.7. From the real part of the mode indices shown in figure 8.7(a), the coupling lengths can be calculated according to equation 8.9. Since the difference in magnitude of the mode splitting depends on the 'Gap' between the two waveguides, the coupling lengths, L_c, also depend on the 'Gap'. This dependence is plotted in figure 8.8(a).

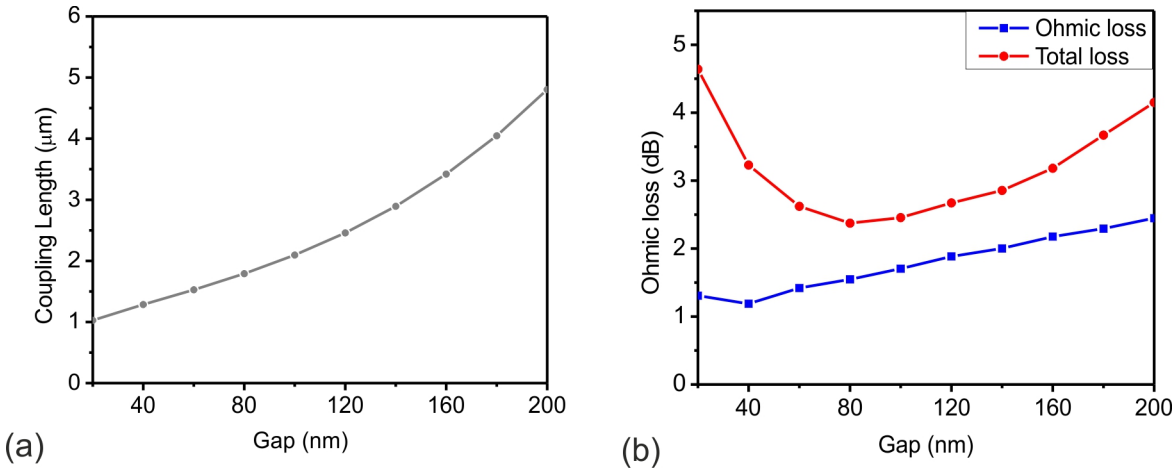

Figure 8.8: **Coupling length and losses. (a)** Coupling length as a function of 'Gap' between the two waveguides. **(b)** Coupling losses as a function of 'Gap' between the waveguides.

The propagation losses of coupled modes over the coupling length L_c, we will refer to as 'Ohmic loss'. Ohmic losses are calculated using the coupling coefficients and mode indices of the even and odd modes of the coupled system. The total coupling loss associated with the coupling from the silver nanowire to the dielectric waveguide over a length L_c is calculated using euations 8.11 and 8.10. Figure 8.8(b) presents the total coupling losses as well as Ohmic losses over L_c as a function of 'Gap'. The dependence of coupling losses on the 'Gap' is explained by the dependence of L_c on it - the more the 'Gap', the higher the L_c. The longer the propagation length needed for coupling, the more the Ohmic losses. However, if the 'Gap' is made very small, the scattering into the free space increases due to increased mismatch between the superposition of coupled modes and the individual waveguide modes. This leads to an optimum 'Gap' between the waveguides for efficient coupling. For the waveguide cross-sections discussed, a 'Gap' of around 100 nm would minimize the total coupling losses.

For the 'Gap' of 100 nm and the chosen silicon nitride waveguide cross-section of 400×230 nm^2, the required silver nanowire diameter, to match the real part of the effective mode indices for the two waveguides, is 73 nm. In figure 8.9, the total loss and ohmic loss are presented, for the 'Gap' of 100 nm, as a function of length of the coupled waveguide system. One can observe that the coupling efficiency is maximum for a length, which is slightly less than L_c. This happens due to the complex coefficients

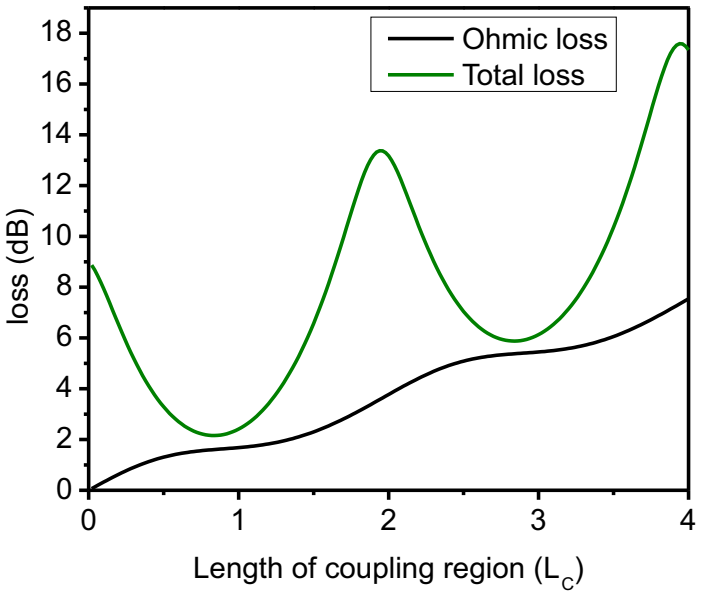

Figure 8.9: Ohmic and total coupling losses as a function of length of the coupling region. Length in this case has units of L_c.

of coupling from silver nanowire to the coupled modes [100].

We have calculated coupling parameters for coupling from the plasmonic mode of silver nanowires to the TM modes of silicon nitride waveguides. The procedure followed here is general and can be used for calculating coupling between different kinds of waveguides, including two plasmonic waveguides and two dielectric waveguides.

8.2 Coupling between Two Silver Nanowires

The schematics for coupling two silver nanowires evanescently is shown in figure 8.10. We have simulated the coupling between two silver nanowires of same diameter, 110 nm, placed on fused silica substrate following the procedure described in previous section. Figure 8.11 shows coupling lengths and coupling losses over a length L_c as a function of the 'Gap' between silver nanowires.

We have experimentally assembled an evanescently coupled silver nanowire system. In this system, a single NV-center in a nanodiamond is coupled to a silver nanowire, and the silver nanowire is evanescently coupled to another silver nanowire.

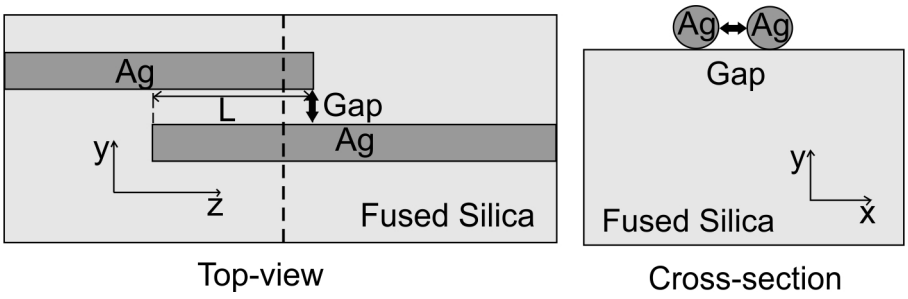

Figure 8.10: **Schmematics of Coupled structure.** Top view schematics of the coupled structure is shown. Cross-section of the coupling region along the dashed line of the coupling structure is also presented. L: Length of coupling region.

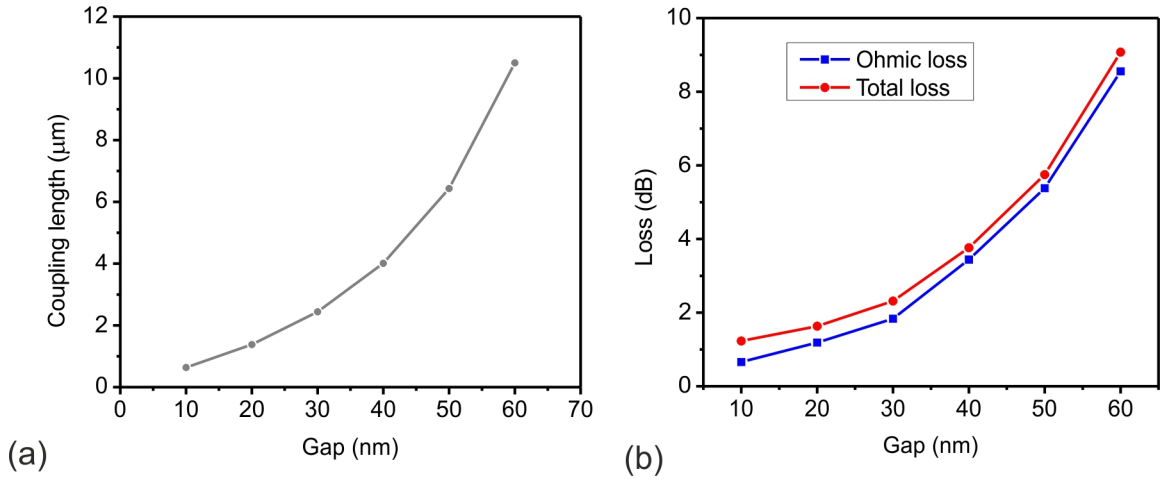

Figure 8.11: **(a)** Coupling length and **(b)** Coupling losses plotted as a function of 'Gap' between the two silver nanowires.

8.2.1 Assembling and Characterization of Evanescently Coupled Silver Nanowires

The sample for this experiment is prepared in a similar way as has been decribed in chapter 4. We then found a system where a nanodiamond containing a single NV-center was lying close to a silver nanowire of a diameter ≈ 110 nm and a length of around 11 μm. Figure 8.12(a) presents an AFM image of the coupled system. The coupling between the NV-center and silver nanowire is confirmed by the galvanometric image taken by exciting the NV-center continuously, which is presented in figure 8.12(b). The image shows the NV-center emission from the spot of the nanodiamond and from the distal ends of the silver nanowire. The single photon characteristics was verified by taking an autocorrelation measurement for the emission from the NV-center. Figure 8.13 presents the autocorrelation measurement data and a fit to a model of three level system as has been described in chapter 2.

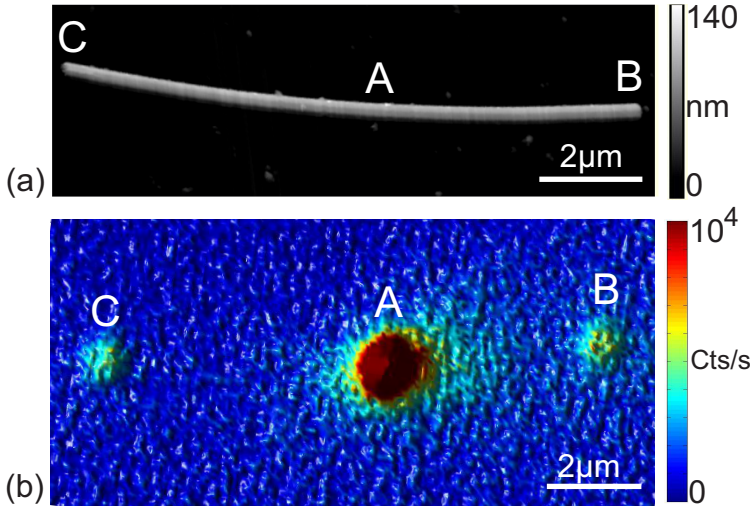

Figure 8.12: **Initial system. (a)** An AFM image of a silver wire of height ≈ 110 nm. 'A' indicates the NV-center position on the silver nanowire. 'B' and 'C' indicates two distal ends of the nanowire. **(b)** A galvanometric image of the coupled system when the NV-center is continuously excited with 532 nm laser light.

After the characterization of the NV-center silver nanowire coupled system, the silver nanowire was cut with the tip of an AFM cantilever. Then, the second nanowire was moved far from the nanowire that was coupled to NV-center. Figure 8.14(a) shows the AFM image of the two nanowires. The galvanometric image was then taken by exciting continuously at spot A. The emission from the distal end 'C" is brighter compared to

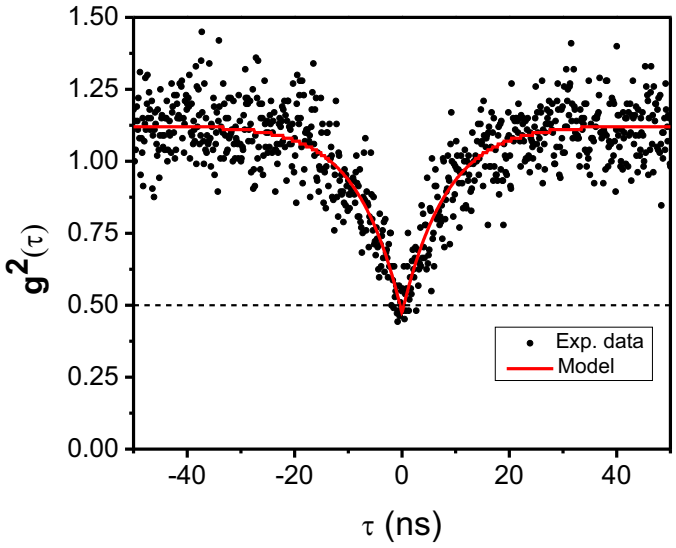

Figure 8.13: **Autocorrelation measurement.** An autocorrelation measurement data and a model fit for point A in figure 8.12(b) showing single photon characteristics of an NV-center coupled to a silver nanowire.

spot 'C' in figure 8.12, which is explained by the high losses in the plasmonic waveguide. The second wire was then slowly moved with the tip of an AFM cantilever in order to make a system where the two nanowires are in the evanescent field of each other. This results in the coupling of the two plasmonic waveguides. Figure 8.15(a) shows an AFM image of the coupled system. 'C"' indicates the region where the coupling between the two silver nanowires takes place. The gap between the two nanowires varies between 20 nm to 40 nm. The length of the coupling region in this case is ≈ 0.9 μm. As can be observed from the fluorescence image shown in figure 8.15(b), some fluorescence gets coupled to the second silver nanowire and re-emits from a distant point which is indicated as spot 'D' in figure 8.15(b).

8.3 Conclusion and Outlook

In this chapter, we have calculated the parameters for coupling between the plasmonic mode of a silver nanowire and a mode in a silicon nitride waveguide. We have also worked on fabrication of silicon nitride waveguides, which is presented in Appendix C. The losses we have obtained for the silicon nitride waveguides are high and the process needs to be optimized. Once we obtain low loss waveguides, we can evanescently couple

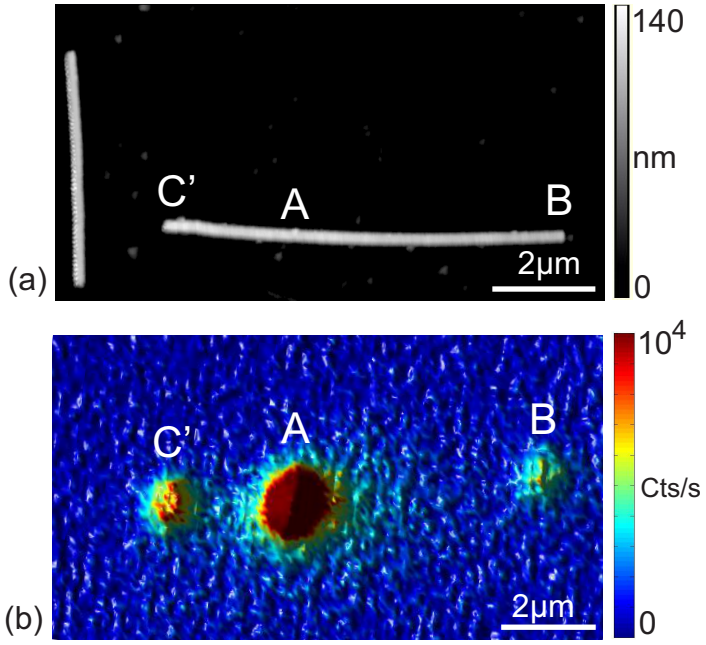

Figure 8.14: **Two Silver nanowires. (a)** An AFM image of the two silver nanowires obtained from the same single wire by cutting. **(b)** A galvanometric image showing the emission from two distal ends of the wire after a part of the silver wire has been cut and moved away.

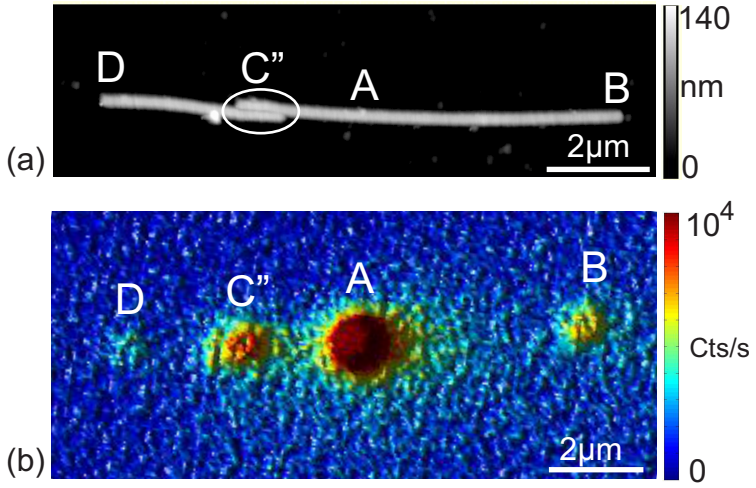

Figure 8.15: **Evanescently coupled silver nanowire system. (a)** An AFM image of two silver nanowires placed close to each other. **(b)** A galvanometric image of the coupled system when the NV-center spot is continuously excited with 532nm laser light.

the plasmonic and dielectric waveguides.

We have also obtained some preliminary results for coupling single photons from one silver nanowire to another. With better control over coupling lengths and gaps, one can obtain efficient coupling between two silver nanowires. The scattering from the coupling region can be avioded by adiabatically changing the gap between two silver nanowires. An example of such a system is shown in figure 8.16. However, these nanowires were not coupled to any NV-center or a fluorescent source. Therefore, coupling could not be observed in this case. With this method, it should also be possible to control the coupling and hence different splitting ratio between the two plasmonic waveguides can be obtained.

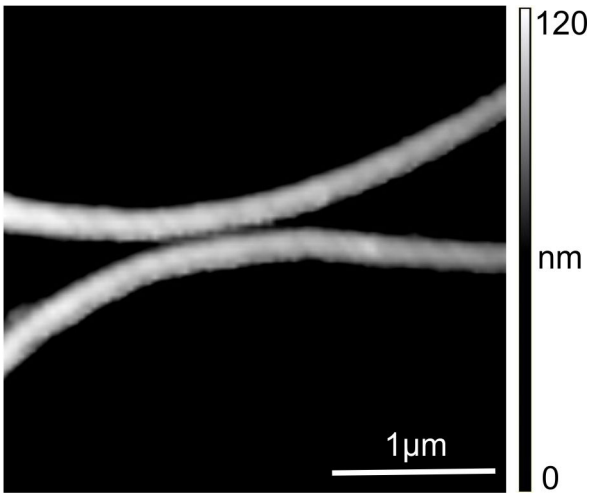

Figure 8.16: **Adiabatic coupling.** AFM image of two silver nanowires where the gap size is gradually changed. Such a system has the potential for adiabatic coupling between two silver nanowires.

Chapter 9

Summary and Outlook

In this thesis, we have described our work towards efficient channeling of emission from an NV-center in a nanodiamond to propagating plasmonic modes, and subsequently to a dielectric waveguide mode. We have used NV-centers in nanodiamonds to study coupling between a quantum emitter and plasmonic modes, because NV-center emits single photons at room temperature, and nanodiamonds can be manipulated with the tip of an AFM cantilever. The plasmonic strutures we have studied, are also useful for coupling to other quantum emitters such as atoms, molecules, and quantum dots.

We coupled single NV-centers contained in a nanodiamond controllably to the propagating plasmonic mode in silver nanowires, by manipulating nanodiamonds with the tip of an AFM cantilever. We then were able to increase the efficiency of coupling by using the gap modes of two silver nanowires placed in parallel. This was also shown with simulations. But the enhancements obtained for the decay rates in case of parallel nanowire obtained experimentally is still much lower (around 8.3) than what is predicted by simulations (of the order of 100). To reach very high efficiency of the coupling, one needs to assemble two parallel nanowires with the gap sizes in the range 10-30 nm with the emitter placed in the gap. These structures can be assembled, for example, by fabrication of parallel grooves in the substrate using e-beam lithography and subsequent placement of silver nanowires in those grooves by manipulation with an AFM.

The NV-centers were also coupled to the propagating mode of a silver nanowire by placing the nanodiamond containing the emitter near to one end of the nanowire. This approach has the advantage that the emission is channeled in one direction. End-to-end aligned silver nanowires with a nanodiamond containing single NV-center was

also investigated for coupling. This system can also provide high enhancement as well as channeling of photons from a dipole emitter into propagating modes of plasmonic waveguides. This can also be used as a controllable splitter of spontaneous emission into the modes of the two silver nanowires, propagating in opposite direction. By appropriate shaping of the ends of the silver nanowires, one can obtain efficient channeling in one direction with a single silver nanowire which can be used for single photon generation on demand, if efficiently coupled to a dielectric waveguide. Coupling of the emitter to the end-to-end aligned nanowires can also be improved by appropriate shaping of the ends.

The coupled systems mentioned above were all assembled using the AFM, and it does not allow for very precise control over the fabrication of structures. To obtain better control over the dimensions, single crystalline silver structures were also fabricated using focussed ion beam (FIB) lithography on single crystalline chemically grown silver nanoplates. Fluorescence from the structures made with this method limits its use for coupling to single NV-centers in room temperature experiments. In addition to that, the conducting substrate, required for FIB milling, decreases the propagation lengths of plasmonic modes in these structures. We then used tip of an AFM cantilever to carve out silver nanowires from silver nanoplates. We have also observed coupling of an NV-center to an AFM fabricated nanowire. Futher refinement of this method can produce thin wires and other desirable silver structures for coupling to single emitters.

Evanescent coupling between a plasmonic waveguide and a dielectric waveguide was studied theoretically. Efficiency of channeling of photons from the plasmonic mode of a silver nanowire to a dielectric mode of silicon nitride waveguide was calculated. It was found that the two waveguides can be coupled with a coupling loss of around 2 dB. Losses in the silicon nitride waveguides, we have fabricated and is presented in Appendix C, has stalled us from coupling it to a plasmonic waveguide.

Coupling by end-to-end alignment of the two kind of waveguides, plasmonic and dielectric, should also be investigated [69]. The coupling efficiency of plasmonic gap modes to the modes in dielectric waveguides should be simulated and optimized. It is important that the coupling length between a plasmonic and dielectric waveguide is minimized, because of the high propagation losses in the plasmonic materials currently available.

We have also worked towards evanescent coupling between two silver nanowires, which can lead to all integrated plasmonic devices. Some preliminary experimental results are presented for these coupled structures.

Appendix A

Silver Nanowire Fabrication

For preparation of silver nanowires, we used polyol reduction of silver nitrate [104]. We purchased all the chemicals required for the preparation of silver nanowires from Sigma Aldrich. Below we give a brief description of the procedure followed for synthesis of silver nanowires, and then some scanning electron microscope (SEM) images of silver nanowires are presented.

A.1 Chemical Synthesization Process

5ml of Ethylene Glycol (EG) was taken in 25 ml Erlenmeyer flask with stopper. It was heated to 151.5 °C with constant stirring at 260 rotations per minute (RPM). The magnetic stirrer combined with hot plate was used for stirring and heating. A thermometer was attached to monitor the temperature during the reaction time. It is very important to keep the temperature as close to 151.5 °C as possible, because the reaction is temperature sensitive and a difference in temperature of 10 °C can create a lot of difference in the aspect ratio of the wires. So, the temperature was controlled, and was kept close to 151.5 °C throughout the process. For this purpose an oil bath was used to place the flask.
While the EG was heated, solutions of Cu (II) chloride di hydrate, silver nitrate and polyvinyl pyrrolidone (PVP) was prepared with following concentrations.

- 2mg of Cu(II) chloride dihydrate in 3ml of EG
- 49mg of PVP in 3ml of EG
- 47.9 mg of silver nitrate in 3ml of EG

After 1 hr, 40 μL of copper chloride solution was added in the heated EG with the help of an electronic pipette. After waiting for 15 minutes, 1.5 ml of PVP solution was added. Immediately after that 1.5 ml of silver nitrate solution was also added. The reaction was then allowed to run for 1.5 hours.
During the reaction, following color changes were observed:

- Within 1min yellow
- Within 3 min red orange
- Within 5 min dirty greenish
- Gradual shift from dirty green to brownish red.
- The end product after 1.5 hours was opaque grey.

Washing Process
Washing of the product obtained, was done by centrifuge process. The product and equal amount of acetone was added to the centrifuge tube and the tube was shaked. The Centrifuge process was run at 3900 RPM for 30 min. It was observed after the process that silver particles were settled down. The liquid from the top was removed by pipette and same process was repeated once more with acetone and then with distilled water. At the end, the product which was settled down in the centrifuge tube (silver nanowires) was dispensed in the distilled water for storage.

A.2 SEM Images of Silver Nanowires

SEM images of some silver nanowires are shown in figure A.1. It can be observed that silver nanowires obtained with the chemical synthesization process has a distribution over lengths and diameter. By changing the parameters of the chemical process, this distribution can be changed. We have made silver nanowires, where the diameter of the nanowires lied between 50 nm to 70 nm, and for another solution between 70 nm and 130 nm. We have mentioned this distribution in the sample preparation part in different chapters.

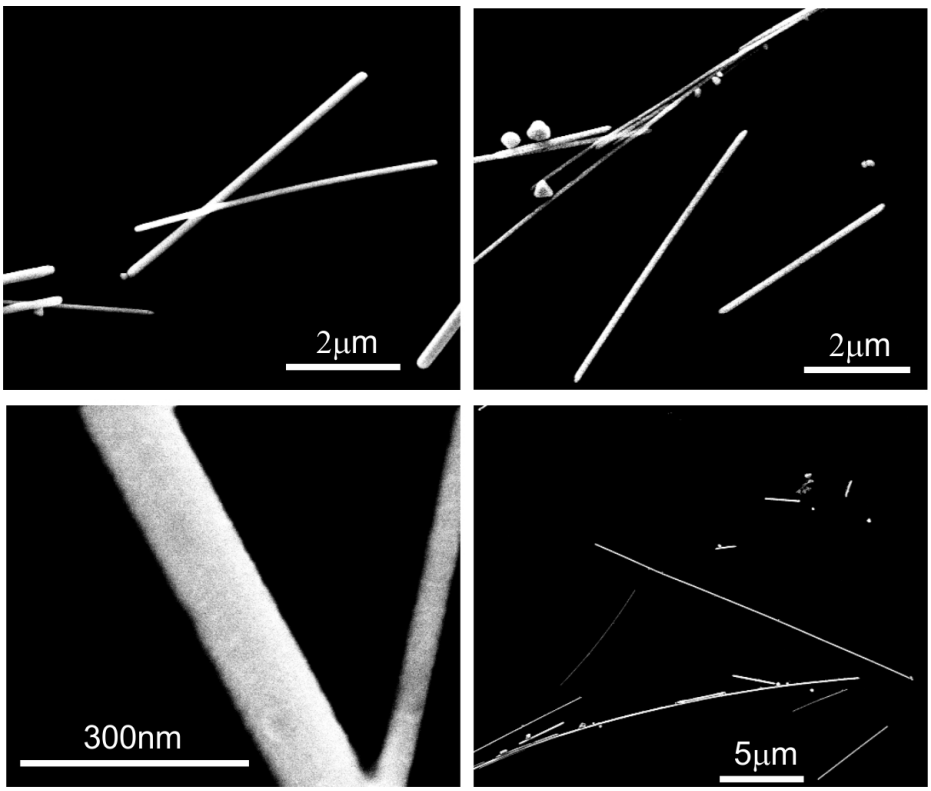

Figure A.1: SEM images of silver nanowires at different scales, for different nanowires.

Appendix B

Fabrication and Characterization of Lithographic Silver Nanostructures

We made silver nanowires and tip structures of silver using e-beam lithography and e-beam assisted deposition of silver layer. The process of fabrication and the results of optical characterization of these structures is presented in this appendix.

B.1 Fabrication of Silver Nanostructures Using E-beam Lithography

We use fused silica substrate of size 2.5×2.5 cm for making silver nanostructures on them. The substrate is plasma cleaned for 5 minutes before starting the process of making the nanostructures. Following steps were taken to fabricate the silver nanostructures:

1. Coating of resist on substrate: Positive e-beam resist ZEP 520A was spin coated. ZEP 520A is diluted in Anisole to obtain different concentrations of ZEP 520A. The thickness of the resist layer depends on the dilution of the resist, and spin speed for the spin coating of resist. Following are some thickness results of the resist. In all cases the acceleration used was 1500 RPM/s and spin time was 30 seconds.

For making the silver nanostructures of thickness 40 nm, resist thinckness > 120 nm was preferred. So, we spin coated ZEP 520A of concentration 5.5% at a spin speed of 1500 RPM. The sample was baked at 180 °C for 2 minutes on a hotplate to cure the resist.

2. Deposition of Al layer: A 20 nm layer of Aluminum was deposited on top of the

Table B.1: Summary of different parametrs used for spin coating the ZEP 520A resist.

ZEP 520A concentration %	spin speed (RPM)	Thickness of resist (nm)
3.6	2000	90
5.5	1500	180
5.5	1000	233
11	3000	450

resist. For fused silica substrate, it is necessary to deposit a charge dissipation layer of Al before E-beam writing to circumvent the charging effects during e-beam writing. Usually, an Al layer of 20 nm is enough for this purpose. The deposition should be thermal, and not e-beam assisted, because the x-ray produced by the 8 keV or 10 keV electron beam will expose the e-beam resist.

3. E-beam writing: Parameters used for E-beam writing for metallic structures were as follows. Current 2nA, 4nm spot, and doses between $220 - 250\mu C/cm^2$ are used.

4. Removal of Al Layer: After E-beam writing, we first remove the Al layer deposited for charge dissipation. This was done by placing the sample for around 70 seconds in MF-322 with manual stirring. The sample was then rinsed in IPA and dried with N_2 gun.

5. Development: The sample was dipped in N-50 for 2 minutes with manual stirring. It was then rinsed in IPA and dried with nitrogen gun. After this process, the e-beam exposed parts of the resist were dissolved and the patterns could be seen under optical microscope.

6. Silver layer deposition: The layer of silver was deposited according to the thickness of the final structures required. This was done using e-beam assisted evaporation of silver.

7. Lift-off: In this step the sample was dipped in the resist remover, called microposit remover 1165. The resist was dissolved, which removed the extra silver, leaving behind the required silver structures on the wafer.

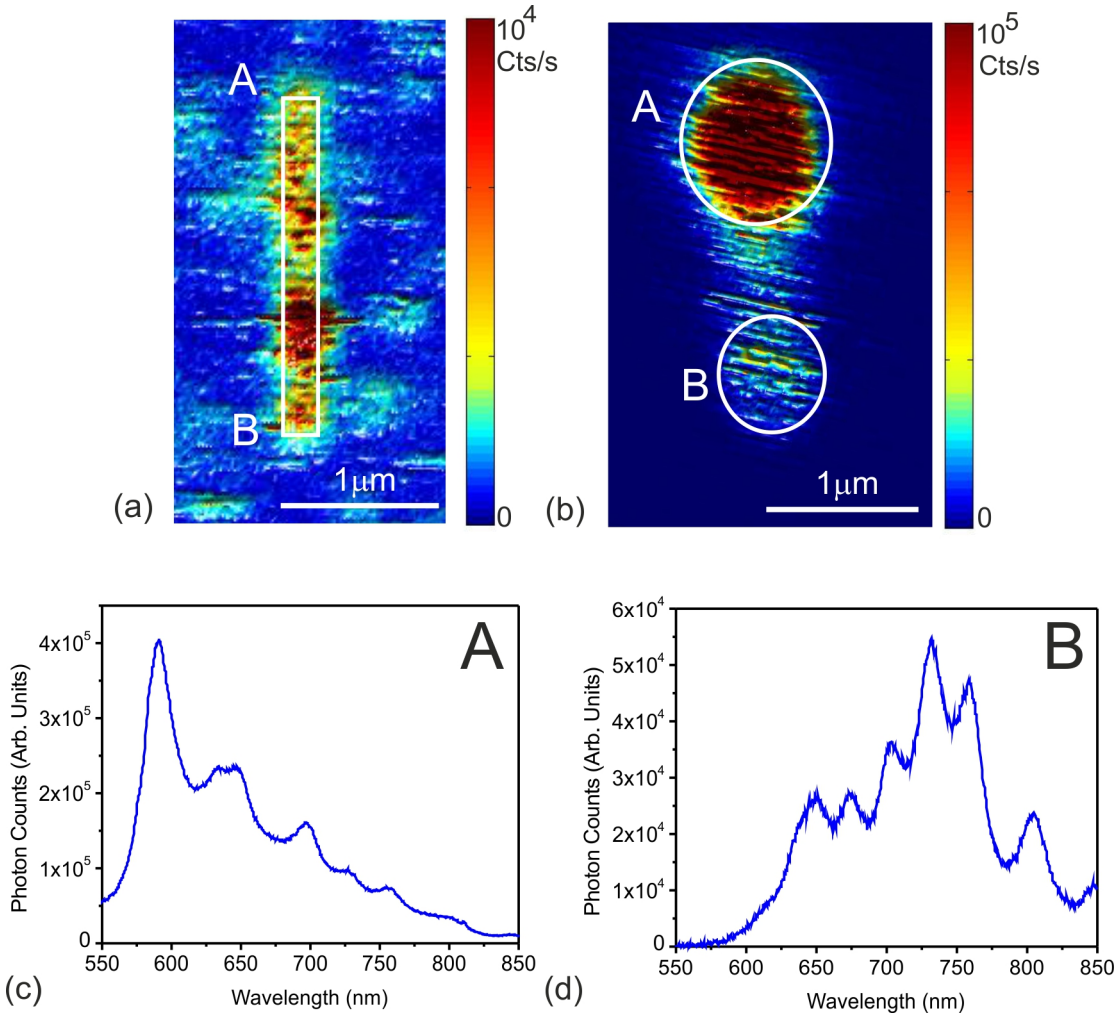

Figure B.1: **(a)** Fluorescence image of a lithographically made silver nanowire. The wire is drawn for the guidance of eye, and is not to scale. **(b)** Galvanometric image when the excitation laser light is signed on end A. **(c)** and **(d)** Spectra of spots A and B shown in (b), respectively.

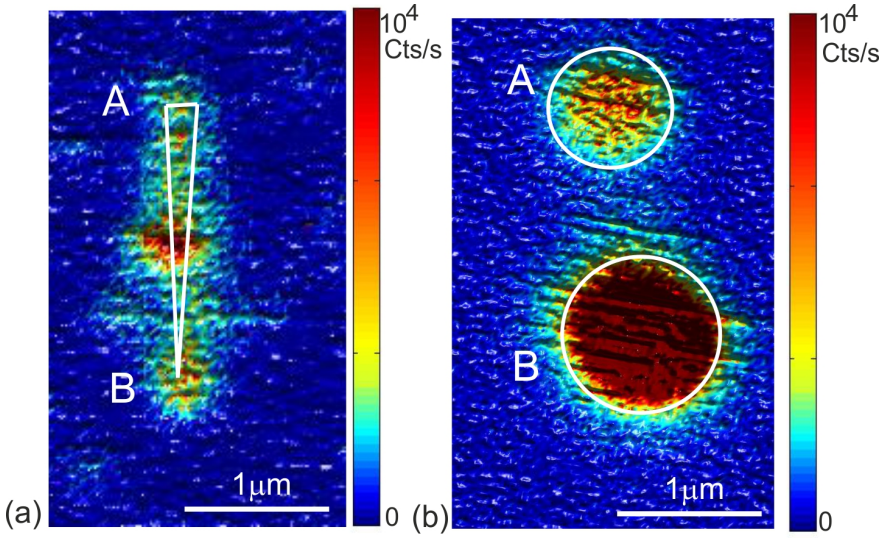

Figure B.2: **(a)** Fluorescence scan image of a tip made using e-beam lithography. The tip is drawn for the guidance of eye, and is not to scale. **(b)** Galvanometric image when end B shown in figure (a) is excited with 532nm laser.

B.2 Optical Characterization of Silver Structures

Silver nanowires and tip structures were tested for fluorescence and propagation of plasmons into them using the confocal set-up described in Chapter 2.

Figure B.1(a) shows the fluorescence image of a silver nanowire of width 90 nm and length 2.5 μm. The height for the strucutures made was 40 nm. The excitation power (532 nm laser CW) in this case was 10 μW. One can observe from figure B.1(a) that the fluorescence from the nanowire is quite high. This results from the polycrystallinity of silver structures obtained with this process [87, 105]. We then took a galvanometric image by continuously shining 100 μW of 532 nm CW laser light at spot A in figure B.1(a). Some of the fluorescence gets coupled to the propagation mode of the silver nanowire and gets scattered from the discontinuities in the silver nanowire. The galvanometric image is shown in figure B.1(b), where it can be observed that the middle part of the nanowire also scatters light. However, the fluorescence from the distal end is scattered more than that from the middle region. This is unlike what we observe in case of chemically grown silver nanowires, or nanowires made using focussed ion beam milling of single crystalline silver nanoplates where coupled fluorescence is scattered only from the ends.

In figure B.1(c) and B.1(d), the spectrum taken at spots 'A' and 'B' in figure B.1(b),

respectively, is presented. The fluorescence at spot 'A' in figure B.1(b) originates from direct scattering of the fluorescence from the silver particles of the nanowires as well as the superposition of it with the light that is reflected from the distal end 'B'. Whereas, the fluorescence from spot 'B' in figure B.1(b) appears due to the fluorescence that propagates to the distal end and its superposition with the multiply reflected fluorescence from two ends of the nanowire. This results in the modulation of the observed spectrum for both spots 'A' and 'B', in figures B.1(c) and B.1(d), respectively. We also fabricated some tip structures. The fluorescence scan image of one of the tip structures is shown in figure B.2(a). One end of the tip, in this case, has a width of 200 nm and the width of the other end is limited by the resolution of the lithographic process ($\approx$ 10 nm). Figure B.2(b) shows the galvanometric image of wire when end B of the tip structure was continuously excited with 35 μW of 532 nm laser light. In this case, the coupling to the propagating mode as well as emission from the distal end is apparently high and two spots can be clearly observed in the galvanometric image.

B.3 Conclusion

We conclude from the optical characterization of silver wires and tips that they support propagating plasmons in the visible spectral region. However, the fluorescence from these structures under 532 nm excitation is very high, which overlaps with the fluorescence from an NV-center in spectrum. So, these structures are not suitable for coupling to NV-centers in room temperature experiments.

Appendix C

Fabrication and Characterization of Silicon Nitride Waveguides

C.1 Fabrication of Silicon Nitride Waveguides

For fabrication of silicon nitride waveguides, we used fused silica substrate in order to have it transparent in the visible region of spectrum. Following steps were followed for the fabrication of silicon nitride waveguides:

1. Deposition of silicon nitride: Stoichiometric silicon nitride layer was deposited using low pressure chemical vapour deposition (LPCVD) technique. This technique is known for producing high quality silicon nitride layers [97]. Before depositing the nitride layer, the substrate was cleaned using a chemical process, in order to get rid of any impurities or small particles from the fused silica substrate.

2. Spin coating of e-beam resist: After deposition of silicon nitride layer, the next step was to spin coat a negative resist ma-N 2403. To increase the adhesion between silicon nitride layer and the resist, we plasma clean our sample followed by a dehydration bake for surface treatment in an oven at 250 °C for 5 days. Then, the resist is spin coated at 3000 RPM for 30 seconds. The acceleration used for the spinner was 500 RPM/s. Expected thickness for the resist was 300 nm. The wafer is then prebaked at 90 °C for 30 minutes.

3. Deposition of aluminium layer: Aluminium layer of thickness 20 nm is deposited thermally to avaoid the charging effects during e-beam writing.

4. E-beam writing: E-beam writing is done to get the desired structures according to the mask. The doses required for this resist is between 340 μC/cm^2 and 370 μC/cm^2.

The current used for the e-beam writing was 6 nA.
5. Development: First, the Al layer is removed by dipping the wafer in MF-322 for around 70 seconds. Then, development is done by ma-D 525 for 40 seconds.
6. Hard-bake of the wafer is done at 165 °C for 5 minutes on a Hot-plate. This is done for the so called 'resist reflow' process, which helps in smoothening of the edges of the resisit structures obtained after development.
7. The silicon nitride etching is done using reactive ion etching (RIE) process and the resist is used as a mask.
8. The resist mask is then removed by dissolving it in acetone, which is followed by plasma cleaning of the wafer.
9. Boro-Phospho-Silica-Glass (BPSG) layer is then deposited using plasma enhanced chemical vapour deposition(PECVD).
10. The wafer is then diced to obtain the waveguides on a desired size substrate.

C.2 Characterization of Silicon Nitride Waveguides.

In figures C.1(a) and C.1(b) SEM images of silicon nitride structures are shown. For taking the SEM images, silicon nitride structures were made on silicon wafers without the BPSG layer on top. From figure C.1(b), it can be seen that some particles are lying on the silicon nitride waveguides. This results from dicing of the wafers.
In figure C.1(c), an optical microscope image is shown, where $532nm$ cw laser light is coupled by focussing with a high NA (0.95) objective on one end of the silicon nitride waveguide. This waveguide was made on fused silica substrate and does not have any BPSG layer on top. The silicon nitride cross-section in this case was 230×400 nm^2. We chose this cross-section in order to match the effective index of plasmonic mode of a silver nanowire to the silicon nitride waveguide, as has been described in chapter 8. From the image taken with the optical microscope, we estimate the propagation losses of the silicon nitride waveguides. Assuming the intensity of scattered light from the waveguide is proportional to the intensity guided by the waveguide, we fit an exponential to the decay of intensity of the scattered light from the silicon nitride waveguides to estimate the propagation losses. For the silicon nitride shown in figure C.1(c), the losses were estimated to be around 8 dB/cm. The propagation losses for the waveguides fabricated so far are high, and optimization of the fabrication process is needed.

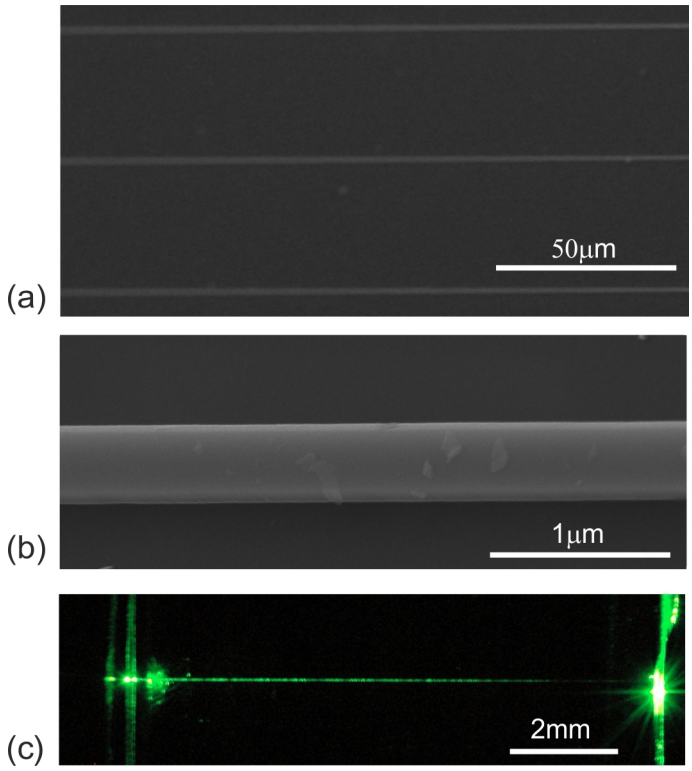

Figure C.1: **(a)** and **(b)** Scanning electron microscope (SEM) images of silicon nitride waveguides. **(c)** An optical microscope image of waveguide when green laser light is coupled into it.

Bibliography

[1] Dmitri K. Gramotnev and Sergey I. Bozhevolnyi. Plasmonics beyond the diffraction limit. *Nature Photonics*, 4:83–91, 2010.

[2] Jon A. Schuller, Edward S. Barnard, Wenshan Cai, Young Chul Jun, Justin S. White, and Mark L. Brongersma. Plasmonics for extreme light concentration and manipulation. *Nature Materials*, 9:193–204, 2010.

[3] E. Ozbay. Plasmonics: Merging photonics and electronics at nanoscale dimensions. *Science*, 311(5758):189–193, 2006.

[4] Evelyn L. Hu, Mark Brongersma, and Adra Baca. *Applications: Nanophotonics and Plasmonics*, volume 1 of *Science Policy Reports*. Springer Netherlands, 2011.

[5] P.R. West, S. Ishii, G.V. Naik, N.K. Emani, V.M. Shalaev, and A. Boltasseva. Searching for better plasmonic materials. *Laser and Photonics Reviews*, 4(6):795–808, 2010.

[6] Harald Ditlbacher, Andreas Hohenau, Dieter Wagner, Uwe Kreibig, Michael Rogers, Ferdinand Hofer, Franz R. Aussenegg, and Joachim R. Krenn. Silver nanowires as surface plasmon resonators. *Physical Review Letters*, 95:257403, Dec 2005.

[7] Sergey I. Bozhevolnyi, Valentyn S. Volkov, E. Devaux, and Thomas W. Ebbesen. Channel plasmon-polariton guiding by subwavelength metal grooves. *Physical Review Letters*, 95:046802, Jul 2005.

[8] Valentyn S. Volkov, Sergey I. Bozhevolnyi, Sergio G. Rodrigo, Luis Martin-Moreno, Francisco J. Garcia-Vidal, E. Devaux, and Thomas W. Ebbesen. Nanofocusing with channel plasmon polaritons. *Nano Letters*, 9(3):1278–1282, 2009.

[9] Junichi Takahara, Suguru Yamagishi, Hiroaki Taki, Akihiro Morimoto, and Tetsuro Kobayashi. Guiding of a one-dimensional optical beam with nanometer diameter. *Optics Letters*, 22(7):475–477, 1997.

[10] R.F. Oulton, V.J. Sorger, D.A. Genov, D.F.P. Pile, and X. Zhang. A hybrid plasmonic waveguide for subwavelength confinement and long-range propagation. *Nature Photonics*, 2(8):496–500, 2008.

[11] S.I. Bozhevolnyi, V.S. Volkov, E. Devaux, J.-Y. Laluet, and T.W. Ebbesen. Channel plasmon subwavelength waveguide components including interferometers and ring resonators. *Nature*, 440(7083):508–511, 2006.

[12] M.A. Noginov, G. Zhu, A.M. Belgrave, R. Bakker, V.M. Shalaev, E.E. Narimanov, S. Stout, E. Herz, T. Suteewong, and U. Wiesner. Demonstration of a spaser-based nanolaser. *Nature*, 460(7259):1110–1112, 2009.

[13] R.F. Oulton, V.J. Sorger, T. Zentgraf, R.-M. Ma, C. Gladden, L. Dai, G. Bartal, and X. Zhang. Plasmon lasers at deep subwavelength scale. *Nature*, 461(7264):629–632, 2009.

[14] A. L. Falk, F. H. L. Koppens, C. L. Yu, K. Kang, N. D. L. Snapp, A. V. Akimov, M. H. Jo, M. D. Lukin, and Hongkun Park. Near-field electrical detection of optical plasmons and single-plasmon sources. *Nature Physics*, 5(5):475–479, 2009.

[15] Reinier W. Heeres, Sander N. Dorenbos, Benny Koene, Glenn S. Solomon, Leo P. Kouwenhoven, and Valery Zwiller. On-chip single plasmon detection. *Nano Letters*, 10(2):661–664, 2010.

[16] Katrin Kneipp, Yang Wang, Harald Kneipp, Lev T. Perelman, Irving Itzkan, Ramachandra R. Dasari, and Michael S. Feld. Single molecule detection using surface-enhanced raman scattering (sers). *Physical Review Letters*, 78:1667–1670, Mar 1997.

[17] Seungchul Kim, Jonghan Jin, Young-Jin Kim, In-Yong Park, Yunseok Kim, and Seung-Woo Kim. High-harmonic generation by resonant plasmon field enhancement. *Nature*, 453:757–760, 2008.

[18] Alpan Bek, Reiner Jansen, Moritz Ringler, Sergiy Mayilo, Thomas A. Klar, and Jochen Feldmann. Fluorescence enhancement in hot spots of afm-designed gold nanoparticle sandwiches. *Nano Letters*, 8(2):485–490, 2008.

[19] Mads L. Andersen, Soren Stobbe, Anders S. Sorensen, and Peter Lodahl. *Nature Physics*, (3):215–218, March.

[20] Pascal Anger, Palash Bharadwaj, and Lukas Novotny. Enhancement and quenching of single-molecule fluorescence. *Physical Review Letters*, 96(11):113002, 2006.

[21] A. Kinkhabwala, Z. Yu, S. Fan, Y. Avlasevich, K. Mllen, and W.E. Moerner. Large single-molecule fluorescence enhancements produced by a bowtie nanoantenna. *Nature Photonics*, 3(11):654–657, 2009.

[22] Alberto G. Curto, Giorgio Volpe, Tim H. Taminiau, Mark P. Kreuzer, Romain Quidant, and Niek F. van Hulst. Unidirectional emission of a quantum dot coupled to a nanoantenna. *Science*, 329(5994):930–933, 2010.

[23] Stefan Schietinger, Michael Barth, Thomas Aichele, and Oliver Benson. Plasmon-enhanced single photon emission from a nanoassembled metal-diamond hybrid structure at room temperature. *Nano Letters*, 9(4):1694–1698, 2009.

[24] Jennifer T. Choy, Birgit J. M. Hausmann, Thomas M. Babinec, Irfan Bulu, Mughees Khan, Patrick Maletinsky, Amir Yacoby, and Marko Loncar. Assembly of hybrid photonic architectures from nanophotonic constituents. *Nature Photonics*, 5:738–743, 2011.

[25] Darrick E. Chang, Anders S. Sørensen, Eugene A. Demler, and Mikhail D. Lukin. A single-photon transistor using nanoscale surface plasmons. *Nature Physics*, 3:807–812, 2007.

[26] A. Gonzalez-Tudela, D. Martin-Cano, E. Moreno, L. Martin-Moreno, C. Tejedor, and F. J. Garcia-Vidal. Entanglement of two qubits mediated by one-dimensional plasmonic waveguides. *Physical Review Letters*, 106, Jan 2011.

[27] D. E. Chang, A. S. Sørensen, P. R. Hemmer, and M. D. Lukin. Quantum optics with surface plasmons. *Physical Review Letters*, 97(5):053002, 2006.

[28] D. E. Chang, A. S. Sørensen, P. R. Hemmer, and M. D. Lukin. Strong coupling of single emitters to surface plasmons. *Physical Review B*, 76:035420, Jul 2007.

[29] T.M. Babinec, B.J.M. Hausmann, M. Khan, Y. Zhang, J.R. Maze, P.R. Hemmer, and M. Lonar. A diamond nanowire single-photon source. *Nature Nanotechnology*, 5(3):195–199, 2010.

[30] K.-M.C. Fu, C. Santori, P.E. Barclay, I. Aharonovich, S. Prawer, N. Meyer, A.M. Holm, and R.G. Beausoleil. Coupling of nitrogen-vacancy centers in diamond to a gap waveguide. *Applied Physics Letters*, 93(23), 2008.

[31] J. Wolters, A. W. Schell, G. Kewes, N. Nsse, M. Schoengen, H. Dscher, T. Hannappel, B. Lchel, M. Barth, and O. Benson. Enhancement of the zero phonon line emission from a single nitrogen vacancy center in a nanodiamond via coupling to a photonic crystal cavity. *Applied Physics Letters*, 97(14), 2010.

[32] P.E. Barclay, K.-M.C. Fu, C. Santori, and R.G. Beausoleil. Chip-based microcavities coupled to nitrogen-vacancy centers in single crystal diamond. *Applied Physics Letters*, 95(19), 2009.

[33] A. V. Akimov, A. Mukherjee, C. L. Yu, D. E. Chang, A. S. Zibrov, P. R. Hemmer, H. Park, and M. D. Lukin. Generation of single optical plasmons in metallic nanowires coupled to quantum dots. *Nature*, 450(06230):402–406, 2007.

[34] Xin Guo, Min Qiu, Jiming Bao, Benjamin J. Wiley, Qing Yang, Xining Zhang, Yaoguang Ma, Huakang Yu, and Limin Tong. Direct coupling of plasmonic and photonic nanowires for hybrid nanophotonic components and circuits. *Nano Letters*, 9(12):4515–4519, 2009.

[35] G. Balasubramanian, P. Neumann, D. Twitchen, M. Markham, R. Kolesov, N. Mizuochi, J. Isoya, J. Achard, J. Beck, J. Tissler, V. Jacques, P. R. Hemmer, F. Jelezko, and J. Wrachtrup. Ultralong spin coherence time in isotopically engineered diamond. *Nature Materials*, 8(5):383–387, 2009.

[36] A. Gruber, A. Dräbenstedt, C. Tietz, L. Fleury, J. Wrachtrup, and C. von Borczyskowski. Scanning confocal optical microscopy and magnetic resonance on single defect centers. *Science*, 276(5321):2012–2014, 1997.

[37] G. Balasubramanian, I.Y. Chan, R. Kolesov, M. Al-Hmoud, J. Tisler, C. Shin, C. Kim, A. Wojcik, P.R. Hemmer, A. Krueger, T. Hanke, A. Leitenstorfer, R. Bratschitsch, F. Jelezko, and J. Wrachtrup. Nanoscale imaging magnetometry with diamond spins under ambient conditions. *Nature*, 455(7213):648–651, 2008.

[38] Jörg Wrachtrup and Fedor Jelezko. Processing quantum information in diamond. *Journal of Physics: Condensed Matter*, 18(21):S807, 2006.

[39] I Aharonovich, S Castelletto, D A Simpson, C-H Su, A D Greentree, and S Prawer. Diamond-based single-photon emitters. *Reports on Progress in Physics*, 74(7):076501, 2011.

[40] F. Jelezko, T. Gaebel, I. Popa, A. Gruber, and J. Wrachtrup. Observation of coherent oscillations in a single electron spin. *Physical Review Letters*, 92(7):076401, Feb 2004.

[41] Liang Jiang, Jacob M. Taylor, Anders S. Sørensen, and Mikhail D. Lukin. Distributed quantum computation based on small quantum registers. *Physical Review A (Atomic, Molecular, and Optical Physics)*, 76(6):062323, 2007.

[42] P. Neumann, N. Mizuochi, F. Rempp, P. Hemmer, H. Watanabe, S. Yamasaki, V. Jacques, T. Gaebel, F. Jelezko, and J. Wrachtrup. Multipartite entanglement among single spins in diamond. *Science*, 320(5881):1326–1329, 2008.

[43] M. V. Gurudev Dutt, L. Childress, L. Jiang, E. Togan, J. Maze, F. Jelezko, A. S. Zibrov, P. R. Hemmer, and M. D. Lukin. Quantum Register Based on Individual Electronic and Nuclear Spin Qubits in Diamond. *Science*, 316(5829):1312–1316, 2007.

[44] E. Togan, Y. Chu, A. S. Trifonov, L. Jiang, J. Maze, L. Childress, M. V. G. Dutt, A. S. Sørensen, P. R. Hemmer, A. S. Zibrov, and M. D. Lukin. Quantum entanglement between an optical photon and a solid-state spin qubit. *Nature*, 466(466):730–734, 2010.

[45] G. Davies and M. F. Hamer. Optical studies of the 1.945 ev vibronic band in diamond. *Proceedings of the Royal Society of London. Series A, Mathematical and Physical Sciences*, 348(1653):285–298, 1976.

[46] A. Batalov, V. Jacques, F. Kaiser, P. Siyushev, P. Neumann, L. J. Rogers, R. L. McMurtrie, N. B. Manson, F. Jelezko, and J. Wrachtrup. Low temperature studies of the excited-state structure of negatively charged nitrogen-vacancy color centers in diamond. *Physical Review Letters*, 102(19):195506, 2009.

[47] N. B. Manson, J. P. Harrison, and M. J. Sellars. Nitrogen-vacancy center in diamond: Model of the electronic structure and associated dynamics. *Physical Review B (Condensed Matter and Materials Physics)*, 74(10):104303, 2006.

[48] Hannes Bernien, Lilian Childress, Lucio Robledo, Matthew Markham, Daniel Twitchen, and Ronald Hanson. Two-photon quantum interference from separate nitrogen vacancy centers in diamond. *Physical Review Letters*, 108:043604, Jan 2012.

[49] A. Sipahigil, M. L. Goldman, E. Togan, Y. Chu, M. Markham, D. J. Twitchen, A. S. Zibrov, A. Kubanek, and M. D. Lukin. Quantum interference of single photons from remote nitrogen-vacancy centers in diamond. *Physical Review Letters*, 108:143601, Apr 2012.

[50] Christian Kurtsiefer, Sonja Mayer, Patrick Zarda, and Harald Weinfurter. Stable solid-state source of single photons. *Physical Review Letters*, 85(2):290–293, Jul 2000.

[51] Jasprit Singh. *Physics of Semiconductors and Their Heterostructures*. Mcgraw-Hill College, 1992.

[52] Rosa Brouri, Alexios Beveratos, Jean-Philippe Poizat, and Philippe Grangier. Photon antibunching in the fluorescence of individual color centers in diamond. *Optics Letters*, 25(17):1294–1296, 2000.

[53] F. Jelezko and J. Wrachtrup. Read-out of single spins by optical spectroscopy. *Journal of Physics: Condensed Matter*, 16(30):R1089–R1104, 2004.

[54] R Alléaume, F Treussart, G Messin, Y Dumeige, J-F Roch, A Beveratos, R Brouri-Tualle, J-P Poizat, and P Grangier. Experimental open-air quantum key distribution with a single-photon source. *New Journal of Physics*, 6(1):92, 2004.

[55] Julia Tisler, Gopalakrishnan Balasubramanian, Boris Naydenov, Roman Kolesov, Bernhard Grotz, Rolf Reuter, Jean-Paul Boudou, Patrick A. Curmi, Mohamed Sennour, Alain Thorel, Michael Borsch, Kurt Aulenbacher, Rainer Erdmann, Philip R. Hemmer, Fedor Jelezko, and Jorg Wrachtrup. Fluorescence and spin properties of defects in single digit nanodiamonds. *ACS Nano*, 3(7):1959–1965, 2009.

[56] C. Bradac, T. Gaebel, N. Naidoo, M.J. Sellars, J. Twamley, L.J. Brown, A.S. Barnard, T. Plakhotnik, A.V. Zvyagin, and J.R. Rabeau. Observation and con-

trol of blinking nitrogen-vacancy centres in discrete nanodiamonds. *Nature Nanotechnology*, 5(5):345–349, 2010.

[57] Alexios Beveratos, Rosa Brouri, Thierry Gacoin, Jean-Philippe Poizat, and Philippe Grangier. Nonclassical radiation from diamond nanocrystals. *Physical Review A*, 64:061802, Nov 2001.

[58] Andreas W. Schell, Günter Kewes, Tim Schröder, Janik Wolters, Thomas Aichele, and Oliver Benson. A scanning probe-based pick-and-place procedure for assembly of integrated quantum optical hybrid devices. *Review of Scientific Instruments*, 82(7):073709, 2011.

[59] Oliver Benson. Assembly of hybrid photonic architectures from nanophotonic constituents. *Nature*, 480:193–199, 2011.

[60] Rodney Loudon. *The Quantum Theory of Light*. 2000.

[61] A T Collins, M F Thomaz, and M I B Jorge. Luminescence decay time of the 1.945 ev centre in type ib diamond. *Journal of Physics C: Solid State Physics*, 16(11):2177, 1983.

[62] A. Batalov, C. Zierl, T. Gaebel, P. Neumann, I.-Y. Chan, G. Balasubramanian, P. R. Hemmer, F. Jelezko, and J. Wrachtrup. Temporal coherence of photons emitted by single nitrogen-vacancy defect centers in diamond using optical rabi-oscillations. *Physical Review Letters*, 100:077401, Feb 2008.

[63] R. Hanbury Brown and R. Q. Twiss. Correlation between photons in two coherent beams of light. *Nature*, 177:27–29.

[64] E.D.Palik. *Handbook of Optical Constants*. Academic Press, 1998.

[65] A. W. Snyder and J. Love. *Optical Waveguide Theory*. 1983.

[66] Yuntian Chen, Torben Roland Nielsen, Niels Gregersen, Peter Lodahl, and Jesper Mørk. Finite-element modeling of spontaneous emission of a quantum emitter at nanoscale proximity to plasmonic waveguides. *Physical Review B*, 81:125431, Mar 2010.

[67] L. Novotny and B. Hecht. *Principles of Nano Optics*. 2006.

[68] Benjamin Xia Younan Chen Antao Pyayt, Anna L. Wiley and Larry Dalton. Integration of photonic and silver nanowire plasmonic waveguides. *Nature Nanotechnology*, 3:660–665, 2008.

[69] Xue-Wen Chen, Vahid Sandoghdar, and Mario Agio. Highly efficient interfacing of guided plasmons and photons in nanowires. *Nano Letters*, 9(11):3756–3761, 2009.

[70] Roman Kolesov, Bernhard Grotz, Gopalakrishnan Balasubramanian, Rainer J. Stöhr, Aurélien A. L. Nicolet, Philip R. Hemmer, Fedor Jelezko, and Jörg Wrachtrup. Waveparticle duality of single surface plasmon polaritons. *Nature Physics*, 5:470–474, 2009.

[71] R. J. Epstein, F. M. Mendoza, Y. K. Kato, and D. D. Awschalom. Anisotropic interactions of a single spin and dark-spin spectroscopy in diamond. *Nature Physics*, 1(2):94–98, October 2005.

[72] A. Huck, S. Kumar, A. Shakoor, and U. L. Andersen. Controlled coupling of a single nitrogen-vacancy center to a silver nanowire. *Physical Review Letters*, 106(8):096801, 2011.

[73] P. B. Johnson and R. W. Christy. Optical constants of the noble metals. *Physical Review B*, 6(12):4370–4379, Dec 1972.

[74] Andreas W. Schell, Günter Kewes, Tobias Hanke, Alfred Leitenstorfer, Rudolf Bratschitsch, Oliver Benson, and Thomas Aichele. Single defect centers in diamond nanocrystals as quantum probes for plasmonic nanostructures. *Optics Express*, 19(8):7914–7920, Apr 2011.

[75] A. Manjavacas and F. J. Garcia de Abajo. Robust plasmon waveguides in strongly interacting nanowire arrays. *Nano Letters*, 9(4):1285–1289, 2009.

[76] Giuseppe Toscano, Søren Raza, Antti-Pekka Jauho, N. Asger Mortensen, and Martijn Wubs. Modified field enhancement and extinction by plasmonic nanowire dimers due to nonlocal response. *Optics Express*, 20(4):4176–4188, Feb 2012.

[77] S.D. Liu, M. T. Cheng, Z. J. Yang, and Q. Q. Wang. Surface plasmon propagation in a pair of metal nanowires coupled to a nanosized optical emitter. *Optics Letters*, 33(8):851–853, 2008.

[78] Ewold Verhagen, Marko Spasenović, Albert Polman, and L. (Kobus) Kuipers. Nanowire plasmon excitation by adiabatic mode transformation. *Physical Review Letters*, 102:203904, May 2009.

[79] J. Greffet, J. Hugonin, M. Besbes, N. D. Lai, F. Treussart, and J. Roch. Diamond particles as nanoantennas for nitrogen-vacancy color centers. *ArXiv e-prints*, July 2011.

[80] Jer-Shing Huang, Victor Callegari, Peter Geisler, Christoph Brning, Johannes Kern, Jord C. Prangsma, Xiaofei Wu, Thorsten Feichtner, Johannes Ziegler, Pia Weinmann, Martin Kamp, Alfred Forchel, Paolo Biagioni, Urs Sennhauser, and Bert Hecht. Atomically flat single-crystalline gold nanostructures for plasmonic nanocircuitry. *Nature communications*, 1:350–357, 2010.

[81] Zhirui Guo, Yu Zhang, Yun DuanMu, Lina Xu, Shengli Xie, and Ning Gu. Facile synthesis of micrometer-sized gold nanoplates through an aniline-assisted route in ethylene glycol solution. *Colloids and Surfaces A: Physicochemical and Engineering Aspects*, 278(13):33 – 38, 2006.

[82] Xionghui Cai and Aixia Zhai. Preparation of microsized silver crystals with different morphologies by a wet-chemical method. *Rare Metals*, 29:407–412, 2010.

[83] Ming-Shang Jin, Qin Kuang, Xi-Guang Han, Shui-Fen Xie, Zhao-Xiong Xie, and Lan-Sun Zheng. Liquidliquid interface assisted synthesis of size- and thickness-controlled ag nanoplates. *Journal of Solid State Chemistry*, 183(6):1354 – 1358, 2010.

[84] Tanja Deckert-Gaudig, Florian Erver, and Volker Deckert. Transparent silver microcrystals: Synthesis and application for nanoscale analysis. *Langmuir*, 25(11):6032–6034, 2009.

[85] Qi Lu, Kun-Jae Lee, Sung-Jei Hong, Nosang V. Myung, Hee-Taik Kim, and Yong-Ho Choa. Growth factors for silver nanoplates formed in a simple solvothermal process. *Journal of Nanoscience and Nanotechnology*, 10(5):3393–3396, 2010.

[86] Lucille A. Giannuzzi and Fred A. Stevie. *Introduction to focussed Ion Beams: Instrumentation, Theory, Techniques and Practice*. Springer, USA, 2005.

[87] Lynn A. Peyser, Amy E. Vinson, Andrew P. Bartko, and Robert M. Dickson. Photoactivated fluorescence from individual silver nanoclusters. *Science*, 291(5501):103–106, 2001.

[88] Hong Wei, Daniel Ratchford, Xiaoqin (Elaine) Li, Hongxing Xu, and Chih-Kang Shih. Propagating surface plasmon induced photon emission from quantum dots. *Nano Letters*, 9(12):4168–4171, 2009.

[89] Marco Allione, Vasily V. Temnov, Yuri Fedutik, Ulrike Woggon, and Mikhail V. Artemyev. Surface plasmon mediated interference phenomena in low-q silver nanowire cavities. *Nano Letters*, 8(1):31–35, 2008.

[90] S. Laux, N. Kaiser, A. Zller, R. Gtzelmann, H. Lauth, and H. Bernitzki. Room-temperature deposition of indium tin oxide thin films with plasma ion-assisted evaporation. *Thin Solid Films*, 335(12):1 – 5, 1998.

[91] Reuven Gordon. Reflection of cylindrical surface waves. *Optics Express*, 17(21):18621–18629, Oct 2009.

[92] A-T. Akono, P. M. Reis, and F-J. Ulm. Scratching as a fracture process: From butter to steel. *Physical Review Letters*, 106:204302, May 2011.

[93] Benjamin J. Wiley, Darren J. Lipomi, Jiming Bao, Federico Capasso, and George M. Whitesides. Fabrication of surface plasmon resonators by nanoskiving single-crystalline gold microplates. *Nano Letters*, 8(9):3023–3028, 2008.

[94] D Tabor. Mohs's hardness scale - a physical interpretation. *Proceedings of the Physical Society. Section B*, 67(3):249, 1954.

[95] R. Wan, F. Liu, Y. Huang, S. Hu, B. Fan, Y. Miura, D. Ohnishi, Y. Li, H. Li, and Y. Xia. Excitation of short range surface plasmon polariton mode based on integrated hybrid coupler. *Applied Physics Letters*, 97(14), 2010.

[96] Boyu Fan, Fang Liu, Yunxiang Li, Yidong Huang, Yoshikatsu Miura, and Dai Ohnishi. Refractive index sensor based on hybrid coupler with short-range surface plasmon polariton and dielectric waveguide. *Applied Physics Letters*, 100(11), 2012.

[97] N. Daldosso, M. Melchiorri, F. Riboli, F. Sbrana, L. Pavesi, G. Pucker, C. Kompocholis, M. Crivellari, P. Bellutti, and A. Lui. Fabrication and optical characterization of thin two-dimensional si3n4 waveguides. *Materials Science in Semiconductor Processing*, 7(46):453 – 458, 2004.

[98] A. Gorin, A. Jaouad, E. Grondin, V. Aimez, and P. Charette. Fabrication of silicon nitride waveguides for visible-light using pecvd: a study of the effect of plasma frequency on optical properties. *Optics Express*, 16(18):13509–13516, Sep 2008.

[99] Qiang Li, Shanshan Wang, Yiting Chen, Min Yan, Limin Tong, and Min Qiu. Experimental demonstration of plasmon propagation, coupling, and splitting in silver nanowire at 1550-nm wavelength. *Selected Topics in Quantum Electronics, IEEE Journal of*, 17(4):1107 –1111, july-aug. 2011.

[100] R. Wan, F. Liu, X. Tang, Y. Huang, and J. Peng. Vertical coupling between short range surface plasmon polariton mode and dielectric waveguide mode. *Applied Physics Letters*, 94(14), 2009.

[101] Wei-Ping Huang. Coupled-mode theory for optical waveguides: an overview. *Journal of Optical Society of America A*, 11(3):963–983, Mar 1994.

[102] Yunchuan Kong, M. Chabalko, E. Black, S. Powell, J.A. Bain, T.E. Schlesinger, and Yi Luo. Evanescent coupling between dielectric and plasmonic waveguides for hamr applications. *Magnetics, IEEE Transactions on*, 47(10):2364 –2367, oct. 2011.

[103] Qiang Li, Yi Song, Gan Zhou, Yikai Su, and Min Qiu. Asymmetric plasmonic-dielectric coupler with short coupling length, high extinction ratio, and low insertion loss. *Optics Letters*, 35(19):3153–3155, Oct 2010.

[104] Kylee E. Korte, Sara E. Skrabalak, and Younan Xia. Rapid synthesis of silver nanowires through a cucl- or cucl2-mediated polyol process. *Journal of Materials Chemistry*, 18(4):437–441, 2008.

[105] Jie Zheng, Yong Ding, Bozhi Tian, Zhong L. Wang, and Xiaowei Zhuang. Luminescent and Raman Active Silver Nanoparticles with Polycrystalline Structure. *Journal of the American Chemical Society*, 130(32):10472–10473, August 2008.